# Synthesis, processing and applications of carbonaceous nanomaterials

By

**Yuqin Yao**

A Dissertation
Submitted to the Faculty
of the

**WORCESTER POLYTECHNIC INSTITUTE**

***In partial fulfillment of the requirements for the***

Degree of Doctor of Philosophy
In
Material Science and Engineering

August 2013

APPROVED:

_____

Jianyu Liang, Ph.D. Advisor
Associate Professor of Mechanical Engineering

_____

Richard D. Sisson, Jr.
George F. Fuller Professor
Director of Manufacturing and Materials Engineering

# ABSTRACT

Carbon is one of the most abundant non-metal elements in the world. The unique arrangement of electrons enables diverse properties and applications of carbon. Long before the discovery of $C_{60}$ in 1985, which is now considered a milestone in the vibrant field of carbon nanotechnology, carbon has been a vital part of human history. It has been a key enabling material in many fields including aerospace, transportation, energy storage, electric devices, infrared sensors, etc. The report of fullerene triggered a feverish surge of interest and effort in the study of nanostructured carbon. Along with the discovery of carbon nanotubes (CNTs) and graphene nanosheets (GNS), the nanocarbon family has been extensively studied. However, controlled production of carbon nanomaterials with low cost and high efficiency and incorporation of nanocarbons to maximize their contribution in advanced applications still faces a lot of technical difficulties.

The objective of this work is to study and optimize processes to synthesize multiwall carbon nanotubes (MWCNTs) and GNS, and to apply GNS in nanocomposite anode materials for Lithium ion batteries (LIBs). Therefore, in this thesis, there are three main parts: (1) development of the post-processing method to obtain free-standing CNT arrays by the template-assisted chemical vapor deposition (CVD) method; (2) development of a synthesis protocol to obtain GNS by oxidation of natural graphite flakes and reduction of the resulted graphene oxides; and (3) fabrication of $TiO_2$/GNS in core-shell structure by a static electric assembling method to improve anode performance for LIB applications.

# ACKNOWLEDGEMENTS

This thesis was completed under Prof. Liang's supervision. During my five years of Ph. D life, she has been always giving me helpful advice, encouraging me to keep moving towards the destination, to complete this thesis. It was her who taught me to write articles in an academic way. Besides, she has also been helping me to deal with many other things in life—my Ph. D work could never have been done without her. I also want to thank Prof. Sisson, Prof. Zhenhai Xia and Prof. Mingjiang Tao for being my committee members.

I would like to thank all of my lab mates I have been working with: Huanan, Qiming, Rose, Sid, Meghan and Yinjie, etc. They helped me a lot in the lab, which made my progress towards my graduation much faster.

I would like to thank my parents, Guangquan Yao and Huimin Gu, they have been supporting me all these years. They always encouraged me when I was upset—no matter in work or in life, I love them both very much.

Finally, I want to dedicate this thesis to my grandparents who both passed away during the very first year I came to U.S. They brought me up, and they supported me both financially and spiritually when they were alive. I Hope they could see this in heaven.

# TABLE OF CONTENTS

# CHAPTER 1: INTRODUCTION

"*There's Plenty of Room at the Bottom, the problems of chemistry and biology can be greatly helped if our ability to see what we are doing, and to do things on an atomic level, is ultimately developed — a development which I think cannot be avoided.*" -- *Richard Feynman*

Feynman envisioned a 'wonderland' of tiny things that could provide many fascinating opportunities. With the persistent pursuit of enthusiastic researchers, scientists and engineers in the past two decades, much of Feynman's prediction has been turned into reality. Nowadays, nanomaterials and nanotechnology are becoming an important part of our world and our daily life. For example, solid state lighting based on thin film semiconductors is widely used and contributes to savings in energy consumption. Nanostructured material-based sensors provide a powerful platform with higher sensitivity, selectivity, accuracy, and faster response benefiting biology, national security, fire protection, drug discovery, disease diagnosis, etc. Nanomaterial-based composite, like novel conducting polymers, conducting metal matrix composites, and high fracture-strength ceramics have shown superior performances. Among all the advancements, the discovery and study of carbonaceous nanomaterials captured much excitement and attention due to their unique structures and properties.

Since the early ages of human history, carbon has been a familiar and useful element to us. Of course, now we know that many organic materials contain carbon and it is considered to be one of the essential elements of all life forms. But in prehistory, relatively pure forms of carbon were discovered and known as soot and charcoal and have been utilized since the earliest human civilizations. Several conventional carbon allotropes with diverse properties are still widely used in modern industries. For example, diamonds are widely used as cutting and grinding tools due to their superior hardness. Graphite is used in refractories, batteries, steelmaking, foundry facings, lubricants, etc.

One of the nanostructured carbon materials, carbon nanotube, was discovered as early as the 1960's[1]. Since then, several nanostructured carbonaceous materials were discovered or studied, including $C_{60}$[2], carbon nanotubes(CNTs)[3] and graphene

nanosheets(GNS)[4]. All of them have demonstrated unique mechanical, thermal, optical, and electrical properties due to their nanosize effect and special dimension feature. Hence, a growing number of scientists are working diligently to either seek for improved synthesis methods, or try to tailor, decorate, and assemble nanostructured carbon materials for various applications.

Among them, fullerene, discovered in 1985, is considered the 0-D carbon material. Carbon nanotube(CNT) is the 1-D material rediscovered in 1991[3].Graphene nano sheet(GNS) is the 2-D nano materials with a tight honeycomb arrangement of carbon atoms obtained by mechanical exfoliation[4] in 2004. GNS had been predicted to be unstable under room temperature due to its 2-D feature[5]. Thus, its discovery not only rejected the old theory, but also filled the gap between 1-D carbon materials (CNTs) and 3-D carbon materials (graphite).

## Research Objective

The goal of this work is to synthesize and process CNT and GNS with controllability for mechanical and energetic applications. For the intended applications, control over the morphology, size, structure and surface properties (chemistry) is of great importance.

## Research Plan

The research plans for this thesis are mainly focused on synthesis and self-assembly of CNTs or GNS. In order to make well-oriented and free standing CNTs, we applied the template-assisted chemical vapor deposition(CVD) method to synthesize well oriented CNTs[6]. To expose the CNTs so as to meet the requirement of the future mechanical test, we devised a two-step post growth process: first, mechanical polishing to remove the amorphous carbon on the sample's surface, followed by an etching step by a NaOH solution at a certain concentration.

Furthermore, we improved the oxidation process to oxidize natural graphite flakes into graphite oxide[7], which can be considered a precursor of graphene. Combined with a fast thermal reduction step, a large quantity of GNS of high quality

was synthesized.

Finally, we introduced GNS into $TiO_2$ nanoparticles to make a $TiO_2$/GNS composite with a novel encapsulation structure and studied its use as an anode for lithium batteries.

**The detailed research plans are listed below:**

***1. Fabrication of highly oriented and free-standing carbon nanotubes:*** A 2-step anodization was conducted in this project to create the template for CNT growth. The CVD method was applied to synthesize multiple walled CNTs within the uniform nano-pores. After the synthesis, a simple but highly efficient mechanical polishing method was used to remove the amorphous carbon that covers the sample. In this step, different sizes of aluminum powder were used and the resulted roughness was investigated. Then the sample was etched by NaOH solution to obtain the free-standing carbon nanotube arrays. The topology was examined by SEM and AFM.

***2. Synthesis of graphene nanosheets by an improved routine:*** A previously reported method was adapted and improved to generate graphite oxide with high yield and high quality. The resulted graphite oxide served as a precursor to synthesize the final product: GNS. Two kinds of widely applied methods (thermal reduction and chemical reduction) were studied and compared. By various characterizations (SEM, AFM, UV-Vis, FTIR and XRD), it was concluded that the improved oxidization of graphite method combined with thermal reduction is a better routine to synthesize GNS with high quality.

***3. Syntheis $TiO_2$/GNS composite for LIB applications:*** In this project, anatase $TiO_2$ nano particles were synthesized by a facile sol-gel method[8]. In order to improve the conductivity and shorten the lithium ion diffusion length, GNS was introduced. $TiO_2$ nano particles were treated with (3-aminopropyl)triethoxysilane (APTES) to make the surface positively charged[9]. Since graphene oxide was negatively charged in nature, an encapsulation structure was obtained by electrostatic mechanism. Followed by a reduction step, $TiO_2$/GNS composite was synthesized. SEM was used to observe the morphology. FTIR and Zeta potential were applied to confirm the functional groups and the surface charging information, XRD was employed to investigate the crystal structure information.

## Thesis organization

This thesis includes 4 parts in total: the introduction part is to provide the readers with the motivation, objectives and research plans of the study. Second chapter is a paper review that summarizes the history of carbon nanotechnology and important advances in synthesis, characterization and applications of CNTs and GNS. The third chapter is a compilation of articles submitted or to be submitted to peer-view journals. Finally, the fourth chapter makes a conclusion of both literature and experimental work and suggests meaningful future work. The appendices include two articles published with the writer of this thesis as the second author regarding mechanical tests and further simulation of CNTs based composites, and the supporting information for paper 3#.

## References


1. Bacon, R. *Journal of Applied Physics* **1960,** 31, (2), 283-290.

2. Kroto, H. W.; Heath, J. R.; O'Brien, S. C.; Curl, R. F.; Smalley, R. E. *Nature* **1985,** 318, (6042), 162-163.

3. Iijima, S. *Nature* **1991,** 354, (6348), 56-58.

4. Novoselov, K. S.; Geim, A. K.; Morozov, S. V.; Jiang, D.; Zhang, Y.; Dubonos, S. V.; Grigorieva, I. V.; Firsov, A. A. *Science* **2004,** 306, (5696), 666-669.

5. Wallace, P. *Physical Review* **1947,** 71, (9), 622.

6. Sui, Y.; Acosta, D.; Gonzalez-Leon, J.; Bermudez, A.; Feuchtwanger, J.; Cui, B.; Flores, J.; Saniger, J. *The Journal of Physical Chemistry B* **2001,** 105, (8), 1523-1527.

7. Daniela C. Marcano, D. V. K., Jacob M. Berlin, Alexander Sinitskii, Zhengzong Sun, Alexander Slesarev, Lawrence B. Alemany, Wei Lu, and James M. Tour. *ACS Nano* **2010,** 4, (8), 4806-4814

8. Wang, C.-C.; Ying, J. Y. *Chemistry of Materials* **1999,** 11, (11), 3113-3120.

9. Chen, J. S.; Wang, Z.; Dong, X. C.; Chen, P.; Lou, X. W. *Nanoscale* **2011,** 3, (5), 2158-61.

# CHAPTER 2: LITERATURE REVIEW

## 1. Introduction to Carbon Family

Carbon is an amazing element with diverse hybridizing types due to its unique arrangement of the electrons around the nucleus: for a single carbon atom, there are six electrons around the nucleus, two for each orbital-1s, 2s, 2p, respectively. Therefore, carbon has different allotropes with diverse properties in solid phase (Figure 1.)[1], including the more conventional allotropes such as diamond and graphite, as well as the newly discovered nanocarbon forms such as fullerenes, carbon nanotubes(CNTs) and graphene. In diamond[2], the hybridization type is $sp^3$, four σ bonds are formed as a tetrahedral structure, which give diamonds excellent hardness and high transparency; In graphite[3], numerous layers of $sp^2$ carbon atoms are arranged in a honeycomb lattice with the delocalized π bonding, which makes it dark and conductive.

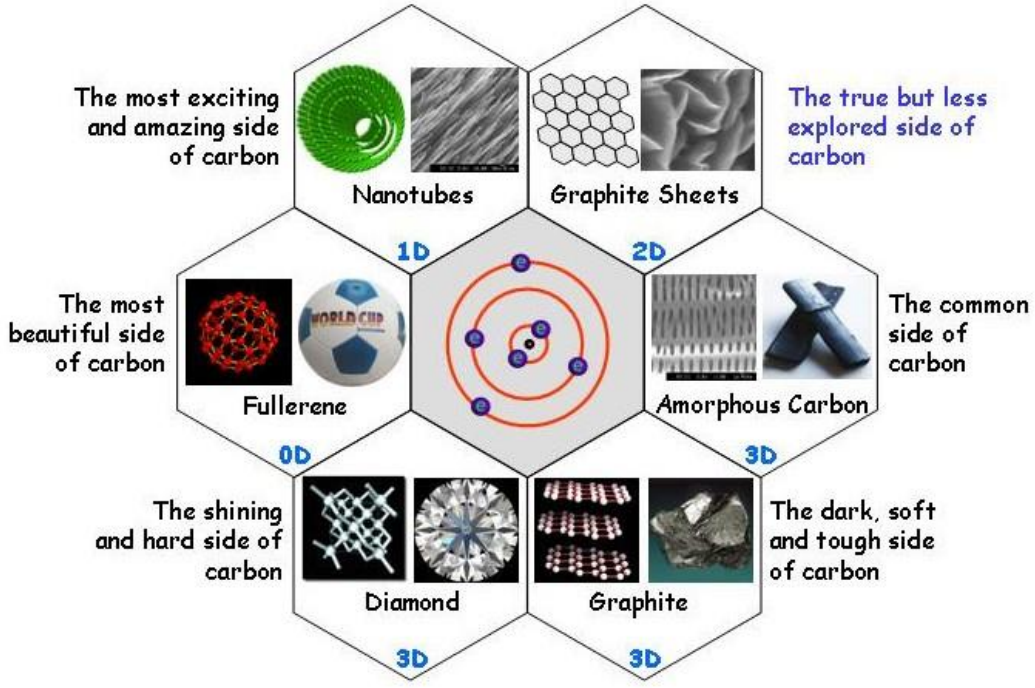


**Figure 1:** Introduction to carbon family[1]

During past century, there has been tremendous development in carbon technology. Carbonaceous materials have been vigorously studied for different applications. In modern industries, carbon almost occurs everywhere: many fundamental materials, such as plastics, fibers, steels incorporate carbon (Figure 2).[4] According to BBC Research, in 2011 the total U.S market for structural carbon materials reached $2.1 billion. The future total market is expected to reach $2.8

billion in 2016, at an annual growth rate of 6.3%. The whole market has been divided into 7 business sectors: aerospace and defense ($1.1 billion in 2011 and 1.5 billion in 2016), industrial applications ($434 million in 2011 and $586 million in 2016), energy ($311 million in 2011 and $461 million in 2016), automotive and other ground transport ($100 million in 2011 and $127 million in 2016), sporting goods ($61 million in 2011 and $64 million in 2016), infrastructure ($12 million in 2011 and $18 million in 2016), and other structural carbon materials ($57 in 2011 and $97 in 2016).

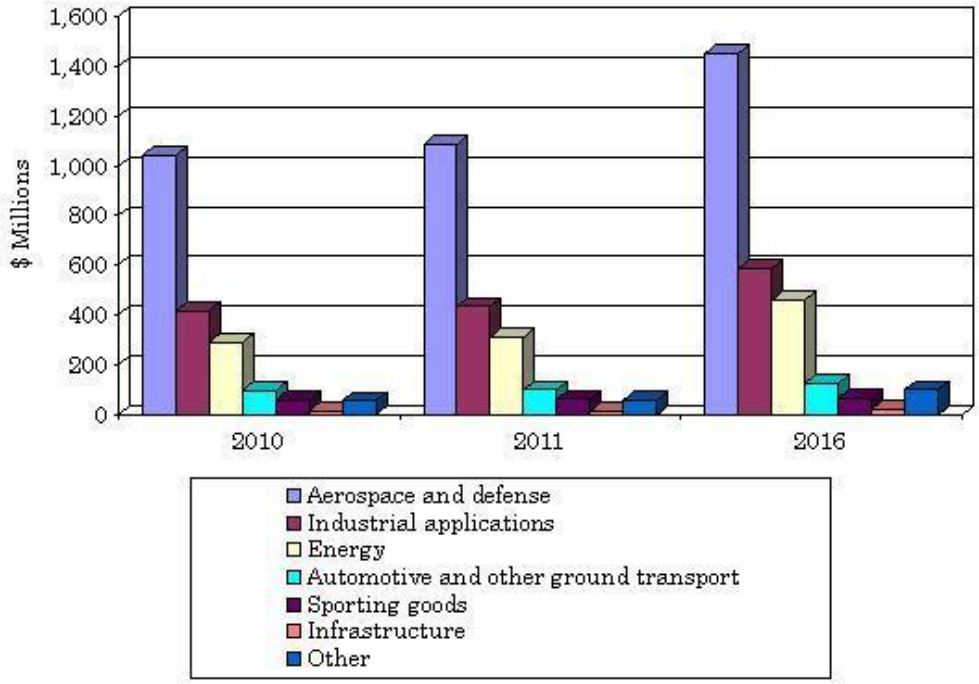


**Figure 2:** U.S market for carbon materials[4]

Although CNTs were synthesized and reported by Bacon's group in 1960[5], they have largely been ignored for decades[6]. In 1980s, the importance of nanotechnology started to be appreciated by more and more scientists. Since materials tend to behave quite differently when they are scaled down to nano size, their amazing properties at nanometer scales have intrigued active exploration in the past three decades. Since the beginning of the surge of nanotechnology, carbon nanomaterials have played an important role. The discovery of $C_{60}$ in 1985[7] declared the arrival of a new carbon era.

## 2. Carbon nanotechnology

As the latest member of nano carbon family that fills the gap between 3-dimensonal and 1-dimensional structures, graphene was discovered experimentally

in 2004. Graphene is considered to be the mother of various carbon allotropes (Figure 3): wrapping a graphene into a ball-like molecule leads to fullerene (0-D); rolling a graphene into a tube forms a carbon nanotube (1-D); disordered stacking graphene nanosheets will form graphite (3-D).

## 2.1 Fullerenes

Fullerenes (Figure 4) are a series of ball-like carbon molecules ($C_{44}$, $C_{60}$, $C_{70}$, $C_{90}$, $C_{180}$ and $C_{540}$, etc.), which belong to a family of graphene, because its dominating bonding type is still $sp^2$. $C_{60}$ was the very first fullerene to be discovered by Kroto, Smalley and their coworkers from Rice University in 1985, which is formed by 20 hexagons and 12 pentagons in a single cage shaped molecule[7]. The discovery of fullerenes is considered as one of the most important discoveries in 20$^{th}$ century. Kroto and Smalley were awarded the Noble Prize of Physics in 1996. After decades of development, fullerenes can now be produced in bulk quantity. In the year of 2004, the annual production capacity of fullerenes reached 1,500 metric tons[9]. Nowadays, fullerenes and their derivatives are available through many manufacturers all over the world, such as Solaris Chem Inc. and American Dye Source Inc., etc.

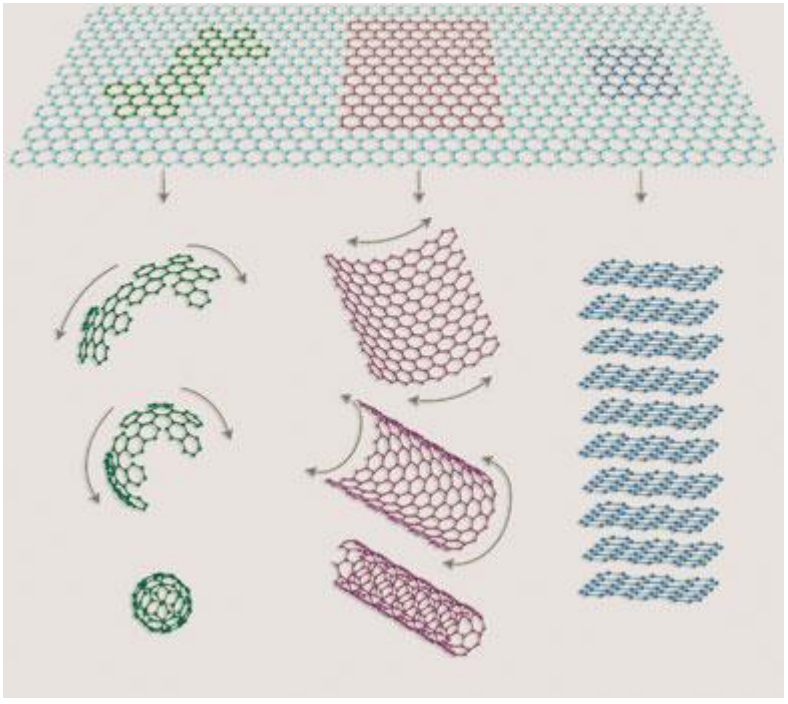

**Figure 3:** Graphene is considered to be the mother of all graphitic forms[8]

Due to the highly bended plane, fullerenes have shown some interesting physical properties: they have different solubility in diverse organic solvents[10]; fullerenes also show outstanding optical limiting feature at a wavelength of 532nm[11];

besides, doped fullerenes can be superconductive[12]. Furthermore, because of extremely high electron affinity, many fullerenes and their derivatives have demonstrated outstanding catalytic performance[13]. Those properties granted them wide-ranged applications in many different fields, such as optical and electronic devices, photosensitive elements, electrochemical sensors, biochemistry and hydrogen storage.

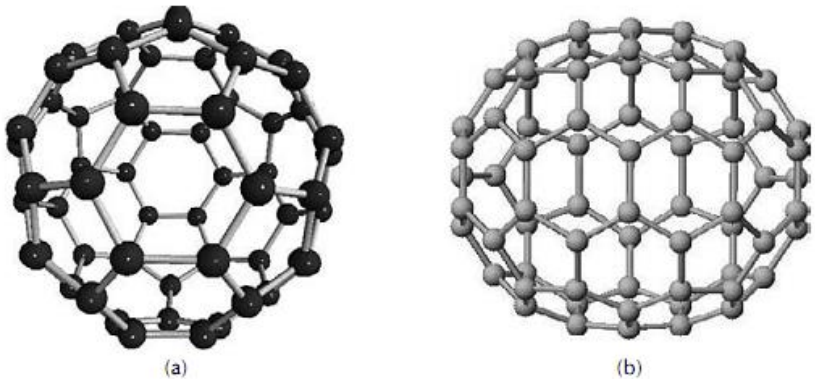


**Figure 4:** Models of the first fullerenes discovered, C60 and C70.[6]

## 2.2 Carbon nanotubes

Six years after the discovery of fullerenes, another allotrope of nanocarbon family—CNTs was claimed by Iijima's group[14]. CNTs can be considered as a hollow cylinder formed by wrapping one graphene sheet (single walled carbon nanotubes) or multiple graphene sheets concentrically (multiple walled carbon nanotubes). Similar to graphite, CNTs are chemically inert. It is considered as a 1-D carbon nanomaterial with its diameter in nanometer range and length in centimeter range. Because of its unique dimensions, micro structure and physical properties, this novel carbon nanomaterial soon took over the center stage of nanotechnology research. Different synthesize routines have been developed, including arc-discharge, laser ablation and chemical vapor deposition (CVD), etc. Furthermore, CNTs produced by various methods have been carefully characterized and studied for diverse applications: energy storage, CNTs composite, solar cells and biosensors, etc. As a result, publications and patents related to CNTs keep increasing for decades (Figure 5). According to an article published by Journal of Science, the annual production of CNTs increases more than 10-fold from 2006 to 2011.

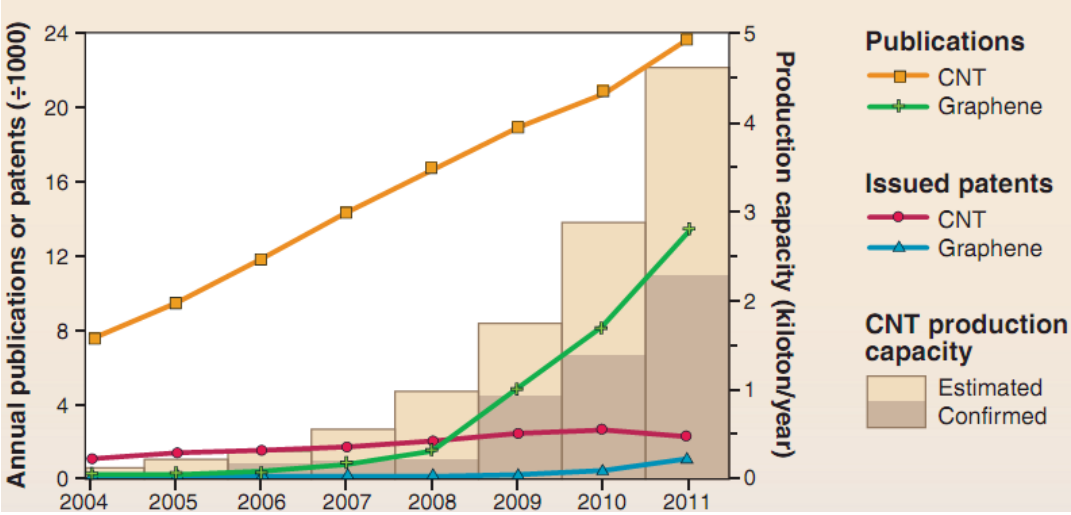


**Figure 5:** Trends in CNT & graphene research and commercialization[15]

## 2.3 Graphene

While CNTs were studied extensively, in 2004, a new member of nanocarbon family came into people's sight: graphene nanosheets. According to previous theoretical calculation, graphene was not stable due to thermal fluctuations in room temperature[8, 16-18]. However, in 2004, for the very first time, Novoselov and Geim demonstrated that this novel 2-D material[19] can be fabricated through mechanical exfoliation from bulk graphite by a Scotch tape. Perfect graphene only contains hexagonal rings, which are formed by carbon atoms. Due to its outstanding properties– high carrier mobility ($2*10^5 cm^2/(V\ s)$), extraordinary stiffness (Young's modulus 1.1TPa), excellent conductivity ($10^6 S/m$), etc., this novel carbon nanomaterial opened a new field and Novoselov & Geim were awarded the Noble Prize for in Physics in 2010 for their discovery (Table 1).

Table 1: Prizes awarded for discovery of nano carbons

| Prize | Year | Winner | Discovery |
|---|---|---|---|
| Nobel Prize | 1996 | Kroto& Smalley | Fullerene |
| Benjamin Franklin Medal in Physics | 2002 | Iijima | Carbon nanotubes |
| Nobel Prize | 2010 | Geim& Novoselov | Graphene |

# 3. CNTs: synthesis, characterization and applications

## 3.1 Structure of Carbon nanotubes

CNTs are the hollow cylinders formed by concentrically rolled graphene nanosheets. Because of the different number of layers of graphene nanosheets, CNTs are classified into single walled CNTs (SWCNTs), double walled CNTs (DWCNTs) and multiple walled CNTs (MWCNTs) (Figure 6). Iijima and his co-workers first reported the successful synthesis of SWCNTs 2 years after their report of MWCNTs[24]. With the assistance of STM, the hexagonal structure can be resolved (Figure 2).

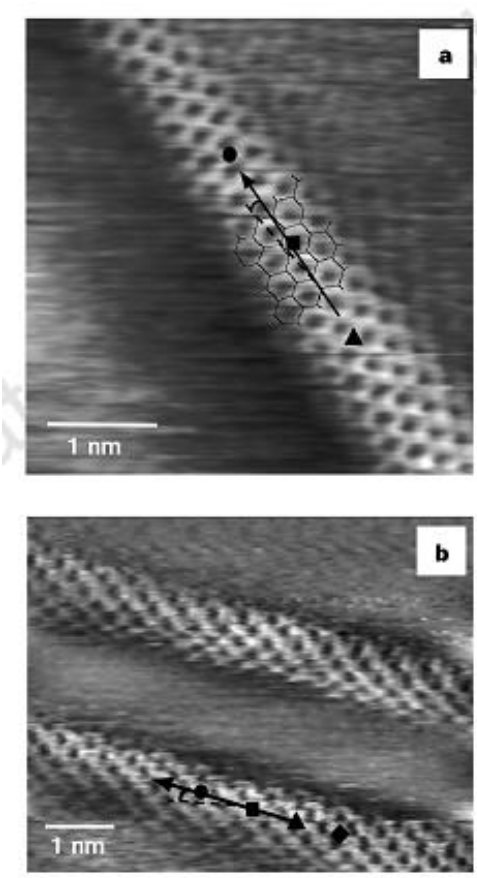


**Figure 6**: Atomic structure and spectroscopy of metallic SWNTs. STM images of (a) SWNT exposed at the surface of a rope and (b) isolated SWNTs on a Au(111) substrate[25].

We can take SWCNT as an example for simplicity. SWCNT is formed by a single layer of graphene nanosheet, which can be described with a vector C. According to the vector of graphene nanosheets, $a_1$ and $a_2$, vector C can be written like this:

$$C = na_1+ma_2 \quad (1)$$

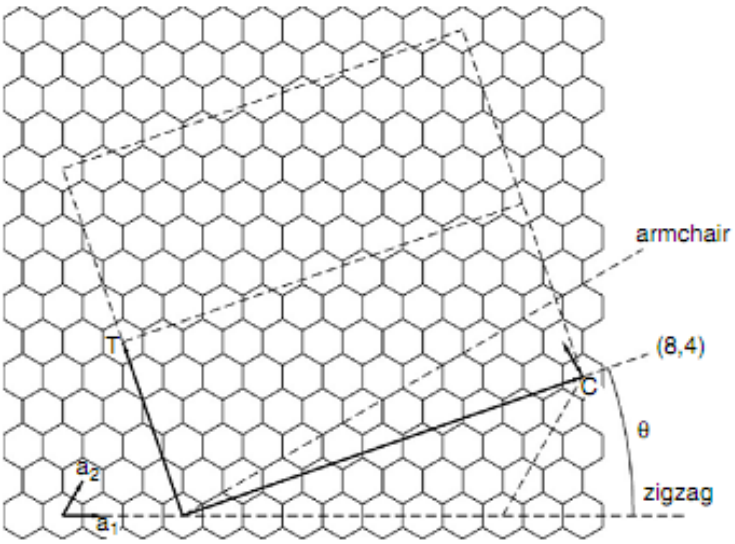


**Figure 7:** Rolling graphene nanosheet to form a SWCNT[27]

When the graphene nanosheet is rolled until two ends of vector meet, a SWCNT is formed, the diameter can be calculated as below:

$$D = | C |/ \pi = a (n^2 + nm + m^2 )^{1/2} / \pi \qquad (2)$$

Where a is the lattice parameter, which is equal to $|a_1|$ and $|a_2|$. Generally speaking, CNTs are arm-chair nanotubes when m is equal to n; when m equals to zero, CNTs are classified as the zigzag type, the other variation are all classified as the chiral type (Figure 8). Both calculations and experimental studies have confirmed that in CNTs, C-C bonding's average length is 0.142 nm, and the average distance between neighboring walls is 0.34nm[26], which is identical to the interlayer spacing of graphite. Chirality is a very interesting property of CNT's structure that has a huge influence on their electronic and optical properties, which will be discussed in the following sections.

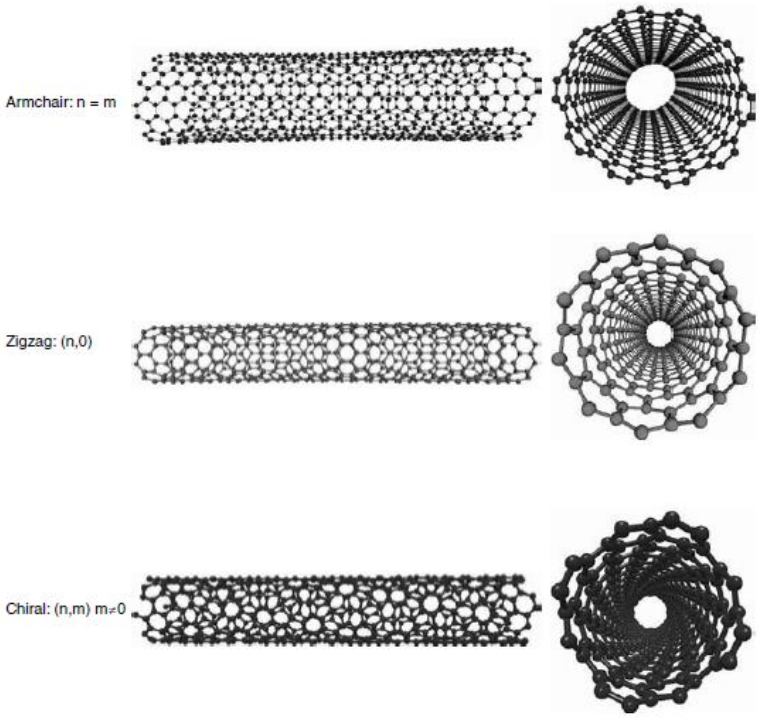


**Figure 8:** Three types of SWCNTs (armchair, zigzag and chiral) [6].

## 3.2 Properties of carbon nanotubes

As a novel 1-D nanomaterial, CNT offers many advantages: low densities, chemically inert and high stiffness. In addition, scientists have been able to decorate the surface of CNTs or dope CNTs to induce and enhance their advantageous properties for different purposes.

Nowadays, they are widely used in field emission devices[21, 28], CNT-polymer composites[22, 29, 30], bio or gas sensors, etc[31-34]. In this project, mechanical, optical and electrical properties of CNTs are most relevant. Thus, these properties are reviewed in the following subsections.

### 3.2.1 Mechanical properties

Compared to traditional materials, CNTs have extraordinary stiffness and Young's modulus (Table 2), which is considered a result of σ bonding from the covalent $sp^2$ bonds, one of the strongest chemical bonding in the world. Both experiments and theoretical calculations[35-37] have indicated that CNT is the 1-D material with the highest strength (number) along axis. Compared with diamonds (420GPa), CNTs' demonstrate even higher hardness of 462~546GPa with much lower densities.

**Table 2:** Comparison of mechanical properties of different materials[38-43]

| Material | Young's modulus (TPa) | Tensile strength (GPa) | Elongation at break (%) | Density |
|---|---|---|---|---|
| SWNT | ~1.2 | 13–53 | 16 | 1.3~1.4g/cm$^3$ |
| MWNT | ~1 | 150 | 10 | 2.1g/cm$^3$ |
| Stainless steel | 0.2 | 2.5 | 15–50 | 8.03g/cm$^3$ |
| Graphite | 0.35–0.18 | 2.5 | 1~1.5 | 2.09~2.23g/cm$^3$ |
| Graphene | 1.1 | 125 | | 2.1g/cm$^3$ |

When CNTs are formed by wrapping graphene nanosheets, the axial component of σ bonding increases rapidly, this phenomenon is believed to be the cause of CNTs' higher strength than that of graphite. Young's modulus of CNTs does not depend on the chirality but on the diameter, which reaches the highest when diameter is around 1nm[44]. In MWCNTs, the Van de Waals force will also contribute to the Young's modulus. Thus, MWCNT's Young's modulus is typically higher than that of SWCNTs.

CNTs also show excellent elastic response. For most materials with high tensile strength, their elongation strains are usually less than 1%. For comparison, experimental result indicates that elongation in CNTs can be up to 15% before they break[39]. This result is also supported by theoretical calculation[45]. All of CNTs' elastic strains are non-linear, which is considered to be caused by re-hybridization and releasing of $sp^2$ bonding [6].

### 3.2.2 Optical properties

Diverse technics such as Fourier transform infrared spectroscopy (FTIR)[46, 47], ultraviolet-visible (UV-VIS) meter[48] and Raman spectrum[49, 50], have been employed to study the optical properties of CNTs. An individual SWCNT with certain diameter and chirality has a fixed band gap, which is preferred by optical scientists. Different SWCNTs have different band gaps that are determined by their different diameter and chirality. Thus, there are metallic CNTs and semiconducting CNTs depending on their band gaps. Figure 9 shows that density of states (DOS)~energy transition energy, metallic CNTs and semiconducting CNTs behave quite differently due to their different band gaps and different electronic density of states. Optical properties of CNTs depend on the electron transitions along the 1-D direction. Unlike 3-D materials with continuous DOS, SWCNT's DOS is discrete. This unique property has resulted

in recently reported non-linear absorption features in CNTs especially SWCNTs: when CNTs are laminated by a laser with a wavelength of 1064nm, pulse width of 35ps, an obvious non-linear absorption behavior was observed[52]. Wei's group[23] observed electro-luminescence spectrum peaks at 407, 417 and 655nm, which was attributed to the discrete DOS. Besides, the optical polarization property of CNTs is quite attractive. Compared with other polarizing materials, CNTs demonstrated higher efficiency, stable electric resistance and relatively stable structure. Those outstanding optical properties have indicated that CNTs have a huge potential in this area.

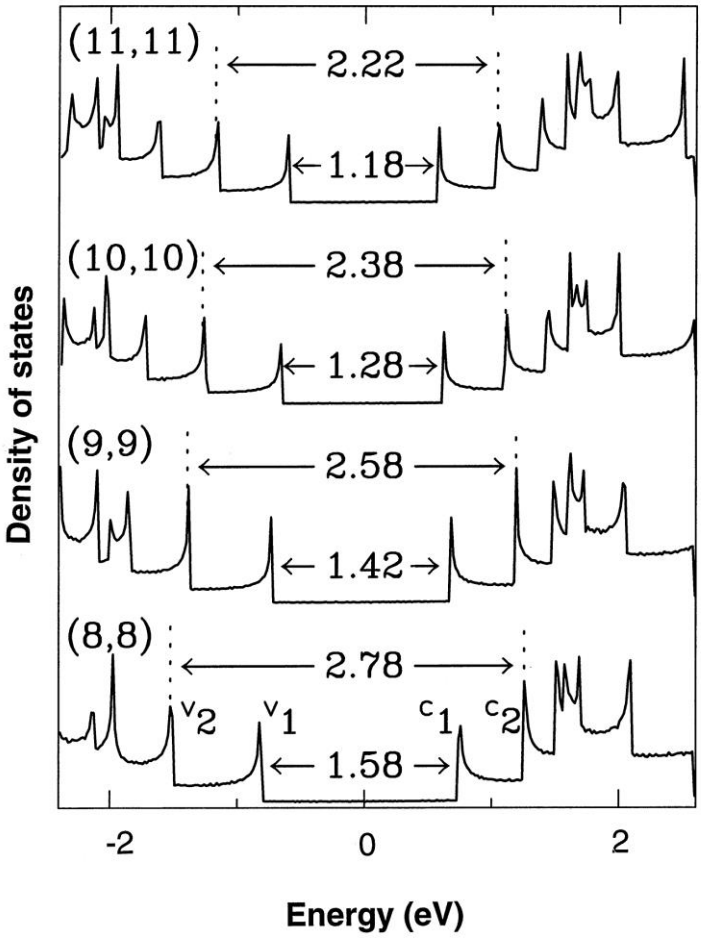


**Figure 9:** Electronic density of states for armchair nanotubes[51].

### 3.2.3 Electrical properties

CNTs' electrical property is determined by their diameter and chirality. SWCNT with (n,m) chirality, it is metallic only when (n-m) is an integer multiple of 3 while others are semiconducting. Therefore, referring to the model built up by the scientists, 1/3 of SWCNTs are metallic while the rest of them are all semiconducting

ones, which is confirmed by synthesis[53].

Early theoretical studies, predicted exceptional electric properties[54, 55] in CNTs that were experimentally confirmed after Iijima's report[56-59]. For a simplest model, the electric properties of CNT can be derived by a relation from dispersion of graphite[54, 55]:

$$E(k_x, k_y) = \pm\gamma\{1+4\cos(\frac{\sqrt{3}k_x a}{2})\cos(\frac{k_y a}{2}) + 4\cos^2(\frac{k_y a}{2})\}^{1/2} \quad (3)$$

Where ($k_x$, $k_y$) are the wave vectors, γ is the closest hopping parameter and a is the lattice parameter.

**Table 3:** Transport Properties of Conductive Materials[43, 61]

| Material | Thermal Conductivity (W/m ƙ) | Electrical Conductivity (s/m) |
|---|---|---|
| Carbon Nanotubes | > 3000 | 106 - 107 |
| Copper | 400 | 6 x 107 |
| Carbon Fiber - Pitch | 1000 | 2 - 8.5 x 106 |
| Carbon Fiber - PAN | 8 - 105 | 6.5 - 14 x 106 |
| Graphene | 5000 | 2000 |

When diameter is less than 25nm, CNTs will exhibit property of quantum transition. On the wall of CNTs, there are always some coupled pentagons and heptagons, which are called "defects". Different defects as well as their density and distributions influence the electrical property of CNTs[60]. There have been numerous reports regarding the comparisons between CNTs and other conventional materials (Table 3)—for a highly ordered SWCNT sample, the resistivity is about 0.4μΩ·m under room temperature and even lower, which indicates that CNT has shown excellent conductivity. This amazing phenomenon is due to the re-hybridization of σ-π bonding, which makes the delocalization of π electrons stronger, thus it brings the better conductivity. When a graphene nanosheet is bended to form a CNT, the π orbits start to aggregate outside the tube, becoming more delocalized, which causes the increase of conductivity. It is reported that resistivity decreases along with the temperature, which is due to the contact, coupling, and defects among the CNTs.

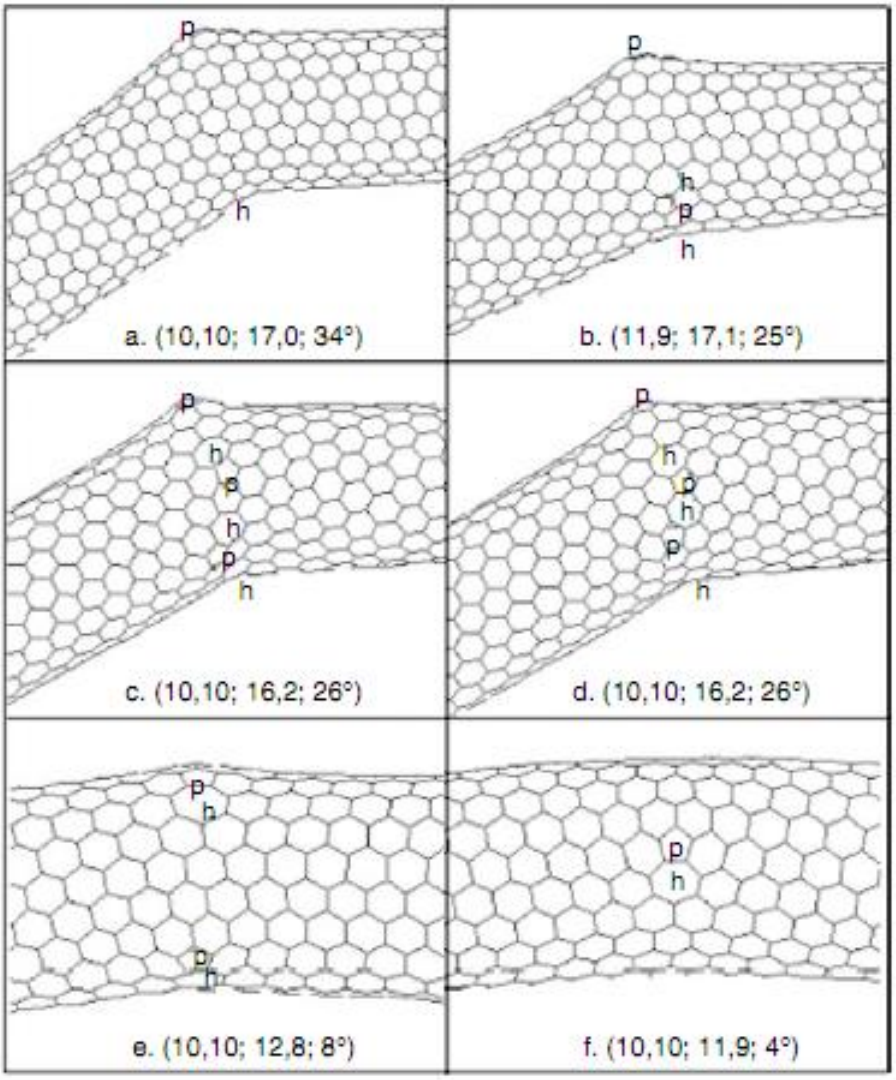


**Figure 10:** Examples of SWCNT bendings (a) 34 °; (b)~(d) 26 °bending with different arrangements; (e) 8 °(f) 4 °[62]

In addition, because of the sharp curvature at the tip of a CNT, it serves as an interesting part because its curvature is nano size, this means CNTs can be considered as an excellent emission electrode.

## 3.3 Synthesis of carbon nanotubes

As discussed previously, CNTs show different properties depending on their individual structures and rolling directions. In recent years, because of their wide-ranged applications, the market of CNTs keeps growing. Synthesis and manufacturing of CNTs with controllability over their structure and properties is of great importance. Several methods — including chemical vapor deposition[63, 64],

arc-discharge[14], laser ablation and high-pressure carbon monoxide have been developed and extensively studied. Each of them has its own advantages and disadvantages, which will be discussed in this section.

### 3.3.1 "Top-down" methods

There are two methods—including arc-discharge and laser ablation starting from bulk graphite, which are considered as top-down approaches.

**(1) Arc-discharge synthesis**

This method was the first employed to synthesize CNTs[5, 14]. The typical setup is shown in Figure 11. Inert gas at certain pressure is introduced into the reaction vessel to provide protective atmosphere. When the power supply is turned on, an arc will be generated between two graphite electrodes[65]. $C_{60}$ can also be synthesized by a similar method. In the early stages, only MWCNTs were reported by using arc-discharge method. Iijima and other groups developed different catalysts for SWCNTs synthesis for this method. However, an important issue noted in many reports is the large amount of impurities produced along with SWCNTs. How to purify the as-made product and retaining beneficial structure as well as properties of SWCNTs was studied as an essential problem. In order to synthesize SWCNTs with high purity, researchers tested catalyst systems, including binary metallic catalysts[66-68]. Hisashi and his co-workers fabricated the anode by incorporating Fe, Co, Ni and FeS into graphite, this method can produce SWCNTs with extremely high purity (up to 90%)[66] and great graphitization[69].

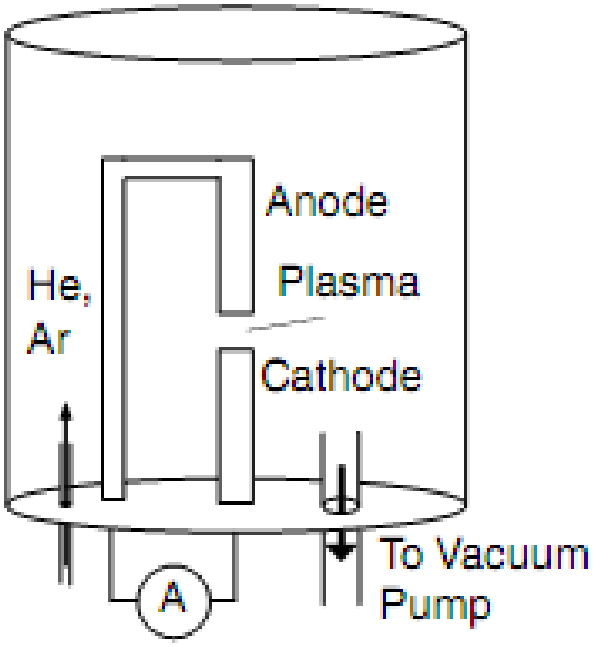


**Figure 11:** Setup of arc discharge method[6]

*Mechanism* The mechanism of this growth method has been extensively studied and well developed[70]. For a typical arc-discharge method[71]: Graphite is ionized by the plasma, by which the flow of carbon ions are accumulated above the pillars. This flow is the raw material for the tube-shape growth. Helium buffer gas was flushed with carbon ions above the pillars, followed by being pushed to the edge, back to the plasma above zone 2[44]. This flow can be considered the major feedstock for column growth. The helium buffer gas drawn in by the carbon ion flux to the top of the pillars is swept to the side, and then returns back to the plasma over zone 2, which is the intermediate area between adjacent columns.

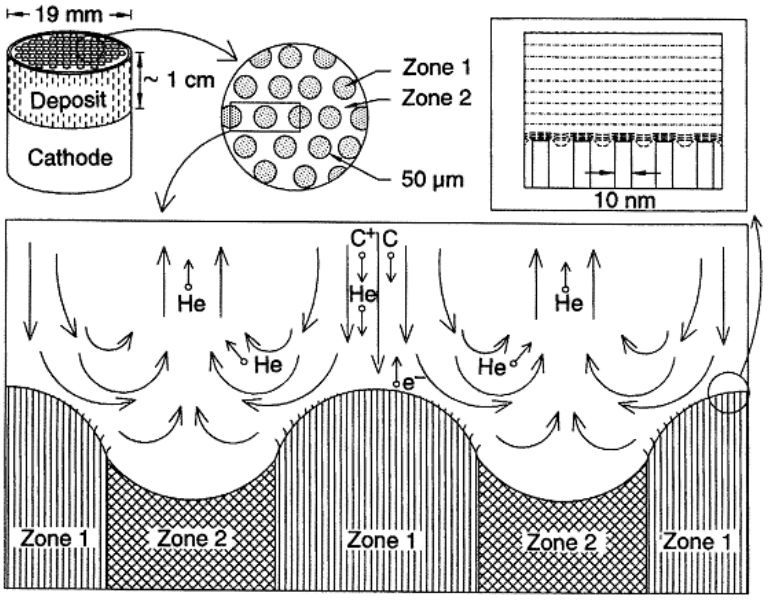


**Figure 12:** Developed modeling of Arc-discharge method[71].

Ejection of electrons constantly occurs everywhere around the pillar structure. By scientists' observation, most of the carbon deposited on the pillar will be vaporized to form gaseous bundles, which is the original source of fullerenes and CNTs. Those small bundles are attached to the top of the graphite anode due to the large amount of positive charge they carried. These small bundles begin to collect at the top of the graphite anode and are considered as the new raw materials for CNTs growth.

**(2) <u>Laser ablation synthesis</u>**

This method was used for the very first time to obtain gram-scale CNTs in 1996, by Smalley group at Rice University[72]. The typical setup is shown in Figure 13. The main routine of this method involves heating the graphite/metal composites with laser pulses, or using continuous illumination to fabricate CNTs. The overall quantity of the products is influenced by some parameters such as light intensity, process temperature and geometry, carrier gas type, pressure, and flow conditions, etc.[73]. This method also requires metal particles to serve as catalyst, but one major drawback is similar to that of arc-discharge method, i.e. there are lots of by-products along with desirable SWCNTs. Besides, cost of this method is too expensive that it prohibits its wide application for bulk-production. Currently, it is as popular as some of other methods.

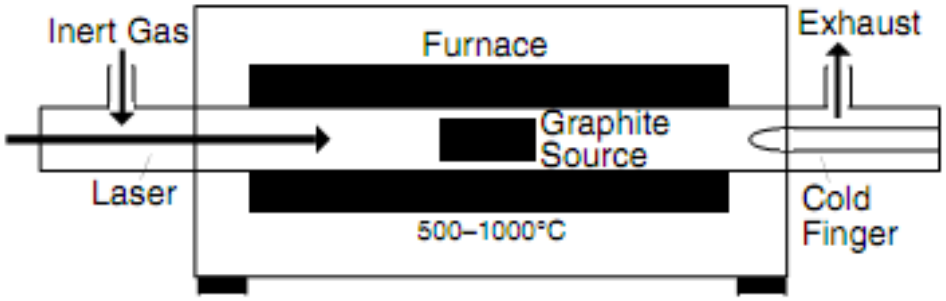


**Figure 13:** Setup of CVD method[6]

### 3.3.2 "Bottom up" method

Gas-phase synthesis methods, including conventional chemical vapor deposition(CVD), plasma-enhanced CVD (PECVD), and pressure catalytic decomposition of carbon monoxide (HiPCO), based on pyrolysis of organic carbon sources to create CNTs are considered as bottom up approaches.

Different methods in this catalog have some in common features: (1) they are all carried out under a 'medium' temperature, i.e. a temperature range from 700~1200 ℃; (2) compared to top down methods, they depend on fewer parameters, mainly thermal energy and catalyst, which results in more controllability. Thus, they are now becoming more and more favorable and adopted by many groups (Table 3).

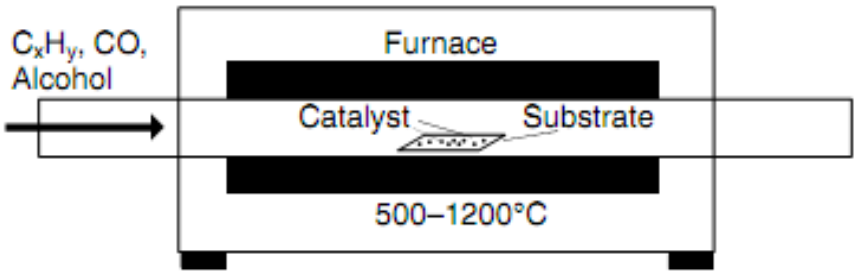


**Figure 14:** Setup of chemical vapor deposition for CNTs synthesis[6].

The well-known report of CNTs synthesized by chemical vapor deposition (CVD) was developed in 1993[74], 2 years after the Iijima's report of CNTs (Figure 14). Although CVD method has been well developed, the mechanism is still debatable. Among proposed theories, the growth of hollow carbon nanofiber is most widely accepted (Figure 15). In this model, the growth process involves the following steps:

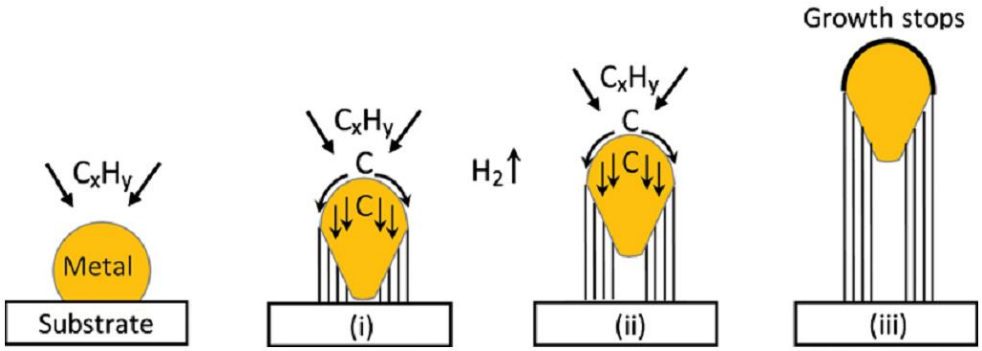


**Figure 15:** Most accepted CNTs growth model: Tip-growth[75].

1. It introduces carbonaceous gas into a tube furnace as the precursor, let it react with the metal particles, which can be considered as nucleation sites to start the growth of CNTs, the feeding gas is converted into carbon atoms on the surface of metal catalyst by pyrolysis;
2. Carbon atoms start to diffuse within those metal nano particles and start to form a graphitic layer at the bottom of those particles;
3. The catalyst is pushed up by the growth of graphitic layer; when the surface of catalyst is totally covered by graphitic layers, the growth of carbon nanotubes stops immediately, and the catalyst stays on the top of those CNTs.

High yield of CNTs is one of the advantages offered by this method. In addition, this method shows very good compatibility with different growth conditions, such as different substrates[76], catalysts[60, 69, 77-79] and feeding stocks[80], etc. Because of this compatibility, the dimension of synthesized CNTs (length, diameter) is much more controllable. CVD method is now favorable method to produce CNTs — both MWCNT and SWCNT in bulk quantities at relatively low cost. The price of SWCNT produced by Carbon Solutions Inc. is now only 50$/2g.

Through years of development, several more sophisticated variations of CVD method are also available: plasma-enhanced CVD (PECVD)[81] and high pressure catalytic decomposition of carbon monoxide (HiPCO)[82], etc.

Table 4: Comparison of different methods for CNTs synthesis[83]

| Method | Arc-discharge | Laser ablation | CVD |
|---|---|---|---|
| Energy required | High | High | Low |
| Cost | High | High | Low |
| Production rate | High | High | High |
| Purification | Required | Required | Required |

| | | | |
|---|---|---|---|
| Design of reactor | Complicated | Complicated | Simple |

### 3.3.3 Purification

Since in most applications, CNTs with high quality and purity are desired, purification of CNTs is a critical post treatment. Usually, the impurities include amorphous carbon, metal nano particles encapsulated in carbon spheres, fullerenes, and other aromatic hydrocarbons. Many methods were developed to purify as-fabricated CNTs, such as thermal oxidization, hydrothermal method, plasma oxidization, acid treatment and high efficiency liquid chromatography. All of those methods can be classified into two catalogs: dry method and wet method.

***Wet method*** Wet purification methods are very popular. As a matter of fact, some of the dry methods require wet treatments to serve as a pretreatment to remove the solid impurities with high melting point, such as metal nano particles. Typically, $HNO_3$ and HCl are used to remove metal catalysts at low cost and with high efficiency[84, 85]. It is well known that in as-prepared CNTs, agglomeration and bundling are unavoidable. Thus, in a typical wet purification treatment[86], CNTs are dispersed in concentrated $HNO_3$, refluxed for extended period of time up to 45 hours. After several vacuum filtration-rinsing cycles, CNT with desired purity can be obtained (Figure 16). Compared with dry method, wet method is considered to be more compatible with following applications of SWCNTs[86-88].

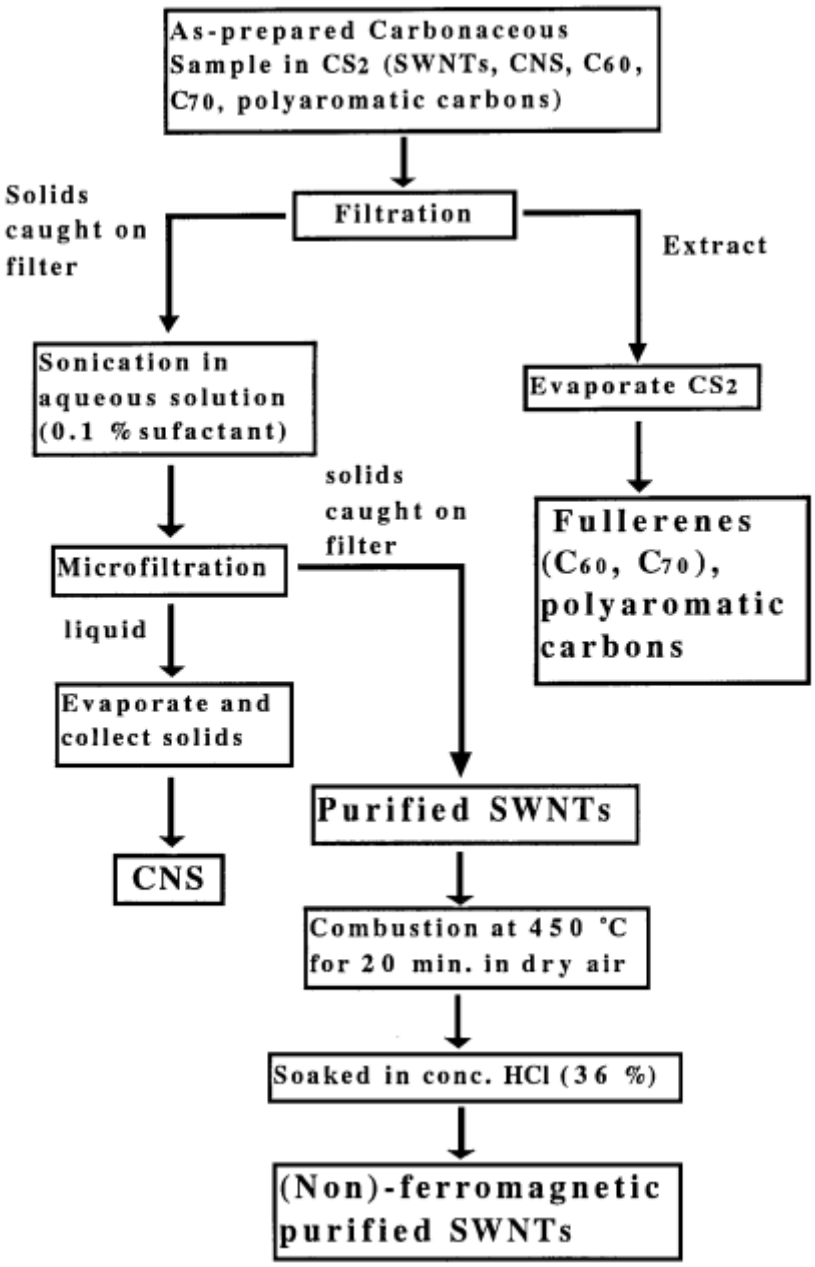


**Figure 16:** Purification procedure to separate coexisting nanospheres and polyaromatic carbons by microfiltration and combustion[89].

***Dry method*** Basically dry method uses gas to treat the as-made sample. Since amorphous carbon is one of the species of impurities and its reactivity is much higher than that of CNTs, gaseous reactions are employed to remove them. For example, amorphous carbon can be removed by oxidation at controlled atmosphere and temperature. However, this method is more suitable for MWCNTs, because SWCNTs are much more reactive. Variations of this simple oxidation approach have been tested to make it applicable to SWCNTs. For example, in order to increase the selectivity of the dry method, Zimmer-man and his co-workers introduced HCl and $Cl_2$ into the air to obtain high purity SWCNTs[90]. However, this method also has an obvious drawback:

compared to the wet method, the efficiency of removing metal catalyst is too low.

## 3.4 Characterization

Characterization techniques are important to evaluate the application potential and, of course, to understand the basic chemical and physical properties of a certain material. Many application methods have been employed to fully investigate CNTs'.

**Electron microscopy: Scanning Electron Microscopy(SEM) and Transmission Electron Microscopy(TEM)**

Electron microscopy is very useful to characterize, monitor in-situ processes of and modify CNTs. For example, SEM enables us to observe the morphology of the SWCNTs, but also to identify the composition of CNTs[91, 92]. TEM enables us to view the detailed microstructure of CNTs, and understand detailed microstructures, and understand their structure-property relationship.

With information obtained from electron diffraction, the formation mechanism of CNTs has been deducted. It is this technique used in Iijima's paper, he and his coworkers could deduct the formation of the CNTs. Besides, with this technique, researchers can also determine other particles (Pt, Ru) present within CNT structures.

**Raman spectroscopy**

The basic principle of this method is to illuminate materials with an incident light at a certain wavelength to cause inelastic scattering on the material. The inelastic scattering absorbs or releases a phonon, and changes the intensity of the incident light [93]. This change can provide information on the detailed bonding, electrical and optical properties and structures of carbon materials[28, 51, 94]. It has been used since 1970s to study carbon or carbon composite materials. And it remains as a powerful tool to study CNTs.

**Atomic Force Microscopy (AFM)**

Compared to EMs, AFM provides even higher resolution and has been widely used to investigate SWCNTs[95, 96]. However, the resolution of AFM is always limited by the shape and mechanical properties of AFM tip. It is interesting to note that due to their 1-dimensional structure and high flexibility, SWCNTs are already employed as AFM tips[97, 98]. A variation of AFM, the scanning tunneling microscopy (STM) is another powerful technique used to investigate SWCNTs in atom scale[99, 100].

Experimental data has shown that it is capable of detecting the defects of CNTs[101-103].

## 3.5 Applications of CNTs

CNTs can be divided into two groups: SWCNTs and MWCNTs. Due to their different structures and arrangements of carbon atoms, they possess different mechanical and electronic properties and are used in different applications.

### 3.5.1 Field Emission Devices

Controlled transportation of electrons in vacuum has enabled many modern technics, such as X-Ray generator, electron microscopy and plasma treating, etc. In general, these technics rely on the control of free electrons either in electric or magnetic fields. One essential factor in these technics is the electron source. Among various of methods to generate free electrons, field emission is considered to be the best choice. Field emission applies strong electric field on the surface of a certain filament to excite electrons[104]. Compared to thermal methods, field emission has the advantages of high current density and high efficiency.

CNTs are considered as a good filament material for field emission devices. Experimental results[105] showed field emission yield of a current density as high as $1A/cm^2$ at low electric intensity (less than $1V/\mu m$) using CNTs. For example, the 4 inch fully sealed CNT-FED panel has been fabricated by Samsung Inc. and operated for 500 h without any significant degradation[106].

### 3.5.2 Composites

Due to CNTs' intriguing properties (mechanical and thermal properties, for example), they have also been incorporated in various composites. For example, MWCNTs were introduced into polymer matrix to serve as conducting constituent. Experimental results (Table 3) shows that little MWCNTs can highly improve the conductivity of the composite and without reducing other properties (strength and Young's modulus); contrarily, once CNTs (either MWCNTs or SWCNTs) are incorporated, those mechanical properties will get a huge increase[107]. For commercial purpose, both MWCNTs and SWCNTs have shown considerable advantages compared to their "ancestor", carbon microfibers due to extremely low percolation threshold[108].

Table 5: Several composite system with enhanced electrical propertie[44]

| Polymer | Nanotube Type | Nanotube Concentration (wt. %) | Percolation Threshold (wt. %) |
|---|---|---|---|
| ABS | SWCNT | 0.5~10 | |
| Epoxy | MWCNT | 0.0225~0.15 | 0.0225~0.04 |
| Polyimide | SWCNT | 0.01~1.0 | 0.02~0.1 |
| PMMA | SWCNT | 0.1~8.0 | <1 |
| Polystytrene | MWCNT | 1~5 | <1 |
| PmPV and PVOH | MWCNT | 0.037~4.3 | 0.055 for both |
| PVOH | MWCNTS | 5~50 | 5~10 |

# 4 Graphene Nano Sheets

Graphene nanosheet(GNS) is a 2-D carbon nano material(Figure 17). It is believed to be a "relative" of CNTs[8], i.e. under certain conditions, they can transform into each other[109]. GNSs possess many exceptional properties, such as 0 band gap, extreme high excellent thermal conductivity (~5000W $\cdot m^{-1} \cdot K^{-1}$)[110], fracture strength (125 GPa)[111] and carrier mobility (200 000 $cm^2 \cdot V^{-1} s^{-1}$)[112], etc. Immediately after its discovery, it was introduced to various applications and different synthesis methods were developed[8, 113].

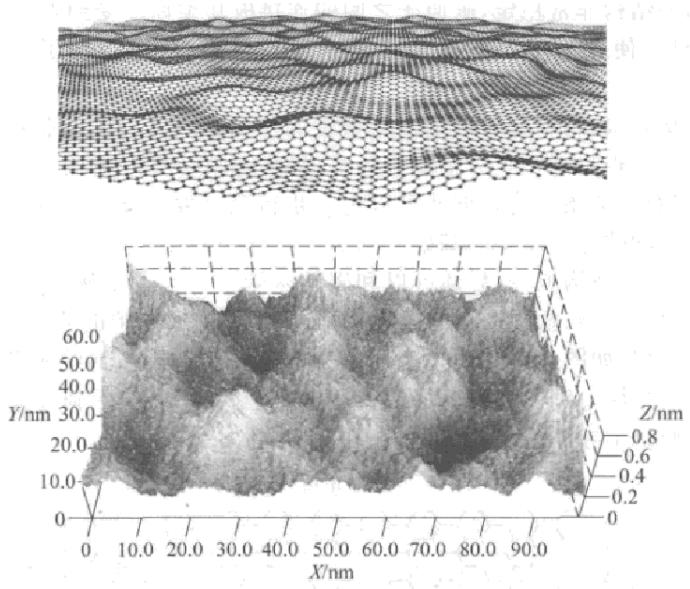


**Figure 17:** Crumbling on graphene nanosheet's surface[114, 115]

## 4.1 Structure of graphene nanosheet

Graphene nanosheet is a mono or multiple layers of $sp^2$ hybridized carbon atoms organized in honeycomb network. The atoms are aligned periodically within the same plane. Every carbon atom is connected to three adherent ones by σ binding (formed by interactions of S, $P_x$, $P_y$ orbitals) by a separation angle of 120 °. The existence of σ bonding results in excellent mechanical properties. Also the π bondings from the $P_z$ orbitals are believed to contribute to the outstanding electric properties of graphene nanosheets[116].

It is well known that ideal 2-D materials are not thermodynamically stable under room temperature, and that is why for over 60 years graphene only exited in theory[117]. According to the observation under TEM and SEM, mono layer of graphene nano sheet is still not completely flat, gentle crumbling can be easily found in graphene nanosheet[114]. Thus, GNS is considered as a 2-D material only when the area is large enough[118].

## 4.2 Properties of graphene nanosheet

### 4.2.1 Mechanical properties

As discussed above, within GNS plane, carbon atoms connect to each other by σ bonds, which gives GNS exceptional mechanical properties. Lee and his co-workers conducted mechanical test by AFM and obtained the Young's modulus and fracture strength of GNS to be 125GPa and 1000GPa, respectively[111]. Therefore, GNS has received the name of "strongest materials ever"[119]. Beside the experiments, theoretical calculations have been also employed to estimate those mechanical properties, which perfectly meet with the experimental results[111]. Compared to stainless steel, ideal GNS thin film's tensile strength is 200 times stronger[120]. These results strongly suggest that GNS can be a promising reinforcing component for construction of various composite materials.

### 4.2.2 Optical properties

GNS has outstanding optical properties. Both theoretical and experimental results show that GNS has high optical transmission (97.7%)[121]. According to principles of reflection and interference, different colors and contrast will result from different number of layers of GNS[122]. Similar to CNTs, GNS exhibits saturable absorption behavior at near infrared wavelength range, this property implies that GNS

can be a promising material for fiber laser generator (Figure 18)[123].

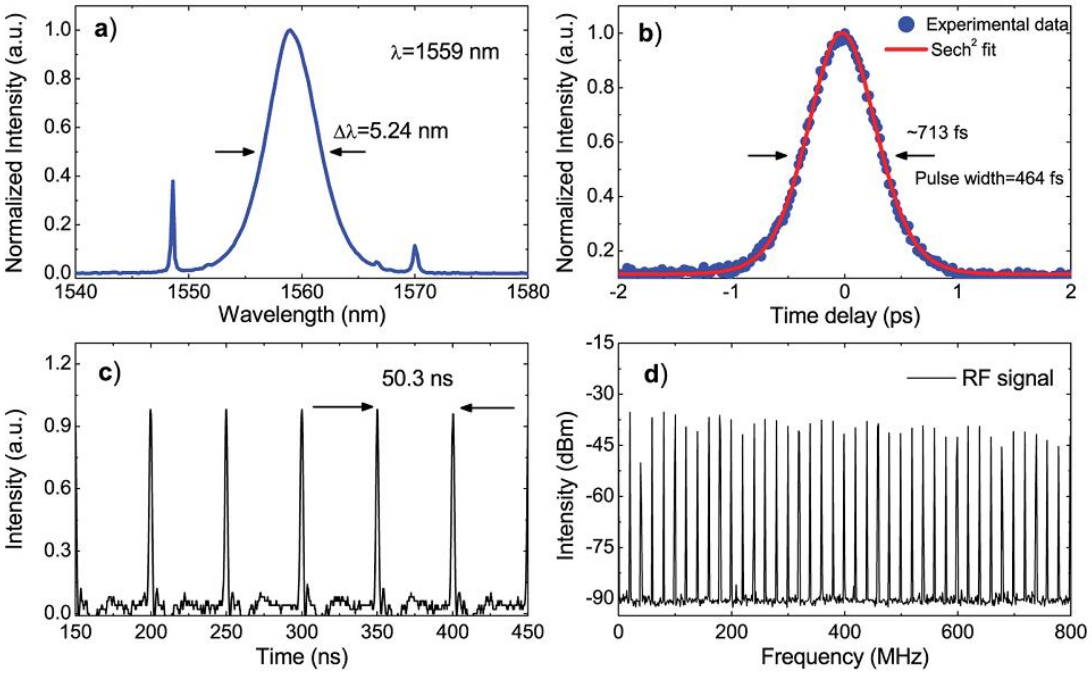


**Figure 18:** Mode-locked pulses characteristics. (a) Output spectrum; spectral resolution 0.1 nm. (b) Autocorrelation trace of output pulses; delay resolution 20fs. (c) Oscilloscope trace. (d)Wide band RF spectrum up to 0.8 GHz[124].

.

### 4.2.3 Electric properties

As mentioned previously, the π-π bonds in GNS contribute to the extraordinary electric properties. The mobility of electrons within GNS plane can be as high as $2*10^5 cm^2/(V\ s)$[125] and its conductivity can reach $1*10^6 S/m$[126]. Besides, GNS is a semi-metal with a 0 band gap[127]. Every unit cell of GNS is formed by 2 carbon atoms (Figure 19), with two conical points touching each other[116]. This unique band structure separates the cavities and electrons so that irregular quantum hall effect occurs, which results in semi-metal behavior. Additionally, Heersche and his group also detected superconductivity in GNS[128].

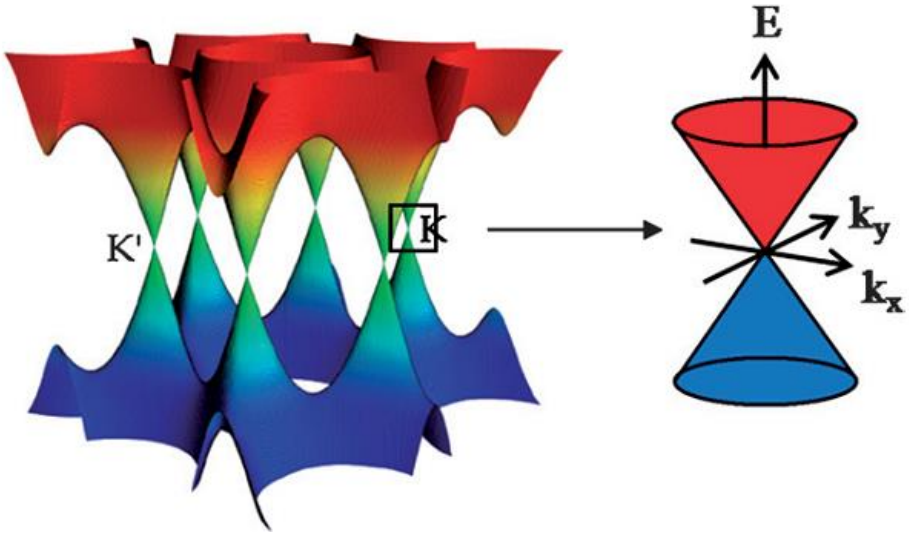


**Figure 19:** Band structure of GNS[116]

### 4.2.4 Thermal properties

Under room temperature, the thermal conductivity of GNS can go up to $5.30*10^3 Wm^{-1}K^{-1}$, as reported by Balandin and his co-workers[110]. In their study a single layer of GNS was deposited on a $Si/SiO_2$ substrate, the sample was illuminated by an incident of laser and the reflected laser's energy were collected to make contrast, then the thermal conductivity can be calculated. The result of this experiment shows that thermal conductivity of GNS is much higher than other carbon nanomaterials (Table 2).

## 4.3 Synthesis of graphene nanosheet

The first reported method to obtain graphene was mechanical exfoliation of graphite[19] by A. K. Geim and K. S. Novoselov in 2004. The two researchers were awarded Nobel Prize in 2010 because of this great work. But this original method was proven to be time consuming and lack of efficiency. During past few years, extensive attention has been paid to developing synthesis methods with improved controllability over properties and dimensions of GNS at large scale and low cost. Several methods have been extensively studied, including CVD, epitaxial growth, chemical reduction of graphite oxide and graphite intercalation compounds and arc-discharge, etc. Similar to CNT synthesis, these methods can be divided into two catalogs: top-down and bottom-up. Table 6 summarizes the popular fabrication methods.

**Table 6:** Comparison of different methods for graphene synthesis[43]

| Method | Mechanical exfoliation | Epitaxial growth | CVD | Chemical reduction |
|---|---|---|---|---|
| Energy required | High | High | Low | Low |
| Cost | High | High | Low | Low |
| Production rate | Low | Low | High | High |
| Size | Small | Small | Large | Large |
| Compatibility | Low | Low | Low | High |

### 4.3.1 "Bottom up" methods

1. CVD method

This method was first reported in 2006, graphene was synthesized on transition metal foils (Figure 20)[129]. Quite similar to CVD synthesis of CNTs, advantages include low cost, environmental friendliness, mild temperature, etc. In the earlier developments it was really hard to control the thickness of fabricated graphene. The synthesized samples typically contained 35 layers[129]. Later, as the precursor was changed from camphor to $H_2$ and $CH_4$, substrate switched from Ni to $Si/SiO_2$, an ultra thin graphene with thickness from 2~3 layers of monolayer graphene was obtained[130].

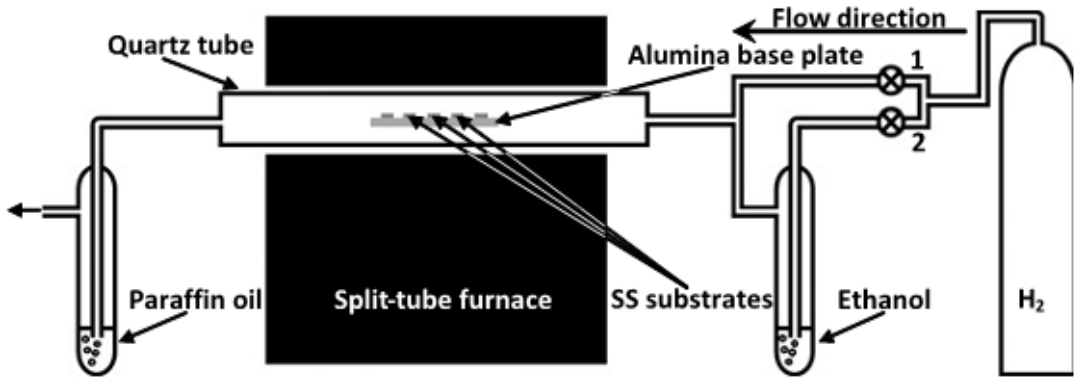


**Figure 20:** Schematic setup of CVD method for GNS growth[131]

More recently, GNS has been synthesized on different substrates, like SiC, Si, and Cu, etc[130, 132] with good quality. However, precise control over the number of layers at a wafer scale, still remains to be difficult.

***Mechanism***

1. On Cu substrate

Cu is one of the transition metal to serve as a catalyst in the growth process, called self-limiting process[133]. Ruoff's group reported that, the whole process involved the following steps(Figure 21(b)):

(1) First of all, carbon atoms are formed by decomposing methane;

(2) Secondly, carbon keeps growing and thus starts to nucleate on the substrate surface;

(3) Then the nuclei keep expanding until the whole substrate is covered by graphene.[133]

2. On Ni substrate

Ni is widely used to serve as catalyst to grow CNTs and GNS by CVD. It was employed to catalyze the decomposition of carbonaceous gas under mild pressure and temperature, and formation of ultrathin graphite film on its surface. Li and his coworkers proposed a so-called segregation mechanism[134]:

(1) First of all, hydrocarbon feedstock is decomposed by assistance of Ni;

(2) Segregation and precipitation;

(3) Finally, by a surface adsorption procedure, an ultrathin graphite film can be formed on the substrate(Figure 21. (a)).

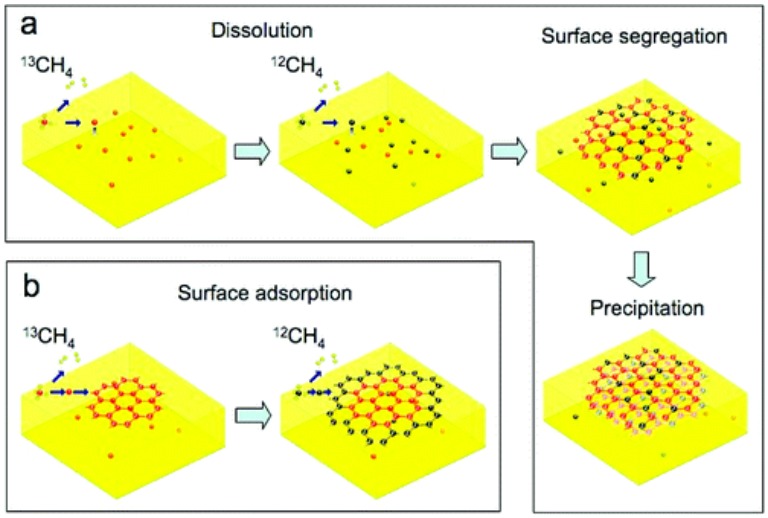


**Figure 21:** Schematic diagrams of the mechanism on different substrates: (a) On Ni(b) On Cu[134]

## 2. Arc-discharge method

Arc-discharge method has also been used to synthesize graphene nanosheets. The setup is very similar to the one for CNTs fabrication. The sample made by this method has shown great crystallinity and high thermal stability because the healing effect of the high plasma temperature and the etching effect of the $H_2$[135]. The

concentration of mixed atmosphere and discharge current can be varied in this method. Rao's group[136] found that when discharge current was within 100~140A, in an $H_2$/He mixture atmosphere, GNS with perfect graphitization can be synthesized. Furthermore, the contribution of $H_2$ to the conductivity and thermal stability was also studied[43].

### 3. Epitaxial Growth of Graphene

The growth of graphitic layers by the sublimation of Ni substrates has been known since 1970 (by Eizenberg)[137]. To meet the need of synthesizing uniform graphene layers, this method revived recently[138]. In principle, this method utilizes the sublimation rate differences between silicon and carbon under high temperature to leave the carbon behind on the substrate surface, and then rearrange them to form graphene layers. Many silicon-based substrates have been tried out and more and more high quality and free standing graphene nanosheets were synthesized. Srivastava's group introduced microwave to this process, they fabricated petal-like GNS on a Si substrate coated with Ni[115]. It was pointed out that power of the microwave will influence the morphology of GNS. Zhu and his co-workers[139] developed a catalyst-free method assisted by plasma and obtained a final product that was close to single layer of graphene. It was also found that substrate could have a significant effect on the electric property of GNS surface, as reported by Heer's group[140].

## 4.3.2 "Top down" methods

Chemical reduction and thermal reduction of graphene oxide are the most common method in top-down catalog. Chemically exfoliating natural graphite by certain oxidants followed by the reduction step has been considered as one of the most efficient ways for easy and scale-up production of GNS. In this method, GNS can be dispersed in organic solvents and can be conveniently deposited on any substrate by simple processes—like spin coating, for example. The first step is using strong oxidation of natural graphite to produce graphene oxide[141]. In this step, lots of functional groups (epoxide, hydroxyl, carbonyl and carboxyl) are introduced to weaken the van der Waals interactions between layers. The obtained graphene oxide is then reduced and most of the functional groups are removed in the reduction step.

There are mainly two ways to reduce the graphene oxide: chemical reduction[142] and thermal reduction[143].

**Chemical reduction**

With graphite oxide powder completely dispersed in organic solvent, strong reducing agent, like hydrazine[113], $NaBH_4$[144], GNS can be synthesized. Stankovich used hydrazine to reduce graphite oxide, which was fabricated by Hammer's method, the final product, GNS, was obtained[113]. However, Due to the strong Van de Waal's force, those nanosheets tended to aggregate[43]. Zhang's group developed an easy reducing process, which used KOH as reductant, a stable, well dispersed GNS suspension was synthesized[145].

**Thermal reduction**

The mechanism of this method is to thermally decompose the oxygen-contained functional groups within the graphite oxide into small molecules, such as $H_2O$ and $CO_2$. These small molecules will escape into air and leave the GNS separated from each other without agglomerating. [146].

## 4.4 Characterization of graphene nano sheets

Similar to CNTs, AFM, Raman, XRD and microscopy are commonly used to characterize GNS

**Atomic force microscopy**

By tapping mode, atomic force microscopy can be used to determine the thickness of GNS, which can be also converted into the number of layers[147]. The edge size of GNS can be obtained in the method. However, GNS' unique 2-D structure will cause some $H_2O$ molecule absorption on the surface, which results in an approximately 1nm experimental thickness of "single layer" [19]. Thus, in ultrathin samples, it is hard to tell if it is single or double layered.

**Raman spectroscopy**

Compared to AFM's limited ability to recognize the difference between single and double layered GNS, Raman spectroscopy is considered to be the most efficiency

method to determine single layered GNS[138, 148]. For both graphite and GNS, their feature Raman spectra show a signature G band at 1584cm$^{-1}$ and G' band and 2700cm$^{-1}$. G band is caused by $E_{2g}$ vibration mode while G' band is caused by the double resonance process. In GNS, the positions of both G and G' band are determined by number of GNS' layers. In single layered GNS, the peak's position is shifted by 5cm$^{-1}$ to the right with constant intensity. Generally, G' band is defined as the "2-D" band, because its intensity and position will both vary due to the changes of number of layers in GNS. In graphite, this 2-D band consists of two peaks: 2-$D_1$ and 2-$D_2$, their intensities are about 1/4 and 1/2 of G band, respectively. In single layered GNS, there is always a sharp peak at lower position, and the intensity is 3 times higher than that of G band. This is used as a signature to differentiate single layered of GNS and multiple layered of GNS. However, when the number of layers is more than 5, then it is hard to distinguish from graphite[149].

**Optical Microscopy**

In Geim and Novoselov's study[19], optical microscopy was used to characterize mechanically exfoliated GNS on a $SiO_2$/silicon substrate. Optical microscopy can provide detailed information on size, shape, color and color contrast determined by the number of graphene layers. The preparation of $SiO_2$ coated substrate is essential to the interference and diffraction of light that result in detectable color contrast in GNS[150, 151].

**X-ray diffraction (XRD)**

Unlike the study of CNTs, XRD is a useful tool to tell the structure of graphite, GNS and graphite-oxide. XRD is useful to determine the extent of oxidation in graphite oxide in top-down methods. It can also determine the structure of the reduced GNS. In the study of ordinary graphite, the signature peak is (002), with a $2\theta$ angle at 26.44 °. In graphite oxide, this peak disappears indicating reduced ordering in graphite and a new peak at 10.6 ° appears, which is the signature peak of graphene oxide at (001). In GNS, the peak at 10.6 ° disappears while a wide peak at 26.44 ° comes back with a much lower intensity compared to that of graphite. This result indicates the decreased crystallinity and increased disordering in graphene[152].

## 4.5 Applications of graphene nano sheets

### 4.5.1 Energy storage

**Lithium battery**

Li-ion secondary battery[153] has found wide applications in modern society and is being actively researched for better performance. However, current anode material was graphite, which suffers from several drawbacks[154], including low theoretical capacity, volume change during charge and discharge process, poor cycle life due to graphite's 3-D structures. Graphene has been proposed as an an alternative anode material because of its superior electrical conductivity, high surface area and chemical tolerance. Many reports demonstrated graphene/metal oxide anodes with the enhanced performance including high capacity, better cycle life and excellent performance under high charge and discharge rate.

**Super capacitors**

Super capacitors are also called electrochemical capacitors. It is a novel device for energy storage, which is based on high efficient electrode materials, such as high specific area carbon material, metal oxide and conducting polymer, etc[155, 156]. Super capacitors still hold several advantages: fast charging rate, long cycling life, high power density and excellent performance under high temperature. The most attractive property of super capacitors is the ability to generate high instant current, which is very desirable in applications like electric vehicles, flash lights and lifting apparatus[157].

Compared to traditional carbon electrode materials, GNS offers many advantages as the electrode material in super capacitors. For example, their high specific area can enhance the energy density. Their unique planar structure will be helpful not only for saturating electrode with electrolyte[158], but also for enhancing absorption/desorption process. GNS's exceptional electric and thermal conductivity are expected to effectively reduce the internal resistance, and improve the heat dispersion within the device[159]. Those attractive properties of GNS make it an interesting candidate electrode material for super capacitors.

### 4.5.2 Field Effect Transistors (FET)

FET is another potential application of GNS. Field effect of GNS[19] was first reported immediately after the discovery of GNS. In this study, graphene based FETs demonstrated a bipolar characteristic at an electron/hole concentration of 1013sq$^{-cm}$, with mobility at almost10000 sq$^{-cm}$/V$^{-s}$ under room temperature It is worth noting that, graphene as a zero band gap material requires tailoring of its dimension and physical properties first[109].

### 4.5.3 Gas and Bio Sensors

The conductivity change in GNS depends on the change in carrier concentration due to the absorption of gas molecules that can act as electron donors or acceptors. Some unique properties of graphene aid to increase its sensitivity to single atom or molecular level detection[160, 161]:. For example, as a 2-D planer material, all carbon atoms are exposed to analyte which contributes to maximizing the adsorption of analyte. Also the high conductivity in GNS contributes to improved sensitivity. According to recent reports, graphene-based sensors not only show good performance in detecting gas, like $NO_2$, $NH_3$, $H_2O$ and CO[162], but also in detecting organics, such as DNA[163], etc.

## References


1.http://www.ece.nus.edu.sg/stfpage/elewuyh/wuyihong_files/Picture_1_files/Carbon_family.jpg

2. Vavilov, V. S. *Physics-Uspekhi* **1998,** 41, (10), 1045.

3. Chung, D. *Acta Crystallographica Section A* **1983,** 39, (1), 192.

4. U.S. Market for Structural Carbon Materials to Grow to $2.8 Billion in 2016. In 2011.

5. Bacon, R. *Journal of Applied Physics* **1960,** 31, (2), 283-290.

6. Michael J. O'Connell, E., Franklin, . **2006**, 360.

7. Kroto, H. W.; Heath, J. R.; O'Brien, S. C.; Curl, R. F.; Smalley, R. E. *Nature* **1985,** 318, (6042), 162-163.

8. Geim, A. K.; Novoselov, K. S. *Nat Mater* **2007,** 6, (3), 183-191.

9. Guldi, D. M.; Martin, N., *Fullerenes: from synthesis to optoelectronic properties*. Springer: 2002; Vol. 4.

10. Sivaraman, N.; Dhamodaran, R.; Kaliappan, I.; Srinivasan, T.; Rao, P. V.;

Mathews, C. *The Journal of Organic Chemistry* **1992,** 57, (22), 6077-6079.

11. Tutt, L. W.; Host, A. *Physics & Chemistry of Fullerenes: A Reprint Collection* **1993,** 1, 234.

12. Schon, J.; Kloc, C.; Siegrist, T.; Steigerwaid, M.; Svensson, C.; Batlogg, B. *Nature* **2001,** 413, (6858), 831-833.

13. Nagashima, H.; Kato, Y.; Yamaguchi, H.; Kimura, E.; Kawanishi, T.; Kato, M.; Saito, Y.; Haga, M.; Itoh, K. *Chemistry Letters* **1994,** 23, (7), 1207-1210.

14. Iijima, S. *Nature* **1991,** 354, (6348), 56-58.

15. De Volder, M. F.; Tawfick, S. H.; Baughman, R. H.; Hart, A. J. *Science* **2013,** 339, (6119), 535-539.

16. Fradkin, E. *Physical Review B* **1986,** 33, (5), 3257.

17. Wallace, P. *Physical Review* **1947,** 71, (9), 622.

18. Slonczewski, J.; Weiss, P. *Physical Review* **1958,** 109, (2), 272.

19. Novoselov, K. S.; Geim, A. K.; Morozov, S. V.; Jiang, D.; Zhang, Y.; Dubonos, S. V.; Grigorieva, I. V.; Firsov, A. A. *Science* **2004,** 306, (5696), 666-669.

20. Dai, H. *Accounts of Chemical Research* **2002,** 35, (12), 1035-1044.

21. Milne, W. I.; Teo, K. B. K.; Amaratunga, G. A. J.; Legagneux, P.; Gangloff, L.; Schnell, J. P.; Semet, V.; Thien Binh, V.; Groening, O. *Journal of Materials Chemistry* **2004,** 14, (6), 933-943.

22. Wang, J.; Dai, J.; Yarlagadda, T. *Langmuir* **2004,** 21, (1), 9-12.

23. Wei, J.; Zhu, H.; Wu, D.; Wei, B. *Applied Physics Letters* **2004,** 84, 4869.

24. Iijima, S.; Ichihashi, T. *Nature* **1993,** 363, (6430), 603-605.

25. Odom, T. W.; Huang, J.-L.; Kim, P.; Lieber, C. M. *Nature* **1998,** 391, (6662), 62-64.

26. Vostrowsky, O. *Advanced Materials* **1997,** 9, (1), 81-82.

27. Meyyappan, M., Carbon Nanotubes: Science and Applications. In 2004.

28. Saito, Y.; Hata, K.; Takakura, A.; Yotani, J.; Uemura, S. *Physica B: Condensed Matter* **2002,** 323, (1–4), 30-37.

29. Andrews, R.; Weisenberger, M. C. *Current Opinion in Solid State and Materials Science* **2004,** 8, (1), 31-37.

30. Li, S.; Qin, Y.; Shi, J.; Guo, Z.-X.; Li, Y.; Zhu, D. *Chemistry of Materials* **2004,** 17, (1), 130-135.

31. Wang, J. *Electroanalysis* **2005,** 17, (1), 7-14.

32. Wang, J.; Musameh, M. *Analytical Chemistry* **2003,** 75, (9), 2075-2079.

33. So, H.-M.; Won, K.; Kim, Y. H.; Kim, B.-K.; Ryu, B. H.; Na, P. S.; Kim, H.; Lee, J.-O. *Journal of the American Chemical Society* **2005,** 127, (34), 11906-11907.

34. Yeow, J. T. W., Carbon Nanotube Gas Sensors. In *Carbon Nanotube Devices*, Wiley-VCH Verlag GmbH & Co. KGaA: 2008; pp 311-349.

35. Zhao, J.; Buldum, A.; Han, J.; Ping Lu, J. *Physical Review Letters* **2000,** 85, (8), 1706-1709.

36. Lu, J. P. *Physical Review Letters* **1997,** 79, (7), 1297-1300.

37. Garg, A.; Han, J.; Sinnott, S. B. *Physical Review Letters* **1998,** 81, (11), 2260-2263.

38. Saito, R.; Takeya, T.; Kimura, T.; Dresselhaus, G.; Dresselhaus, M. S. *Physical Review B* **1999,** 59, (3), 2388-2392.

39. Han, J. L. a. J. *Int. J. High Speed Elec. and Syst.* **1998,** 9, 14.

40. Yu, M.-F.; Lourie, O.; Dyer, M. J.; Moloni, K.; Kelly, T. F.; Ruoff, R. S. *Science* **2000,** 287, (5453), 637-640.

41. Demczyk, B. G.; Wang, Y. M.; Cumings, J.; Hetman, M.; Han, W.; Zettl, A.; Ritchie, R. O. *Materials Science and Engineering: A* **2002,** 334, (1–2), 173-178.

42. Stainless Steel Properties. In Australian Stainless Steel Development Association.

43. Guo, S.; Dong, S. *Chem. Soc. Rev.* **2011,** 40, (5), 2644-2672.

44. Meyyappan, M., *Carbon nanotubes: science and applications*. CRC: 2004.

45. Tang, C.; Guo, W.; Chen, C. *Physical Review B* **2009,** 79, (15), 155436.

46. Jiang, L.; Gao, L. *Carbon* **2003,** 41, (15), 2923-2929.

47. Lebedkin, S.; Arnold, K.; Hennrich, F.; Krupke, R.; Renker, B.; Kappes, M. M. *New Journal of Physics* **2003,** 5, 140.

48. O'connell, M. J.; Bachilo, S. M.; Huffman, C. B.; Moore, V. C.; Strano, M. S.; Haroz, E. H.; Rialon, K. L.; Boul, P. J.; Noon, W. H.; Kittrell, C. *Science* **2002,** 297, (5581), 593-596.

49. Saito, R.; Dresselhaus, G.; Dresselhaus, M. S., *Physical properties of carbon nanotubes*. World Scientific: 1998; Vol. 35.

50. Dresselhaus, M. S.; Dresselhaus, G.; Saito, R.; Jorio, A. *Physics Reports* **2005,** 409, (2), 47-99.

51. Rao, A.; Richter, E.; Bandow, S.; Chase, B.; Eklund, P.; Williams, K.; Fang, S.; Subbaswamy, K.; Menon, M.; Thess, A. *Science* **1997,** 275, (5297), 187-191.

52. Freitag, M.; Martin, Y.; Misewich, J.; Martel, R.; Avouris, P. *Nano Letters* **2003,** 3, (8), 1067-1071.

53. Ajayan, P. *ChemInform* **1999,** 30, (39), no-no.

54. Saito, R.; Fujita, M.; Dresselhaus, G.; Dresselhaus, M. S. *Physical Review B* **1992,** 46, (3), 1804.

55. Mintmire, J. W.; Dunlap, B. I.; White, C. T. *Physical Review Letters* **1992,** 68, (5), 631-634.

56. Bockrath, M.; Cobden, D. H.; McEuen, P. L.; Chopra, N. G.; Zettl, A.; Thess, A.; Smalley, R. *Science* **1997,** 275, (5308), 1922-1925.

57. Frank, S.; Poncharal, P.; Wang, Z.; de Heer, W. A. *Science* **1998,** 280, (5370), 1744-1746.

58. Odom, T. W.; Huang, J. L.; Kim, P.; Lieber, C. M. *Nature* **1998,** 391, (6662), 62-64.

59. Wildoer, J. W. G.; Venema, L. C.; Rinzler, A. G.; Smalley, R. E.; Dekker, C. *Nature* **1998,** 391, (6662), 59-62.

60. Huang, Y.; Okada, M.; Tanaka, K.; Yamabe, T. *Physical Review, B: Condensed Matter* **1996,** 53, (9).

61. http://www.nanocyl.com/CNT-Expertise-Centre/Carbon-Nanotubes

62. Han, J.; Anantram, M.; Jaffe, R.; Kong, J.; Dai, H. *Physical Review B* **1998,** 57, (23), 14983.

63. Cassell, A. M.; Raymakers, J. A.; Kong, J.; Dai, H. *The Journal of Physical Chemistry B* **1999,** 103, (31), 6484-6492.

64. Couteau, E.; Hernadi, K.; Seo, J. W.; Thien-Nga, L.; Mikó, C.; Gaal, R.; Forro, L. *Chemical Physics Letters* **2003,** 378, (1), 9-17.

65. Colbert, D. T.; Smalley, R. E. *Carbon* **1995,** 33, (7), 921-924.

66. Journet, C.; Maser, W.; Bernier, P.; Loiseau, A.; Lamy de La Chapelle, M.; Lefrant, S.; Deniard, P.; Lee, R.; Fischer, J. *Nature* **1997,** 388, (6644), 756-757.

67. Maser, W.; Lambert, J.; Ajayan, P.; Stephan, O.; Bernier, P. *Synthetic metals* **1996,** 77, (1), 243-247.

68. Guo, T.; Nikolaev, P.; Thess, A.; Colbert, D.; Smalley, R. *Chemical Physics Letters* **1995,** 243, (1), 49-54.

69. Saito, Y.; Yoshikawa, T.; Inagaki, M.; Tomita, M.; Hayashi, T. *Chemical Physics Letters* **1993,** 204, (3-4), 277-282.

70. Kiselev, N.; Moravsky, A.; Ormont, A.; Zakharov, D. *Carbon* **1999,** 37, (7), 1093-1103.

71. Colbert, D.; Zhang, J.; McClure, S.; Nikolaev, P.; Chen, Z.; Hafner, J.; Owens, D.; Kotula, P.; Carter, C.; Weaver, J. *ChemInform* **1995,** 26, (9), no-no.

72. Thess, A.; Lee, R.; Nikolaev, P.; Dai, H.; Petit, P.; Robert, J.; Xu, C.; Lee, Y. H.; Kim, S. G.; Rinzler, A. G. *Science* **1996,** 273, (5274), 483-487.

73. Kataura, H.; Kimura, A.; Ohtsuka, Y.; Maniwa, S.; Hanyu, T.; Achiba, Y. *Japanese journal of applied physics* **1998,** 37, L616-L618.

74. Endo, M.; Takeuchi, K.; Igarashi, S.; Kobori, K.; Shiraishi, M.; Kroto, H. W. *Journal of Physics and Chemistry of Solids* **1993,** 54, (12), 1841-1848.

75. Kumar, M.; Ando, Y. *Journal of Nanoscience and Nanotechnology* **2010,** 10, (6), 3739-3758.

76. Kukovitsky, E.; L'vov, S.; Sainov, N.; Shustov, V.; Chernozatonskii, L. *Chemical Physics Letters* **2002,** 355, (5), 497-503.

77. Jose‐Yacaman, M.; Miki‐Yoshida, M.; Rendon, L.; Santiesteban, J. *Applied Physics Letters* **1993,** 62, (2), 202-204.

78. Chen, P.; Zhang, H. B.; Lin, G. D.; Hong, Q.; Tsai, K. *Carbon* **1997,** 35, (10-11), 1495-1501.

79. Ivanov, V.; Nagy, J.; Lambin, P.; Lucas, A.; Zhang, X.; Zhang, X.; Bernaerts, D.; Van Tendeloo, G.; Amelinckx, S.; Van Landuyt, J. *Chemical Physics Letters* **1994,** 223, (4), 329-335.

80. Hernadi, K.; Fonseca, A.; Nagy, J. B.; Siska, A.; Kiricsi, I. *Applied Catalysis A: General* **2000,** 199, (2), 245-255.

81. Ren, Z.; Huang, Z.; Xu, J.; Wang, J.; Bush, P.; Siegal, M.; Provencio, P. *Science* **1998,** 282, (5391), 1105-1107.

82. Zhu, H.; Xu, C.; Wu, D.; Wei, B.; Vajtai, R.; Ajayan, P. M. *Science* **2002,** 296, (5569), 884-886.

83. Rafique, M. M. A.; Iqbal, J. *Journal of Encapsulation and Adsorption Sciences* **2011,** 1, (2), 29-34.

84. Chiang, I.; Brinson, B.; Huang, A.; Willis, P.; Bronikowski, M.; Margrave, J.; Smalley, R.; Hauge, R. *The Journal of Physical Chemistry B* **2001,** 105, (35), 8297-8301.

85. Dujardin, E.; Ebbesen, T. W.; Krishnan, A.; Treacy, M. M. J. *Advanced Materials* **1999,** 10, (8), 611-613.

86. Liu, J.; Rinzler, A. G.; Dai, H.; Hafner, J. H.; Bradley, R. K.; Boul, P. J.; Lu, A.; Iverson, T.; Shelimov, K.; Huffman, C. B. *Science* **1998,** 280, (5367), 1253-1256.

87. Dillon, A. C.; Gennett, T.; Jones, K. M.; Alleman, J. L.; Parilla, P. A.; Heben, M. J. *Advanced Materials* **1999,** 11, (16), 1354-1358.

88. Rinzler, A.; Liu, J.; Dai, H.; Nikolaev, P.; Huffman, C.; Rodriguez-Macias, F.; Boul, P.; Lu, A. H.; Heymann, D.; Colbert, D. *Applied Physics A: Materials Science & Processing* **1998,** 67, (1), 29-37.

89. Bandow, S.; Asaka, S.; Zhao, X.; Ando, Y. *Applied Physics A: Materials Science & Processing* **1998,** 67, (1), 23-27.

90. Zimmerman, J. L.; Bradley, R. K.; Huffman, C. B.; Hauge, R. H.; Margrave, J. L. *Chemistry of Materials* **2000,** 12, (5), 1361-1366.

91. Bandow, S.; Rao, A.; Williams, K.; Thess, A.; Smalley, R.; Eklund, P. *The Journal of Physical Chemistry B* **1997,** 101, (44), 8839-8842.

92. Andrews, R.; Jacques, D.; Rao, A.; Derbyshire, F.; Qian, D.; Fan, X.; Dickey, E.; Chen, J. *Chemical Physics Letters* **1999,** 303, (5), 467-474.

93. Gardiner, D. J.; Graves, P. R.; Bowley, H. J., *Practical Raman Spectroscopy*. Springer-Verlag Berlin: 1989; Vol. 21.

94. Dresselhaus, M. S.; Dresselhaus, G.; Eklund, P., *Science of fullerenes and carbon nanotubes*. Academic Pr: 1996.

95. Kong, J.; Soh, H. T.; Cassell, A. M.; Quate, C. F.; Dai, H. *Nature* **1998,** 395, (6705), 878-881.

96. Chen, J.; Rao, A. M.; Lyuksyutov, S.; Itkis, M. E.; Mark. A. Hamon, ⊥; Hu, H.; Cohn, R. W.; Eklund, P. C.; Colbert, D. T.; Smalley, R. E. *The Journal of Physical Chemistry B* **2001,** 105, (13), 2525-2528.

97. Chen, L.; Cheung, C. L.; Ashby, P. D.; Lieber, C. M. *Nano Letters* **2004,** 4, (9), 1725-1731.

98. Woolley, A. T.; Cheung, C. L.; Hafner, J. H.; Lieber, C. M. *Chemistry & Biology* **2000,** 7, (11), R193-R204.

99. Ouyang, M.; Huang, J. L.; Lieber, C. M. *Accounts of Chemical Research* **2002,** 35, (12), 1018-1025.

100. Kim, P.; Odom, T. W.; Huang, J.; Lieber, C. M. *Carbon* **2000,** 38, (11-12), 1741-1744.

101. Osváth, Z.; Vértesy, G.; Tapasztó, L.; Wéber, F.; Horváth, Z.; Gyulai, J.; Biró, L. *Physical Review B* **2005,** 72, (4), 045429.

102. Kim, H.; Lee, J.; Kahng, S. J.; Son, Y. W.; Lee, S.; Lee, C. K.; Ihm, J.; Kuk, Y. *Physical Review Letters* **2003,** 90, (21), 216107.

103. Bellucci, S. *physica status solidi (c)* **2005,** 2, (1), 34-47.

104. Chernozatonskii, L.; Gulyaev, Y. V.; Kosakovskaja, Z. J.; Sinitsyn, N.; Torgashov, G.; Zakharchenko, Y. F.; Fedorov, E.; Val'Chuk, V. *Chemical Physics Letters* **1995,** 233, (1-2), 63-68.

105. Adessi, C.; Devel, M. *Physical Review B* **2000,** 62, (20), 13314-13317.

106. Choi, W.; Jin, Y.; Kim, H.; Lee, S.; Yun, M.; Kang, J.; Choi, Y.; Park, N.; Lee, N.; Kim, J. *Applied Physics Letters* **2001,** 78, (11), 1547-1549.

107. Qian, D.; Dickey, E. C.; Andrews, R.; Rantell, T. *Applied Physics Letters* **2000,** 76, 2868.

108. Biercuk, M.; Llaguno, M. C.; Radosavljevic, M.; Hyun, J.; Johnson, A. T.; Fischer, J. E. *Applied Physics Letters* **2002,** 80, 2767.

109. Jiao, L.; Zhang, L.; Wang, X.; Diankov, G.; Dai, H. *Nature* **2009,** 458, (7240), 877-880.

110. Balandin, A. A.; Ghosh, S.; Bao, W.; Calizo, I.; Teweldebrhan, D.; Miao, F.; Lau, C. N. *Nano Letters* **2008,** 8, (3), 902-907.

111. Lee, C.; Wei, X.; Kysar, J. W.; Hone, J. *Science* **2008,** 321, (5887), 385-388.

112. Park, S.; Ruoff, R. S. *Nature nanotechnology* **2009,** 4, (4), 217-224.

113. Stankovich, S.; Dikin, D. A.; Piner, R. D.; Kohlhaas, K. A.; Kleinhammes, A.; Jia, Y.; Wu, Y.; Nguyen, S. B. T.; Ruoff, R. S. *Carbon* **2007,** 45, (7), 1558-1565.

114. Meyer, J. C.; Geim, A.; Katsnelson, M.; Novoselov, K.; Booth, T.; Roth, S. *Nature* **2007,** 446, (7131), 60-63.

115. Stolyarova, E.; Rim, K. T.; Ryu, S.; Maultzsch, J.; Kim, P.; Brus, L. E.; Heinz, T. F.; Hybertsen, M. S.; Flynn, G. W. *Proceedings of the National Academy of Sciences* **2007,** 104, (22), 9209.

116. Rao, C. N. R.; Biswas, K.; Subrahmanyam, K. S.; Govindaraj, A. *Journal of Materials Chemistry* **2009,** 19, (17), 2457.

117. Mermin, N. D. *Physical Review* **1968,** 176, (1), 250.

118. Calado, V.; Schneider, G.; Theulings, A.; Dekker, C.; Vandersypen, L. *Applied Physics Letters* **2012,** 101, (10), 103116-103116-3.

119. Geim, A. K. *Science* **2009,** 324, (5934), 1530-1534.

120. http://www.mechanicalengineeringblog.com/tag/graphene-vs-steel/

121. Nair, R.; Blake, P.; Grigorenko, A.; Novoselov, K.; Booth, T.; Stauber, T.; Peres, N.; Geim, A. *Science* **2008,** 320, (5881), 1308-1308.

122. Ni, Z.; Wang, H.; Kasim, J.; Fan, H.; Yu, T.; Wu, Y.; Feng, Y.; Shen, Z. *Nano Letters* **2007,** 7, (9), 2758-2763.

123. Zhang, H.; Tang, D.; Zhao, L.; Bao, Q.; Loh, K. *Optics Express* **2009,** 17, (20), 17630-17635.

124. Sun, Z.; Hasan, T.; Torrisi, F.; Popa, D.; Privitera, G.; Wang, F.; Bonaccorso, F.; Basko, D. M.; Ferrari, A. C. *ACS Nano* **2010,** 4, (2), 803-810.

125. Bolotin, K. I.; Sikes, K.; Jiang, Z.; Klima, M.; Fudenberg, G.; Hone, J.; Kim, P.; Stormer, H. *Solid State Communications* **2008,** 146, (9), 351-355.

126. Kim, K. S.; Zhao, Y.; Jang, H.; Lee, S. Y.; Kim, J. M.; Ahn, J. H.; Kim, P.; Choi, J. Y.; Hong, B. H. *Nature* **2009,** 457, (7230), 706-710.

127. Son, Y. W.; Cohen, M. L.; Louie, S. G. *Nature* **2006,** 444, (7117), 347-349.

128. Heersche, H. B.; Jarillo-Herrero, P.; Oostinga, J. B.; Vandersypen, L. M. K.; Morpurgo, A. F. *Nature* **2007,** 446, (7131), 56-59.

129. Somani, P. R.; Somani, S. P.; Umeno, M. *Chemical Physics Letters* **2006,** 430, (1), 56-59.

130. Reina, A.; Jia, X.; Ho, J.; Nezich, D.; Son, H.; Bulovic, V.; Dresselhaus, M. S.; Kong, J. *Nano Letters* **2008,** 9, (1), 30-35.

131. John, R.; Ashokreddy, A.; Vijayan, C.; Pradeep, T. *Nanotechnology* **2011,** 22, 165701.

132. Dervishi, E.; Li, Z.; Watanabe, F.; Biswas, A.; Xu, Y.; Biris, A. R.; Saini, V.; Biris, A. S. *Chemical Communications* **2009**, (27), 4061-4063.

133. Choi, W.; Lee, J. W., *Graphene: Synthesis and Applications*. CRC Press: 2011; Vol. 3.

134. Li, X.; Cai, W.; Colombo, L.; Ruoff, R. S. *Nano Letters* **2009,** 9, (12), 4268-4272.

135. Wu, Z. S.; Ren, W.; Gao, L.; Zhao, J.; Chen, Z.; Liu, B.; Tang, D.; Yu, B.; Jiang, C.; Cheng, H. M. *ACS Nano* **2009,** 3, (2), 411-417.

136. Subrahmanyam, K.; Panchakarla, L.; Govindaraj, A.; Rao, C. *The Journal of Physical Chemistry C* **2009,** 113, (11), 4257-4259.

137. Eizenberg, M.; Blakely, J. *Surface Science* **1979,** 82, (1), 228-236.

138. Röhrl, J.; Hundhausen, M.; Emtsev, K.; Seyller, T.; Graupner, R.; Ley, L. *Applied Physics Letters* **2008,** 92, 201918.

139. Zhu, M.; Wang, J.; Outlaw, R. A.; Hou, K.; Manos, D. M.; Holloway, B. C. *Diamond and related materials* **2007,** 16, (2), 196-201.

140. Berger, C.; Song, Z.; Li, X.; Wu, X.; Brown, N.; Naud, C.; Mayou, D.; Li, T.; Hass, J.; Marchenkov, A. N. *Science* **2006,** 312, (5777), 1191-1196.

141. Hummers, W. S.; Offeman, R. E. *Journal of the American Chemical Society* **1958,** 80, (6), 1339-1339.

142. Park, S.; An, J.; Jung, I.; Piner, R. D.; An, S. J.; Li, X.; Velamakanni, A.; Ruoff, R. S. *Nano Letters* **2009,** 9, (4), 1593-1597.

143. Zhu, Y.; Stoller, M. D.; Cai, W.; Velamakanni, A.; Piner, R. D.; Chen, D.;

Ruoff, R. S. *ACS Nano* **2010,** 4, (2), 1227-1233.

144. Liang, Y.; Wu, D.; Feng, X.; Müllen, K. *Advanced Materials* **2009,** 21, (17), 1679-1683.

145. Fan, X.; Peng, W.; Li, Y.; Li, X.; Wang, S.; Zhang, G.; Zhang, F. *Advanced Materials* **2008,** 20, (23), 4490-4493.

146. Jung, I.; Vaupel, M.; Pelton, M.; Piner, R.; Dikin, D. A.; Stankovich, S.; An, J.; Ruoff, R. S. *The Journal of Physical Chemistry C* **2008,** 112, (23), 8499-8506.

147. Ishigami, M.; Chen, J.; Cullen, W.; Fuhrer, M.; Williams, E. *Nano Letters* **2007,** 7, (6), 1643-1648.

148. Ferrari, A. C.; Meyer, J. C.; Scardaci, V.; Casiraghi, C.; Lazzeri, M.; Mauri, F.; Piscanec, S.; Jiang, D.; Novoselov, K. S.; Roth, S.; Geim, A. K. *Physical Review Letters* **2006,** 97, (18).

149. Cançado, L.; Pimenta, M.; Neves, B.; Medeiros-Ribeiro, G.; Enoki, T.; Kobayashi, Y.; Takai, K.; Fukui, K.; Dresselhaus, M.; Saito, R. *Physical Review Letters* **2004,** 93, (4), 47403.

150. Blake, P.; Hill, E.; Neto, A. H. C.; Novoselov, K.; Jiang, D.; Yang, R.; Booth, T.; Geim, A. *Applied Physics Letters* **2007,** 91, 063124.

151. Roddaro, S.; Pingue, P.; Piazza, V.; Pellegrini, V.; Beltram, F. *Nano Letters* **2007,** 7, (9), 2707-2710.

152. Wang, G.; Yang, J.; Park, J.; Gou, X.; Wang, B.; Liu, H.; Yao, J. *The Journal of Physical Chemistry C* **2008,** 112, (22), 8192-8195.

153. Liu, R.; Duay, J.; Lee, S. B. *Chem. Commun.* **2011,** 47, (5), 1384-1404.

154. Liang, M.; Zhi, L. *J. Mater. Chem.* **2009,** 19, (33), 5871-5878.

155. Winter, M.; Brodd, R. J. *ChemInform* **2004,** 35, (50), no-no.

156. Miller, J. R.; Simon, P. *Science Magazine* **2008,** 321, (5889), 651-652.

157. Burke, A. *Journal of power sources* **2000,** 91, (1), 37-50.

158. Wu, Q.; Xu, Y.; Yao, Z.; Liu, A.; Shi, G. *ACS Nano* **2010,** 4, (4), 1963-1970.

159. Fan, Z.; Yan, J.; Zhi, L.; Zhang, Q.; Wei, T.; Feng, J.; Zhang, M.; Qian, W.; Wei, F. *Advanced Materials* **2010,** 22, (33), 3723-3728.

160. Wang, Y.; Li, Y.; Tang, L.; Lu, J.; Li, J. *Electrochemistry Communications* **2009,** 11, (4), 889-892.

161. Alwarappan, S.; Erdem, A.; Liu, C.; Li, C. Z. *The Journal of Physical Chemistry C* **2009,** 113, (20), 8853-8857.

162. Schedin, F.; Geim, A.; Morozov, S.; Hill, E.; Blake, P.; Katsnelson, M.; Novoselov, K. *Nature materials* **2007,** 6, (9), 652-655.

163. Fowler, J. D.; Allen, M. J.; Tung, V. C.; Yang, Y.; Kaner, R. B.; Weiller, B. H. *ACS Nano* **2009,** 3, (2), 301-306.

164. Hirsch, A. *Nature materials* **2010,** 9, (11), 868-871.

# CHAPTER 3: PUBLICATIONS

## Paper 1: Exposure of carbon nanotubes fabricated by template-assisted CVD through a two-step method


## Abstract

Carbon nanotubes/ceramic composites have been studied extensively in recent years. Well aligned carbon nanotubes are highly desirable for various studies and applications. Template-assisted chemical vapor deposition have been developed and applied for a decade. However, post growth surface cleaning to remove the junk carbon on sample surface and expose carbon nanotubes still relies on either capital intensive facilities or 'hard to control' process. In the letter, we report a mechanical polishing method to remove the amorphous carbon layer. Compared to other conventional surface cleaning methods, mechanical polishing is relatively straightforward, much easier to scale up and requires no expensive instruments. Combined with a wet-etching step using sodium hydroxide as the etchant, highly ordered carbon nanotube arrays were reliably obtained. Scanning electron microscopy and atomic force microscopy were employed to investigate the surface morphology and roughness and to optimize the processing conditions.


### 1. Introduction

Since the report of carbon nanotubes (CNTs) by Iijima[1], these materials have demonstrated exceptional mechanical, thermal and electric properties due to their unique structures. Hence, CNTs have been vigorously studied as promising candidates for varies applications, including electron field emitters[2-5], electronic devices[6-10], bio sensors[11-13], and drug delivery vessel[14-17]. For many applications, such as flat panel displays and some sensors, it is essential to have free standing and well aligned CNT arrays with controllable length. In order to provide large area of dense packed and highly ordered CNTs, template assisted method has been well developed[18]. During the last decade, several groups have synthesized well-aligned CNTs by using template assisted method for diverse applications[19-22]. To meet the requirement of fabrication of well aligned and free standing CNT arrays, porous alumina templates is one of the most popular candidate because it can provide uniform, vertical nanopore channels

and hexagonal packed structure[18]. In addition, the most attractive advantage of AAO template is that its thickness and diameter is highly controllable, which is critical to control the dimension (such as length and diameter) of the final product (CNTs), which is favored by many researchers—by varying the several parameters, such as electrolyte, DC voltage and anodization duration, the thickness, pore density and pore diameter are tunable[19]. As a starting material, bulk aluminum sheet has been applied by many groups for the two-step anodization method to serve as a highly controllable platform for the fabrication of aligned CNTs[23-25].

Herein, a template assisted catalytic chemical vapor deposition (CCVD) method was developed to gain uniform and well-aligned CNTs. In this letter, a two-step anodization method is used to provide nanoporous templates with high controllability. The diameter and length of CNTs grown within the pores can be determined by the pore size and the thickness of the template, respectively[19, 26]. Furthermore, this method can be scaled-up for manufacturing and is highly compatible with the existing manufacturing techniques[27] . Thus, this method has been widely employed in both research labs and commercial manufacturing practices[28, 29].

However, an issue has accompanied the template-assisted CCVD method: after the growth of CNTs, there's always a layer of junk carbon on the as-made product[19]. Since for many applications it is essential to remove this layer of junk carbon and controllably expose the highly ordered CNTs, a method to selectively and effectively remove the junk carbon without ruining the CNTs within the nanopores is highly desirable. Up to now, numerous attempts, such as air oxidation and reactive ion etching (RIE)[30-32] were studied for this purpose. However, each of these methods has their own pros and cons: air oxidation is relatively cheap, but it is quite hard to control. It is rather difficult to optimize treating temperature and duration; if the condition is not optimized, it not only removes the junk carbon on the surface, but also damages the CNTs within the nanopores[33, 34]; RIE[35-38] can reliably and selectively remove the junk carbon layer, but this process may take up to 5 hours depending on the layer thickness. Besides, it requires rather expensive equipment and sophisticated maintenance, thus are less available outside of large research universities and laboratories. In this report, a simple, fast and low cost post treatment, which is composed of mechanical polishing and subsequent wet-etching, was demonstrated as an effective method to clean the as-made product surface immediately after CCVD of

CNTs in templates and expose the CNTs. Through the characterization of sample surface by scanning electron microscopy and atomic force microscopy, it was confirmed that by using small polishing particles a smooth surface with complete removal of junk carbon layer can be obtained through 1 minute of mechanical polishing. Controlled wet etching can be used to further expose the CNTs to desired height.

## 2. Experimental

The CNTs were synthesized by a well-established template assisted CVD method[38], which consists of three steps(as illuminated in Figure 1.): 1. Anodize aluminum sheets to gain nanoporous templates; 2. Grow CNTs via CCVD method; and 3. Post treat the as-made sample to expose the CNTs.

First of all, an aluminum sheet (purity 99.999%) was anodized via a typical two-step method to generate highly ordered nanoporous templates[39]. Briefly, a first anodization step was carried out in 0.3M oxalic acid at 40 V DC and 10℃ for at least 16 hours. Then a mixture of chromic acid and phosphoric acid was used to remove the AAO thin film on the sheet, followed by the second anodization step conducted under the same conditions for about 12 hours to form highly ordered arrays of hexagonal pores.

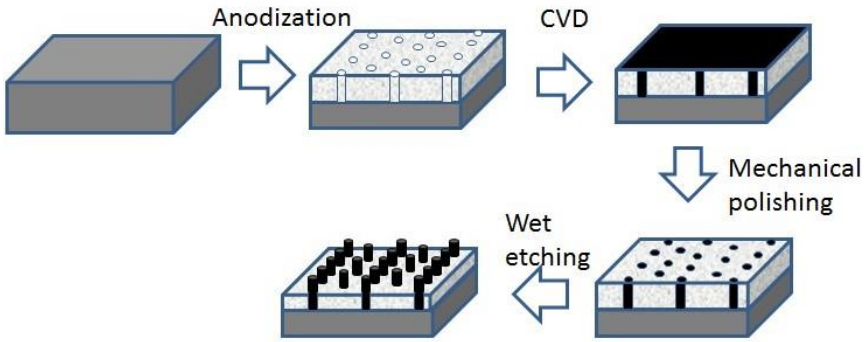


**Figure 1:** Schematic process of sample preparation

To grow CNTs inside the nanopores, a CCVD method was applied after the template preparation[39]. Cobalt is used as catalyst for CNT growth. The cobalt nanoparticles were electrochemically deposited to the bottom of the nanopores[39]. To reduce the catalyst, the template with cobalt particles was placed in a tube furnace,

heated up to 600℃ under CO flow (80ml/s) for 2 hours. Then CO was replaced by a mixture of $C_2H_2$ (20ml/s) and $N_2$ (60ml/s) for CNTs growth, the reaction lasted for 2 hours. Finally, the sample was annealed in a nitrogen atmosphere at 600℃ for another 12 hours.

The amorphous carbon layer was removed by mechanical polishing. Different particles (Gamma alumina, from Bucheler Inc.) were used to polish the sample surface by E- plus AC Adjustable Speed control polishing machine from FHP Inc. for 1minute. As a comparison, two other conventional surface cleaning methods, ion milling and air oxidation were also employed to treat identical samples. For a typical ion milling process, the sample was cleaned at $BCl_3$ 20 sccm, Ar 5 sccm, Pressure 15 mTorr, Power: 100 W by a RIE system of Trion Minilock II for 15 minutes [39]. For a typical air oxidation, the sample was calcined in the air at 650℃ for 30min[40].

After surface cleaning, the samples were wet etched by 0.01M NaOH solution for 20minutes.

The morphologies of samples were investigated with scanning electron microscopy (JOEL 7000F) operated at 15kV; and the surface roughness was studied by atomic force microscopy (AFM, MFP3D Bio, Asylum Research) operating in contact mode.

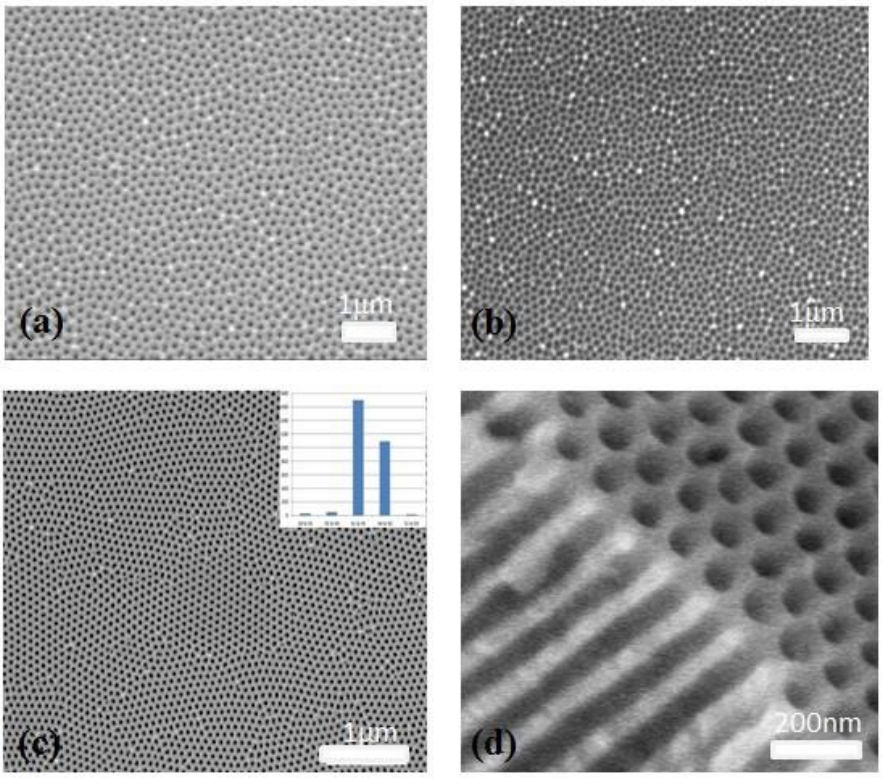


**Figure 2:** Top view of the template after (a) the 1st anodization; (b) Top view after removing the AAO layer; c) Top view of the template after the 2nd anodization; (d) cross- section of AAO template[41]

## 3. Results and discussion

Fig. 2a and b show tightly aligned nanopores formed within the AAO film after the first anodization. After the second anodization, hexagonal nanopores were found to be embedded in the template (Fig. 2c). To extract the diameter distribution of the pores, the SEM images were analyzed with an open source software "Image J"[42]. The result shows the size distribution is quite uniform, the mean diameter is 40.06nm (Figure 2c). In addition, straight channels were obtained (Fig. 2d), obviously the channels are vertical to the film surface, which meets the essential requirement to fabricate homogenous dispersed CNTs.

After the CCVD synthesis, as shown in Fig. 3a, a thick amorphous carbon layer was observed on the sample surface, similarly to previous reports and typical for the template-assisted CCVD process[33], which is inert to most etchants and will jeopardize the subsequent wet etching step. From Fig. 3b, it is obvious that after air oxidation, some of the junk carbon was removed. However, there is still a layer of carbon that blocks the well aligned and ordered CNTs. This result supports the view that the air oxidation method is hard to control.

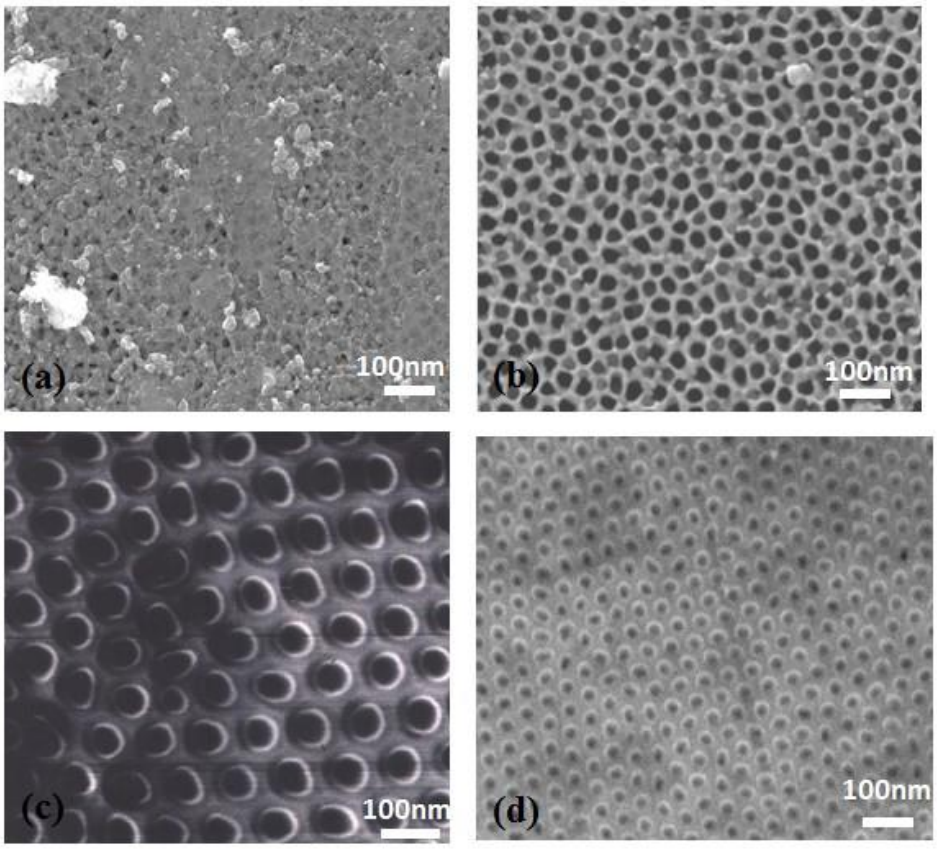


**Figure 3:** Top view SEM image of the sample after: (a) CNTs growth; (b) air oxidation; (c)RIE cleaning; (d) mechanical polishing;

The sample was also treated by a reported RIE method. Top view of the sample (Figure 3(c)) shows that after RIE, the sample surface is flat and the amorphous carbon has been removed. So apparently the RIE method is much more controllable than the air oxidation method. However, the RIE procedure took up a long time (5 hours according to this experiment), and the equipment is not common on many campuses. Therefore, an alternative method is still desired.

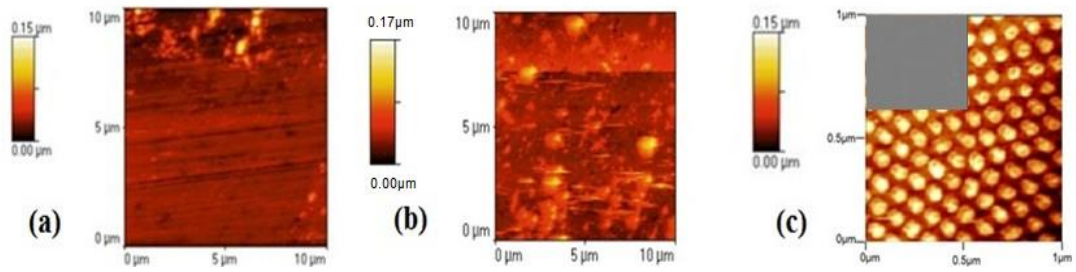


**Figure 4:** AFM topograhies after polished by particles of (a) 1 µm (b)300nm (c) 50nm in diameter.

The high rigidity of the sample promises the possibility to employ a simple mechanical polishing method to clean the as-made sample surface. Mechanical polishing eliminates the risk of damaging the CNTs. For all mechanical polishing procedures, the duration was 1 minute, and the rotate speed was fixed at 144 rpm, different sizes of polishing particles were used for comparison in this process. Here polishing particles with 3 different sizes (1 µm, 300nm, 50nm, respectively) were applied. Each sample after polishing was scanned by AFM to inspect the topography (Figure. 4 a-c). All the as-made samples were scanned at an area of 10×10 µm, but as shown in the inset of Figure 4(c), it was hard to tell the details of the sample surface at such a huge scan area, therefore, for the sample polished by 50nm particles, topography with small scan area (1×1 µm) was acquired (Figure 4(c)).

**Table 1:** Sample roughness after different polishing conditions

| Duration | Rotate speed | Particle size | Roughness(RMS) |
|---|---|---|---|
| 1 min | 144rpm | 50nm | 2.1nm |
| 1min | 144rpm | 300nm | 3.4nm |
| 1min | 144rpm | 1 µm | 16.4nm |

Figure 3c is the SEM top view image of a typical sample surface that was polished by 50nm particles for 1 min. It is obvious that the amorphous carbon has completely been removed and CNTs were exposed out of the template matrix after 1min mechanical polishing. Figure 4 a, b, and c are AFM topographies of the sample

after been treated by particles of 1μm, 300nm and 50nm in diameter, respectively. Compared to Figure 4c, it is difficult to see the notable effect of polishing from Figure 4 (a) and (b). In addition, the surface roughness was also collected by AFM at the same scan area(5×5μm) (Table 1), it can be concluded that the smaller polishing particles gave better uniformity, this result means 50nm particles is the optimized polishing condition.

To compare mechanical polishing with the two traditional surface methods above, the sample treated with 50nm particles was further investigated by SEM and AFM. From Figure. 4c, remarkable removal of amorphous carbon was observed and what's more, the CNTs were exposed to a certain extent. The result was comparable to the surface cleaning by RIE (Figure 3c).

Figure 5a is the top view image of the sample after etching the sample with 0.01M NaOH for 20 min, the CNTs were successfully further exposed (Figure 5a) and the matrix remains flat. To measure the exposed length of CNTs accurately, AFM topographic measurements (one typical test shown in Figure 5(b) and (c)) confirmed that the CNTs in the samples treated by this two-step post-growth process were exposed rather uniformly, the height is about 50nm, identified by Figure 5(d).

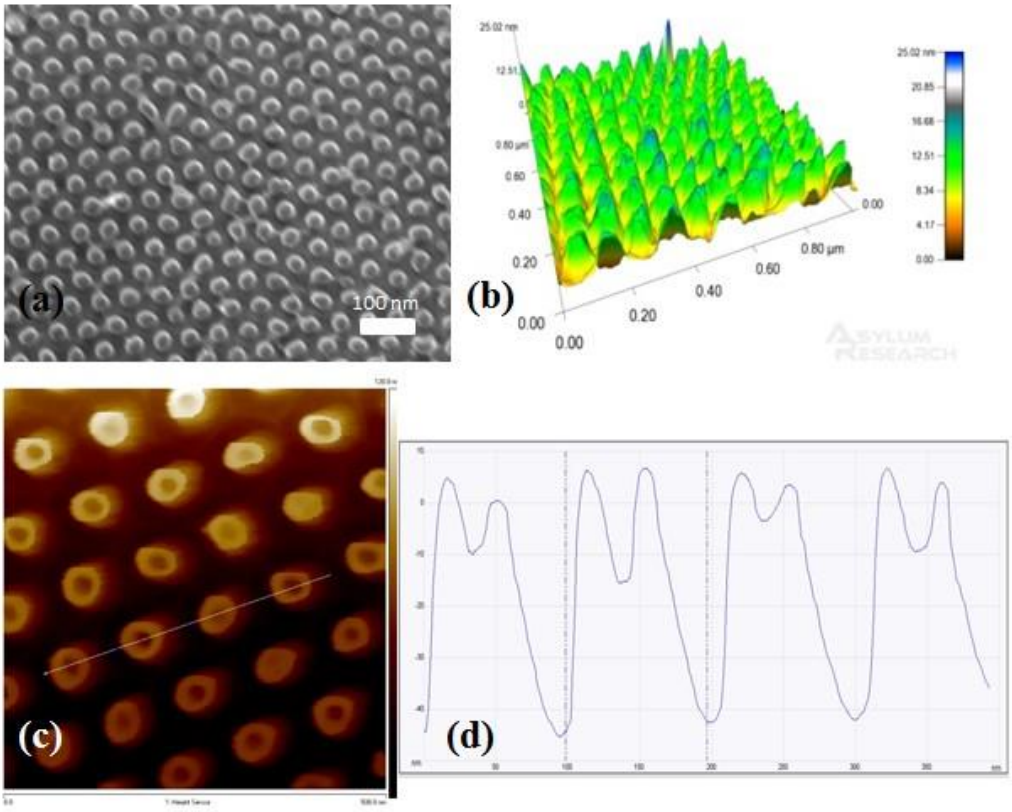


**Figure 5:** (a) SEM top view image; (b) 3-D image of the sample after post- treatment; (c) AFM topography of the sample; (d) cross sectional profile of the sample

## 4. Conclusions

In conclusion, the CCVD process based on Template-assisted method is an convenient way to synthesize highly ordered CNTs in large scale. AAO templates made via two-step anodization method can serve as a platform to provide uniform nanopores for the synthesis of well-aligned carbon nanotubes. Mechanical polishing combined with wet-etching method can be considered as a low cost and effective alternative method to clean the surface and expose CNTs, it is relatively simple, straightforward, controllable, and useful for the future applications, such as interfacial mechanical test, electric applications, etc.

## References


1. Iijima, S. *Nature* **1991,** 354, (6348), 56-58.

2. Zhu, W.; Bower, C.; Zhou, O.; Kochanski, G.; Jin, S. *Applied Physics Letters* **1999,** 75, (6), 873-875.

3. Fan, S.; Chapline, M. G.; Franklin, N. R.; Tombler, T. W.; Cassell, A. M.; Dai, H. *Science* **1999,** 283, (5401), 512-514.

4. Saito, Y.; Uemura, S. *Carbon* **2000,** 38, (2), 169-182.

5. Bonard, J.-M.; Croci, M.; Klinke, C.; Kurt, R.; Noury, O.; Weiss, N. *Carbon* **2002,** 40, (10), 1715-1728.

6. Liu, J.; Casavant, M. J.; Cox, M.; Walters, D.; Boul, P.; Lu, W.; Rimberg, A.; Smith, K.; Colbert, D. T.; Smalley, R. E. *Chemical Physics Letters* **1999,** 303, (1), 125-129.

7. Bachtold, A.; Fuhrer, M.; Plyasunov, S.; Forero, M.; Anderson, E. H.; Zettl, A.; McEuen, P. L. *Physical Review Letters* **2000,** 84, (26), 6082.

8. Wang, J.; Musameh, M.; Lin, Y. *Journal of the American Chemical Society* **2003,** 125, (9), 2408-2409.

9. Kocabas, C.; Shim, M.; Rogers, J. A. *Journal of the American Chemical Society* **2006,** 128, (14), 4540-4541.

10. Fu, L.; Liu, Z.; Liu, Y.; Han, B.; Hu, P.; Cao, L.; Zhu, D. *Advanced Materials* **2005,** 17, (2), 217-221.

11. Besteman, K.; Lee, J.-O.; Wiertz, F. G.; Heering, H. A.; Dekker, C. *Nano Letters* **2003,** 3, (6), 727-730.

12. Wang, S.; Zhang, Q.; Wang, R.; Yoon, S.; Ahn, J.; Yang, D.; Tian, J.; Li, J.; Zhou, Q. *Electrochemistry Communications* **2003,** 5, (9), 800-803.

13. Wang, S.; Wang, R.; Sellin, P.; Zhang, Q. *Biochemical and biophysical research*

*communications* **2004,** 325, (4), 1433-1437.

14. Chen, J.; Chen, S.; Zhao, X.; Kuznetsova, L. V.; Wong, S. S.; Ojima, I. *Journal of the American Chemical Society* **2008,** 130, (49), 16778-16785.

15. Liu, Z.; Tabakman, S.; Welsher, K.; Dai, H. *Nano Research* **2009,** 2, (2), 85-120.

16. Liu, Z.; Chen, K.; Davis, C.; Sherlock, S.; Cao, Q.; Chen, X.; Dai, H. *Cancer research* **2008,** 68, (16), 6652-6660.

17. Pastorin, G.; Wu, W.; Wieckowski, S.; Briand, J.-P.; Kostarelos, K.; Prato, M.; Bianco, A. *Chemical Communications* **2006**, (11), 1182-1184.

18. Chen, P.-L.; Chang, J.-K.; Kuo, C.-T.; Pan, F.-M. *Diamond and Related Materials* **2004,** 13, (11–12), 1949-1953.

19. Jeong, S.-H.; Hwang, H.-Y.; Lee, K.-H.; Jeong, Y. *Applied Physics Letters* **2001,** 78, (14), 2052-2054.

20. Wen, S.; Jung, M.; Joo, O.-S.; Mho, S.-i. *Current Applied Physics* **2006,** 6, (6), 1012-1015.

21. Gao, H.; Mu, C.; Wang, F.; Xu, D.; Wu, K.; Xie, Y.; Liu, S.; Wang, E.; Xu, J.; Yu, D. *Journal of Applied Physics* **2003,** 93, (9), 5602-5605.

22. Wen, Z.; Wang, Q.; Li, J. *Advanced Functional Materials* **2008,** 18, (6), 959-964.

23. Ahn, H.-J.; Sohn, J. I.; Kim, Y.-S.; Shim, H.-S.; Kim, W. B.; Seong, T.-Y. *Electrochemistry communications* **2006,** 8, (4), 513-516.

24. Sohn, J. I.; Kim, Y.-S.; Nam, C.; Cho, B.; Seong, T.-Y.; Lee, S. *Applied Physics Letters* **2005,** 87, (12), 123115-123115-3.

25. Masuda, H.; Fukuda, K. *Science* **1995,** 268, 1466-1468.

26. Hinds, B. J.; Chopra, N.; Rantell, T.; Andrews, R.; Gavalas, V.; Bachas, L. G. *Science* **2004,** 303, (5654), 62-65.

27. Karthikeyan, S.; Mahalingam, P.; Karthik, M. *Journal of Chemistry* **2009,** 6, (1), 1-12.

28. Schadler, L.; Giannaris, S.; Ajayan, P. *Applied Physics Letters* **1998,** 73, 3842.

29. Ajayan, P.; Ebbesen, T.; Ichihashi, T.; Iijima, S.; Tanigaki, K.; Hiura, H. **1993**.

30. Colomer, J.-F.; Piedigrosso, P.; Fonseca, A.; Nagy, J. *Synthetic metals* **1999,** 103, (1), 2482-2483.

31. Shi, Z.; Lian, Y.; Liao, F.; Zhou, X.; Gu, Z.; Zhang, Y.; Iijima, S. *Solid State Communications* **1999,** 112, (1), 35-37.

32. Chiang, I.; Brinson, B.; Smalley, R.; Margrave, J.; Hauge, R. *The Journal of Physical Chemistry B* **2001,** 105, (6), 1157-1161.

33. Chen, X.; Chen, C.; Chen, Q.; Cheng, F.; Zhang, G.; Chen, Z. *Materials Letters* **2002,** 57, (3), 734-738.

34. Kang, S. J.; Kocabas, C.; Ozel, T.; Shim, M.; Pimparkar, N.; Alam, M. A.; Rotkin, S. V.; Rogers, J. A. *Nature nanotechnology* **2007,** 2, (4), 230-236.

35. Ren, Z.; Huang, Z.; Xu, J.; Wang, J.; Bush, P.; Siegal, M.; Provencio, P. *Science* **1998,** 282, (5391), 1105-1107.

36. Huang, S.; Dai, L. *The Journal of Physical Chemistry B* **2002,** 106, (14), 3543-3545.

37. Chhowalla, M.; Teo, K.; Ducati, C.; Rupesinghe, N.; Amaratunga, G.; Ferrari, A.; Roy, D.; Robertson, J.; Milne, W. *Journal of Applied Physics* **2001,** 90, (10), 5308-5317.

38. Liang, J.; Chik, H.; Xu, J. *Selected Topics in Quantum Electronics, IEEE Journal of* **2002,** 8, (5), 998-1008.

39. Yin, A.; Chik, H.; Xu, J. *Nanotechnology, IEEE Transactions on* **2004,** 3, (1), 147-151.

40. Shiraishi, M.; Ata, M. *Carbon* **2001,** 39, (12), 1913-1917.

41. Duan, H. Synthesis, Integration, and Characterization of Functional Inorganic Nanomaterials Worcester Polytechnic Institute, 2009.

42. Abràmoff, M. D.; Magalhães, P. J.; Ram, S. J. *Biophotonics international* **2004,** 11, (7), 36-42.

# Paper 2: An Optimized Method to Synthesize Graphene Nanosheets

**Yuqin Yao and Jianyu Liang**

**Abstract**

As a novel 2-D material, graphene has been vigorously studied since its discovery in 2004. Synthesizing methods have been sought by many researchers since graphene was first made by mechanical exfoliation. In this report, the reduction of graphite oxides by chemical and thermal methods has been employed to convert graphite oxide synthesized by a wet chemical method using $KMnO_4$ and $H_2O_2$. with lower temperature and much less toxic gas. Comparing the results from the two reduction methods, it can be concluded that a combination of wet oxidation of graphite and thermal reduction method is an efficient and environmental friendly way to produce as-made samples with more single layered graphene and less oxygen functionalities .

## 1. Introduction

Graphene is a two dimensional planar material with atomic thickness, formed by $sp^2$ hybridized carbon atoms in a honey-comb arrangement. According to previous theory, 2-D crystals could not exist due to their thermal unstability, which resulted in the consideration of graphene only as an "academic" materials for decades[1]. In 2004, graphene was made by Geim and Novoselov by a micro-mechanical exfoliation method, claiming this kind of material does exist in reality[2]. Since then, this unique material has sparked high interest within the nanotechnology research community.

Extensive work has been done on synthesis, characterization and applications of graphene. Both theoretical and experimental studies have revealed outstanding physical properties of GNS such as very high specific area ($1500 m^2 g^{-1}$)[3], extraordinary conductivity ($\sim 2*10^5 Sm^{-1}$)[4], large Young's modulus (~1000GPa)[5], outstanding carrier mobility ($200000 cm^2/(V\ s)$)[6], high chemical and thermal stabilities and exceptional thermal conductivity ($5000 W/(m\ K)$)[5]. These unique properties imply that GNS has huge potential for numerous applications, such as composites[7-9], sensors[10, 11], batteries[12, 13] and solar cells[14-16].

Although the significance of GNS has been recognized by many researchers and scientists, optimization of synthesizing GNS still remains as a challenge[17].

Mechanical exfoliation was the first reported method for producing GNS[2]. However, soon it was found to be time consuming with a yield that is too low for most of the applications[1]. Chemical vapor deposition (CVD)[18, 19] is considered to be a promising method for bulk production. However, strict conditions, such as high temperature and complicated process of substrate treatment still impose limits of this method[1]. Chemical synthesis[20, 21] is considered to be cheap and easy to be tailored. But the first step of this method typically involves the use of strong acid to oxidize natural graphite flakes to graphite oxide (GO), which is considered to be the precursor of graphene. There have been several methods developed for the chemical oxidization process, including Brodie's method[22], Staudenmaier's method[23] and Hammer's method[24]. The common drawback of them is that they all involve explosive reactions, and generation of toxic gas (Table 1). To solve this problem, an improved method to synthesize GO was reported in 2010 by Daniela's group[25]. Compared with traditional methods, this method increased the amount of $KMnO_4$ and eliminated the need of using $NaNO_3$. Also, no toxic gas is generated in this process due to the mild reacting temperature (50℃) compared with conventional method (up to 80℃)[26]. Therefore, this method can serve as an alternative way for safe production of graphite oxide.

Table 1: Drawbacks of three traditional synthesis of graphite oxide

| Method | Chemicals | Duration | Temperature | Toxic gas | Oxidation degree |
|---|---|---|---|---|---|
| Brodie's method | $HNO_3$, $HClO_3$ | 24 hours | 0℃~80℃ | $Cl_2$ | High |
| Staudenmaier's Method | $H_2SO_4$, $HClO_3$, $HNO_3$ | 56 hours | 0℃ | $Cl_2$ | Low |
| Hummer's method | $H_2SO_4$, $KMnO_4$, $NaNO_3$ | 48 hours | 4℃~98℃ | $NO_2$ | High |

Reduction of graphite oxide is the second step in chemical synthesis of GNS. Chemical reduction and thermal reduction are considered to be two of the most efficient methods for scale-up production at low cost[1]. Each of these two methods has its own advantages and disadvantages: GNS produced by chemical reduction can be easily deposited on any substrate with simple process, but chemical reduction is a time consuming process that usually use explosive reductant introduced ($NaBH_4$ and $N_2H_4$, etc.)[1]; thermal reduction is fast (takes only about 1min), but the final product is hydrophobic, which makes it difficult for dispersion and deposition in the post

synthesis steps. Since the reduction process plays a key role in determining the yield, quality, chemical and surface properties of the GNS product, it is important to establish a wet chemical synthesis protocol that considers both the oxidation and reduction steps.

In this report, we adapted a previously reported method to prepare graphite oxide, and compared the two reduction methods to obtain reduced graphene: chemical reduced graphene (CRG) and thermal reduced graphene (TRG). The synthesized graphene nanosheets were characterized by SEM, XRD, Raman, UV-vis spectrometer, FTIR and AFM. Thermal reduction was confirmed to be an effective method to synthesize GNS with more single layered GNS and less oxygen containing groups without further treatment.

## 2. Experimental

In this study, graphite was first oxidized into graphite oxide, and then the graphite oxide was reduced into GNS by (Figure 1): 1) wet chemical method and 2) thermal reduction. The outcomes were compared.

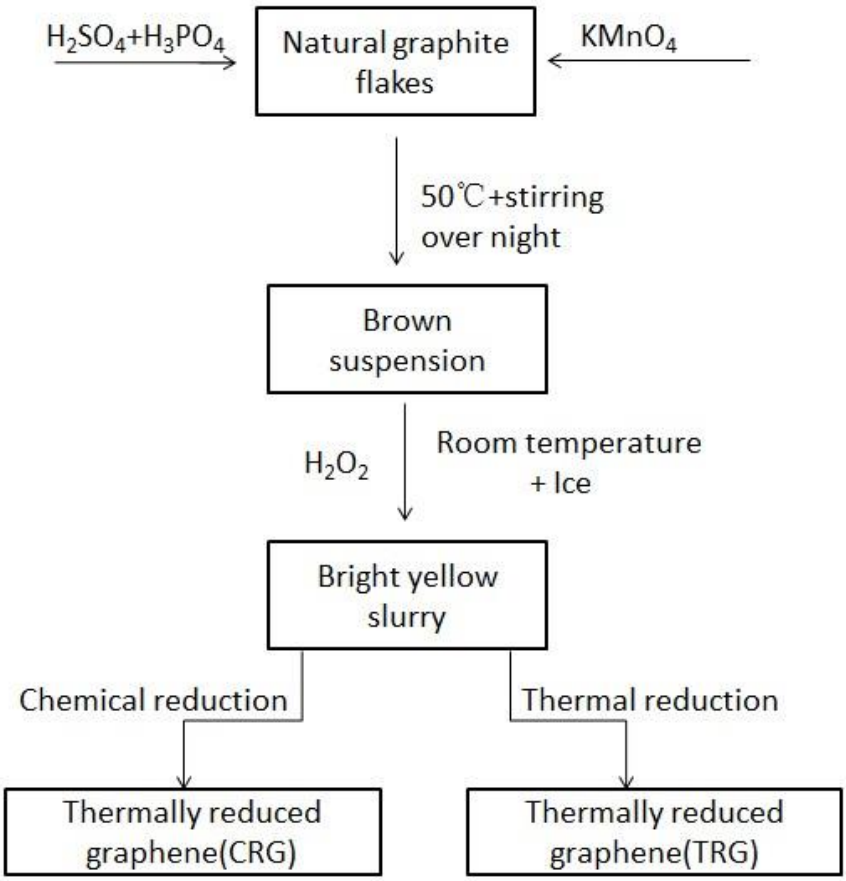


**Figure 1**: Process of sample preparation

**Preparation of graphite oxide** An improved oxidation of graphite process has been adapted[25]. Typically, a mixture of $H_2SO_4$ and $H_3PO_4$ was added into a mixed powder, which contained natural graphite flakes and $KMnO_4$ (2.5g and 15g, respectively). The suspension was heated up to 50℃ and kept stirring for about 12 hours, and followed by cooling the whole system down to room temperature. Then, the suspension was poured onto ice (made from D.I. water, 400ml) and kept stirring for another 4 hours. Finally, 4ml $H_2O_2$ was added into the suspension. The color of the suspension turned into bright yellow immediately, which is the featured color of graphite oxide.

**Synthesize of graphene nanosheets**

1. Chemical reduction: Although many redcutants and methods were investigated since the chemical reduction method was developed[1], reduction by hydrazine is still one of the most popular methods to convert graphite oxide to GNS[27]. Firstly, the as-made graphite oxide (2.5g) was dispersed in N,N-Dimethylformamide (DMF) by sonicating for 2 hours; then 10ml hydrazine was added into the suspension, which was stored in a four neck flask; thirdly, the mixture was heated up to 100℃ under the protection of nitrogen and kept refluxing overnight; finally, as-made graphene nanosheets was collected by centrifuging, and then dried in a vacuum oven for 8 hours.

2. Thermal reduction: For a typical thermal reduction, 2.5g graphite oxide was placed in a quartz tube. The tube was exposed to 1000℃ in a tube furnace for 30 seconds in Ar atmosphere; and then cooled down to room temperature.

**Characterizations**

The morphology of TRG and CRG were investigated by scanning electronic microscopy (SEM JOEL 7000F); Crystallographic information of the samples was investigated with X-ray powder diffraction (XRD, Cu Kα radiation at λ=1.54Å). The oxygen containing groups were confirmed by Fourier transformation infrared spectroscopy (FTIR, FTIR Spectrometer Tensor 37, BrukerOptics). UV-vis absorption spectra of both TRG and CRG were obtained by UV-vis spectrophotometer (DU 640, 600 Series). AFM images were taken by AFM microscopy (MFP3D Bio, Asylum Research) and Raman spectra were collected by Raman spectrometer (Agiltron,

PEK-785)

## 3. Results and Discussion

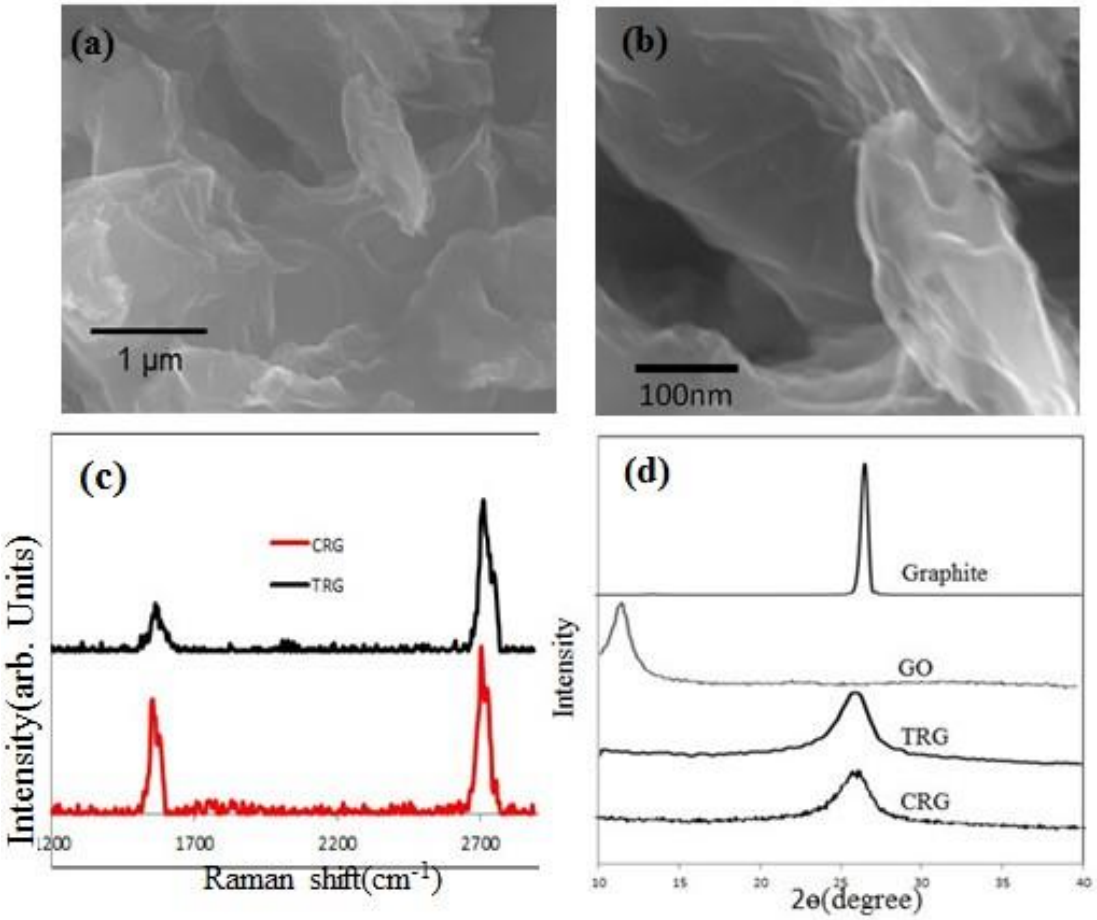


**Figure 2**: (a) and (b): SEM pictures of CRG and TRG; (c) Raman spectroscopy of CRG and TRG; and (d) XRD results of natural graphite, graphene oxide, TRG and CRG, respectively.

Without further purification, CRG and TRG were characterized by SEM (Figure 1(a) and (b)). It is well known that SEM is very useful to provide morphology information. However, it is hard to determine the precise thickness of as-made graphene samples by SEM. Therefore, Raman spectroscopy was employed to investigate the thickness of graphene samples (Figure 2(c)). In Raman, graphene presents two fingerprint peaks, G band around 1580cm$^{-1}$, which stands for C=C bond stretching and 2D band around 2700cm$^{-1}$, which is caused by the double resonance process. It is an established practice to us $I_D/I_G$ as a standard to determine the number of layers of as-fabricated GNS[28, 29]. From Figure 2(c), it is obvious that $I_D/I_G$ of TRG

is higher than that of CRG, which implies that TRG contains more single layered GNS[30].

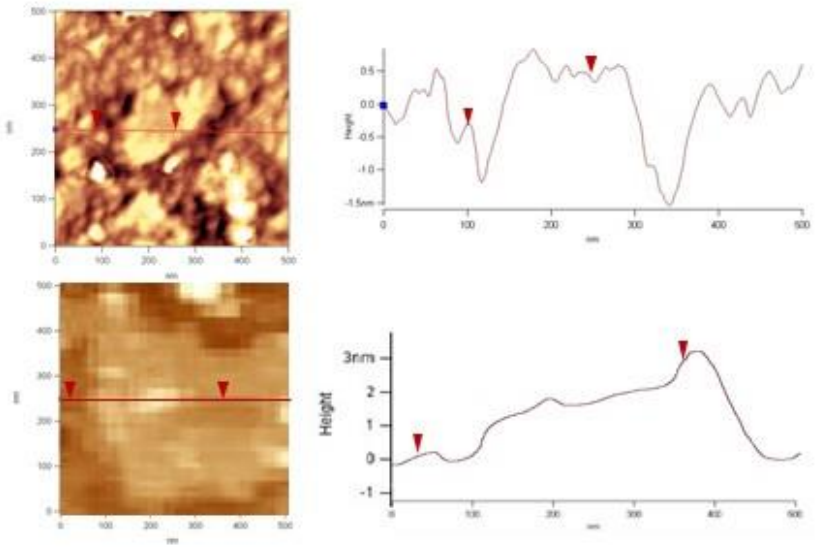


**Figure 3**: AFM image of TRG (upper) and CRG (lower)

XRD was also performed on graphite flakes, graphite oxide, TRG and CRG samples (Figure 2(d)). For natural graphite, there's a sharp peak at about 26 degree, which is the featured peak of graphite at (002). After oxidization, the peak (002) disappears while a new peak at 10.6 degree appears, which is the featured peak of graphene oxide at (001). It indicates that graphite structure has been changed and another crystal structure has formed. After reduction, the graphene oxide peak at (001) disappears while a wide peak at graphite (002) comes back, but the intensity is weak, which implies that after reduction, the size of the graphite layer becomes much smaller and the crystal integrity decreases while the disorder parameter increases. However, it is hard to tell the difference between the XRD patterns of TRG and CRG, because their interplane spacings are very close.

AFM images (Figure 3) indicates the thickness of TRG (~1nm) is thinner than that of CRG (3~4nm), which also confirms the result of Raman spectroscopy.

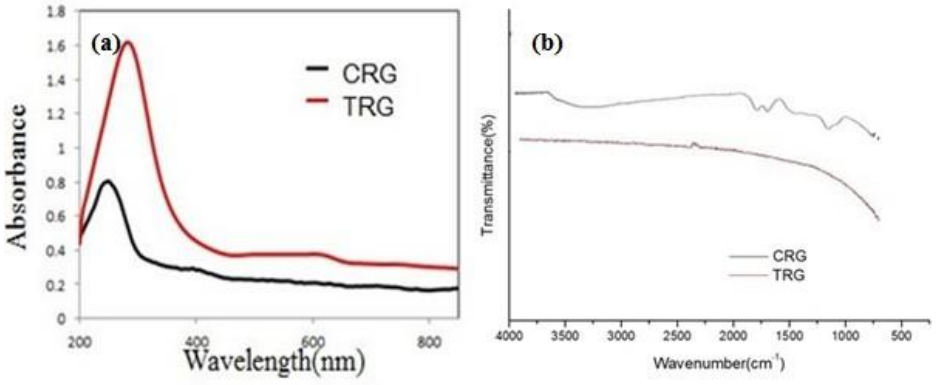


**Figure 4**: (a) UV-Vis spectroscopy of TRG and CRG; (b) FT-IR of GO, TRG and CRG

Both CRG and TRG were dispersed for UV-Vis test (Figure 4(a)). It is well known that for GNS, it has a fixed absorption peak at the wavelength of 273nm[27]. As the result shows, TRG has a stronger absorption peak than CRG, which implies that thermal reduction process was able to restore more π conjugations than chemical reduction did. Fourier Transform infrared spectroscopy (FTIR) test was employed to (Figure 4(b)) identify different functional groups, such as C=O groups (1720-1740$cm^{-1}$), C=C unoxdized bondings (1590~1620$cm^{-1}$) and C-O vibrations(1250$cm^{-1}$). According to the results (Figure 4(b)), TRG has much less residual oxygen-containing groups, which means that thermal reduction has a better efficiency in removing oxygen containing groups. In GO, the aromatic carbon lattice is interrupted by oxygen containing groups, which leads to poor conductivity. So for applications that require to remove as much oxygen functionality as possible to retain excellent conductivity, the results here suggest that thermal reduction is no doubt the better approach.

## 4. Conclusions

In summary, it was confirmed that combined with improved synthesis of graphite oxide, thermal redcution can produce graphene nanosheets that are thinner and contains less oxygen functionality. In addition, thermal reduction method provides several advantages: 1. Environmental friendly: not only because there was no toxic gas during the oxidation step, but also the reducing reaction was safe without any toxic chemicals; 2. Fast process: compared with the chemical reducing method, thermal reduction is much faster. Besides, there was much less residue left among the as-made sample after thermal reduction; 3. High quality: compared with chemical

reduction, the amount of single layered GNS after thermal reduction is much more than that after chemical reduction, which implies this routine to synthesize GNS has good potential for the future industrial applications.

## References


1. Guo, S.; Dong, S. *Chem. Soc. Rev.* **2011,** 40, (5), 2644-2672.

2. Novoselov, K. S.; Geim, A. K.; Morozov, S. V.; Jiang, D.; Zhang, Y.; Dubonos, S. V.; Grigorieva, I. V.; Firsov, A. A. *Science* **2004,** 306, (5696), 666-669.

3. Schniepp, H. C.; Li, J. L.; McAllister, M. J.; Sai, H.; Herrera-Alonso, M.; Adamson, D. H.; Prud'homme, R. K.; Car, R.; Saville, D. A.; Aksay, I. A. *The Journal of Physical Chemistry B* **2006,** 110, (17), 8535-8539.

4. Wu, Z. S.; Ren, W.; Gao, L.; Zhao, J.; Chen, Z.; Liu, B.; Tang, D.; Yu, B.; Jiang, C.; Cheng, H. M. *ACS Nano* **2009,** 3, (2), 411-417.

5. Savage, N. *Nature* **2012,** 483, (7389), S30-S31.

6. Geim, A. K.; Novoselov, K. S. *Nat Mater* **2007,** 6, (3), 183-191.

7. Wang, Z. M.; Hoshinoo, K.; Shishibori, K.; Kanoh, H.; Ooi, K. *Chemistry of Materials* **2003,** 15, (15), 2926-2935.

8. Stankovich, S.; Dikin, D. A.; Dommett, G. H. B.; Kohlhaas, K. M.; Zimney, E. J.; Stach, E. A.; Piner, R. D.; Nguyen, S. B. T.; Ruoff, R. S. *Nature* **2006,** 442, (7100), 282-286.

9. Huang, X.; Qi, X.; Boey, F.; Zhang, H. *Chemical Society Reviews* **2012,** 41, (2), 666-686.

10. Schedin, F.; Geim, A.; Morozov, S.; Hill, E.; Blake, P.; Katsnelson, M.; Novoselov, K. *Nature materials* **2007,** 6, (9), 652-655.

11. He, Q.; Sudibya, H. G.; Yin, Z.; Wu, S.; Li, H.; Boey, F.; Huang, W.; Chen, P.; Zhang, H. *ACS Nano* **2010,** 4, (6), 3201-3208.

12. Yang, S.; Cui, G.; Pang, S.; Cao, Q.; Kolb, U.; Feng, X.; Maier, J.; Müllen, K. *ChemSusChem* **2010,** 3, (2), 236-239.

13. Li, B.; Cao, H.; Shao, J.; Li, G.; Qu, M.; Yin, G. *Inorganic Chemistry* **2011,** 50, (5), 1628-1632.

14. Tang, Y. B.; Lee, C. S.; Xu, J.; Liu, Z. T.; Chen, Z. H.; He, Z.; Cao, Y. L.; Yuan, G.; Song, H.; Chen, L. *ACS Nano* **2010,** 4, (6), 3482-3488.

15. Wang, X.; Zhi, L.; Müllen, K. *Nano Letters* **2008,** 8, (1), 323-327.

16. Hong, W.; Xu, Y.; Lu, G.; Li, C.; Shi, G. *Electrochemistry Communications* **2008,** 10, (10), 1555-1558.

17. Daniela C. Marcano, D. V. K., Jacob M. Berlin, Alexander Sinitskii, Zhengzong Sun, Alexander Slesarev, Lawrence B. Alemany, Wei Lu, and James M. Tour. *ACS Nano* **2010,** 4, (8), 4806-4814

18. Li, X.; Cai, W.; An, J.; Kim, S.; Nah, J.; Yang, D.; Piner, R.; Velamakanni, A.; Jung, I.; Tutuc, E. *Science* **2009,** 324, (5932), 1312-1314.

19. Chen, S.; Cai, W.; Piner, R. D.; Suk, J. W.; Wu, Y.; Ren, Y.; Kang, J.; Ruoff, R. S. *Nano Letters* **2011,** 11, (9), 3519-3525.

20. Stankovich, S.; Dikin, D. A.; Piner, R. D.; Kohlhaas, K. A.; Kleinhammes, A.; Jia, Y.; Wu, Y.; Nguyen, S. B. T.; Ruoff, R. S. *Carbon* **2007,** 45, (7), 1558-1565.

21. Stankovich, S.; Piner, R. D.; Chen, X.; Wu, N.; Nguyen, S. B. T.; Ruoff, R. S. *Journal of Materials Chemistry* **2006,** 16, (2), 155-158.

22. Jeong, H.-K.; Lee, Y. P.; Lahaye, R. J.; Park, M.-H.; An, K. H.; Kim, I. J.; Yang, C.-W.; Park, C. Y.; Ruoff, R. S.; Lee, Y. H. *Journal of the American Chemical Society* **2008,** 130, (4), 1362-1366.

23. Nakajima, T.; Matsuo, Y. *Carbon* **1994,** 32, (3), 469-475.

24. Hummers Jr, W. S.; Offeman, R. E. *Journal of the American Chemical Society* **1958,** 80, (6), 1339-1339.

25. Marcano, D. C.; Kosynkin, D. V.; Berlin, J. M.; Sinitskii, A.; Sun, Z.; Slesarev, A.; Alemany, L. B.; Lu, W.; Tour, J. M. *ACS Nano* **2010,** 4, (8), 4806-4814.

26. Zhu, Y.; James, D. K.; Tour, J. M. *Advanced Materials* **2012,** 24, (36), 4924-4955.

27. Li, D.; Müller, M. B.; Gilje, S.; Kaner, R. B.; Wallace, G. G. *Nature nanotechnology* **2008,** 3, (2), 101-105.

28. Röhrl, J.; Hundhausen, M.; Emtsev, K.; Seyller, T.; Graupner, R.; Ley, L. *Applied Physics Letters* **2008,** 92, 201918.

29. Ferrari, A. C.; Meyer, J. C.; Scardaci, V.; Casiraghi, C.; Lazzeri, M.; Mauri, F.; Piscanec, S.; Jiang, D.; Novoselov, K. S.; Roth, S.; Geim, A. K. *Physical Review Letters* **2006,** 97, (18).

30. Ferrari, A. C. *Solid State Communications* **2007,** 143, (1), 47-57.

# Paper 3: Fabrication of $TiO_2$-graphene composite for enhanced performance of Lithium batteries

**Yuqin Yao[1], Yinjie Cen[1], Quan Xu[2,] Zhenhai Xia[2], Richard D. Sisson[1] and Jianyu Liang[1*]**

1. **Department of Mechanical Engineering, Worcester Polytechnic Institute, Worcester, MA, 01609;**
2. **Department of Mechanical Engineering, University of North Texas, Denton, TX, 76203.**

## Abstract

$TiO_2$ nanoparticles (NPs) synthesized by a facile sol-gel method were encapsulated in graphene nanosheets (GNS) to enhance its performance as anode active materials in Li-ion batteries. The encapsulation was facilitated by electrostatic interaction between the positively charged surface of $TiO_2$ with silane decoration and the negatively charged graphene oxide. Followed by reduction of the graphene oxide wrapped $TiO_2$ nanoparticles, graphene encapsulated $TiO_2$ nanocomposite was successfully fabricated. SEM and TEM revealed the uniform and individual conformal wrapping of $TiO_2$ by graphene. XRD results further validated uniform distribution of graphene within anatase $TiO_2$. FTIR and Zeta potential results confirmed that the electrostatic interaction was effective in facilitating uniform wrapping of graphene oxide around $TiO_2$ NPs. Electrochemical performance of the nanocomposite was tested by cyclic voltammetry and coin cell tests. The graphene encapsulated $TiO_2$ materials demonstrated a very high initial capacity of 409mA ħ/g at 1C and retained a capacity of 141 mA ħ/g at 20C. The nanocomposite electrode also showed a Coulombic efficiency above 98% and good long term cycling performance (as high as 343mAh/g after 100 cycles) at a rate of 1C. Possible mechanisms resulting in the observed improved performance are discussed in this report.

## 1. Introduction

Alternative electrode materials for Lithium-ion batteries(LIBs) have been extensively studied for portable devices and hybrid electric vehicles due to the demand of these applications for large cycling capacity and long cycle life at high

charging and discharging speed[1]. Compared with traditional graphite anode materials, transition metal oxides($Fe_3O_4$[2-4], $TiO_2$[5, 6], $Co_3O_4$[7-9] and $SnO_2$[10-12], etc.) enable a different reaction chemistry(convention reaction) and provide high theoretical capacity. The convention reaction of metal oxides can be written as equation 1:

$$M_xO_y+2ye^-+2yLi^+ \leftrightarrow x(M)^0+yLi_2O \quad (1)$$

Where M is a transition metal, such as Co, Fe, Cu and Sn, etc. Among them, $TiO_2$ is an interesting candidate for anode because of its relatively good structural stability compared with other metal oxides[13], environmental friendliness and cost-effectiveness. Typical anatase $TiO_2$ was reported with a theoretical capacity of 330mA ħ/g[14]. However, there are several drawbacks of this material, including 1) poor conductivity, which is common for most metal oxides; 2) need of efficient diffusion paths due to the difficulty of controlling the particle size shape and morphology[15]; and 3) significant capacity decay due to aggregation and volume expansion[15-17]. Generally speaking, there are several factors that influence Li storage and cycling in $TiO_2$, such as particle size($\leq$200nm is desired), crystalline structure and morphology[14]. Therefore, many attempts have been made to optimize $TiO_2$ nanoparticle synthesizing methods such as anodization[18, 19], sol-gel method[20, 21], hydrothermal method[22, 23], molten salt method[24] and soft template method[25, 26] to enable effective control over the phase, size, shape, and morphology of the product. Among them, sol-gel method provides products with low degree of aggregation and relatively good controllability over nano particle size[27] at relatively mild conditions. However, the capacity decay during charging and discharging cycles of the products is still a significant issue.

Many $TiO_2$ nano structures have been synthesized and tested, including nanoporous $TiO_2$ particles[28] with a reported capacity of 229mA ħ/g, $TiO_2$ nano sheets[29] with a reported capacity of 202mA ħ/g and $TiO_2$ pseudocube[14] with a reported capacity of 131mA ħ/g, etc. A common observation was that most synthesized $TiO_2$ nano-structures showed a significant decay (up to 30%) after 20 cycles even at relatively low cycling rate such as 0.5~1C rate[15, 30-32]. Typically, it is difficult to fully access the theoretical capacity of $TiO_2$ and address the capacity decay issue only with nanostructures.

Carbon coating was considered as an efficient way to enhance the electronic conductivity and also serve as a cushion to absorb the volume change of metal oxides[33] during cycling. Therefore, diverse methods have been developed to fabricate

metal oxide and carbon composites, such as mechanical mixing[34], solvothermal method[35] and in-situ method[36]. However, the carbon incorporation is typically disordered. There are a couple of common obstacles to be overcome[37], including the need to lower the carbon content because high carbon content leads to relatively low amount of metal oxides content in the composite electrode and thus, the lower than expected capacity improvement from metal oxides; and the need to improve the crystalline quality of carbon coating that will result in better conductivity towards improving cycling performance.

Graphene nanosheets(GNS), as a 2-D material with tight honeycomb arrangement of $sp^2$ hybridized carbon atoms has shown many favorable properties for LIB application, such has high carrier mobility(200,000$cm^2 \cdot V^{-1} \cdot S^{-1}$)[38], exceptional mechanical stiffness(125GPa)[39], excellent electric conductivity(2000$S \cdot cm^{-1}$)[40], good thermal conductivities(4840-5300$W \cdot m^{-1} \cdot K^{-1}$)[41] and large specific areas(2630$m^2 \cdot g^{-1}$)[42]. GNS itself has been studied as an anode material for LIB, and has shown high reversible capacity(~1000mA ħ/g) and good capacity retention at high rates with a capacity of 250mA ħ/g at 2.1A/g[43, 44]. Due to the high cost, GNS is most commonly incorporated into metal oxides to form metal oxides/GNS composites ($SnO_2$/graphene[45, 46], $TiO_2$/graphene[47], $Fe_3O_4$/graphene[48, 49], and $Co_3O_4$/graphene[50, 51]) to enhance the electrochemical performance.

Recently, GNS encapsulated $TiO_2$ nanoshells have been reported[52] with initial capacity of 200mA ħ/g and reversible capacity of ~150 mA ħ/g at 1C after 100 cycles. The static electric assembly of GNS on $TiO_2$ surface is an interesting approach that demands further investigation, especially to get a clear view and understanding of the GNS wrapping on individual $TiO_2$ nano structures. Since the mechanical properties and intrinsic limit of volume capacities of nanoshells might not render them significant advantages over nano particles for large scale applications, it is worthwhile to look into the GNS encapsulated $TiO_2$ nanoparticles for LIB applications.

Herein, we fabricated a GNS encapsulated $TiO_2$ anatase NPs through a facile method followed by a self-assembly and reduction process. XRD, SEM and TEM were used to investigate the crystalline structure and morphology of the sample. FTIR and zeta potential were employed to identify the functional groups and charging information of the samples. Coin cells were assembled to test the electrochemical performance of the as-made electrode. The graphene encapsulated $TiO_2$ materials showed an initial capacity as high as 409mA ħ/g at 1C and demonstrated a relatively

high capacity of 141mA ħ/g at 20C. The nanocomposite electrode also showed a Coulombic efficiency above 98% and exhibited an excellent long term cycling performance (as high as 343mAh/g after 100 cycles) at a 1C rate.

## 2. Experimental

Figure 1 briefly depicts the process of synthesizing $TiO_2$/GNS nanocomposite: first anatase $TiO_2$ NPs were synthesized by sol-gel method[53] and natural graphite flakes were oxidized to form stable graphite oxide(GO) suspension in N,N-Dimethylformamide(DMF)[54]; then, as-made $TiO_2$ NPs were treated with (3-aminopropyl)triethoxysilane(APTES) to introduce positive charges to their surface, followed by mixing them with GO and dispersing in DMF; finally, the $TiO_2$/GO slurry was reduced by hydrazine to obtain the $TiO_2$/GNS nanocomposite.

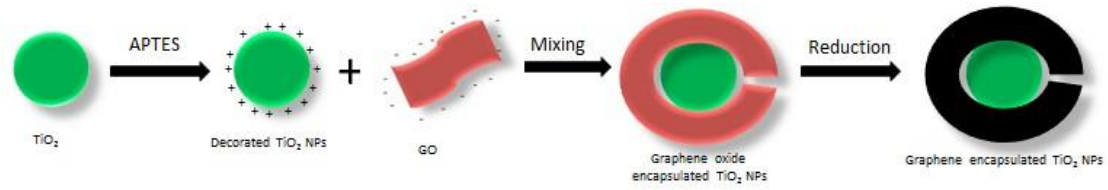


**Figure 22:** Schematics of the synthesis process of graphene encapsulated TiO2 NPs

### 2.1 Synthesis of $TiO_2$ nanoparticles

3.42 ml tetrabutyl orthotitanate (TBOT, Sigma-Aldrich, 97%) and 0.57 ml acetic acid (99%, Sigma Aldrich) were dispersed in 4.67 ml ethanol. After stirring vigorously for a few minutes, a mixture of 0.54 ml D.I. water and 2.33 ml acetic acid was added to the above solution under stirring. Then $TiO_2$ gel was placed in an oven at 60℃ for 24h. Finally, the particles were obtained by calcinating at 450℃ for 3h.

### 2.2 Synthesis of graphite oxide

GO was synthesized by adapting a reported method[55]. First of all, a 9:1 mixture of concentrated $H_2SO_4$(95~98%, Alfa Aesar)/$H_3PO_4$(85%, Alfa Aesar)(300:40mL) was added to a mixture of natural graphite flakes(2.5g，99.9%, Alfa Aesar) and $KMnO_4$ (15g, >99%, Sigma Aldrich). The reaction was then heated to 50℃ and stirred for 12h. Finally the reaction was cooled to room temperature and poured onto ice(~400mL) with 30% $H_2O_2$ (3mL, 30%, Sigma Aldrich) to form stable

bright yellow suspension.

### 2.3 Surface treatment of $TiO_2$ nanoparticles

0.6g as-made $TiO_2$ NPs were added into 60ml methanol and sonicated for 30 minutes. Then certain amount of (3-aminopropyl)triethoxysilane (99%, Sigma Aldrich) was added into the suspension and stirred for another 1 hour. After the homogenizing step, the treated particles were collected by vacuum filtration and then dried overnight in a vacuum oven.

### 2.4 Synthesis of $TiO_2$/GNS composite

500mg pre-treated $TiO_2$ NPs were dispersed in 500ml DMF by sonication. When a homogenous white suspension occurred, 100mg graphite oxide powder was introduced and kept sonicating for another 2 hours. Then, hydrazine was added under nitrogen protection. Then reaction was kept at 95℃ for overnight. The resultant black particles were collected by centrifuging and washed with ethanol. Finally, the as-made composite was dried in the vacuum oven for 12 hours.

### 2.5 Characterization

The morphology of bare $TiO_2$ NPs and graphene encapsulated $TiO_2$ NPs were investigated by scanning electronic microscopy (SEM JOEL 7000F); Crystallographic information of the samples were investigated with X-ray powder diffraction (XRD, Cu Kα radiation at λ=1.54Å). The oxygen containing groups of GO were confirmed by Fourier Transformation Infrared Spectroscopy (FTIR, FTIR Spectrometer Tensor 37, BrukerOptics). AFM images were taken by AFM microscopy (MFP3D Bio, Asylum Research) and Zeta potential of GO and decorated $TiO_2$ NPs was collected by Zetasizer nano series (ZEN3600, Malvern Instruments Limited).

### 2.6 Electrochemical tests

The electrochemical tests were conducted by using a half-coin cell setup with lithium foil as counter electrode. For preparation of testing electrode**,** $TiO_2$ or $TiO_2$/GNS composite was mixed with acetylene black and poly vinylidene fluoride (PVDF) at a ratio of 80:10:10, respectively. The black slurry was casted on copper foil as anode by a doctor blade. The electrode was first dried at 60℃ for 12 hours and

then kept at 120℃ for overnight to remove all the solvents. The coin cell was assembled in a glove box. The electrolyte was 1mol $LiPF_6$ dissolved in a mixed solution of dimethyl carbonate (DMC) and ethyl carbonate(EC). The electric performance was tested between 1 and 3V and the charging rate was calculated based on the anatase $TiO_2$ theoretical capacity of 330mA ħ/g[55].

## 3. Results and Discussion

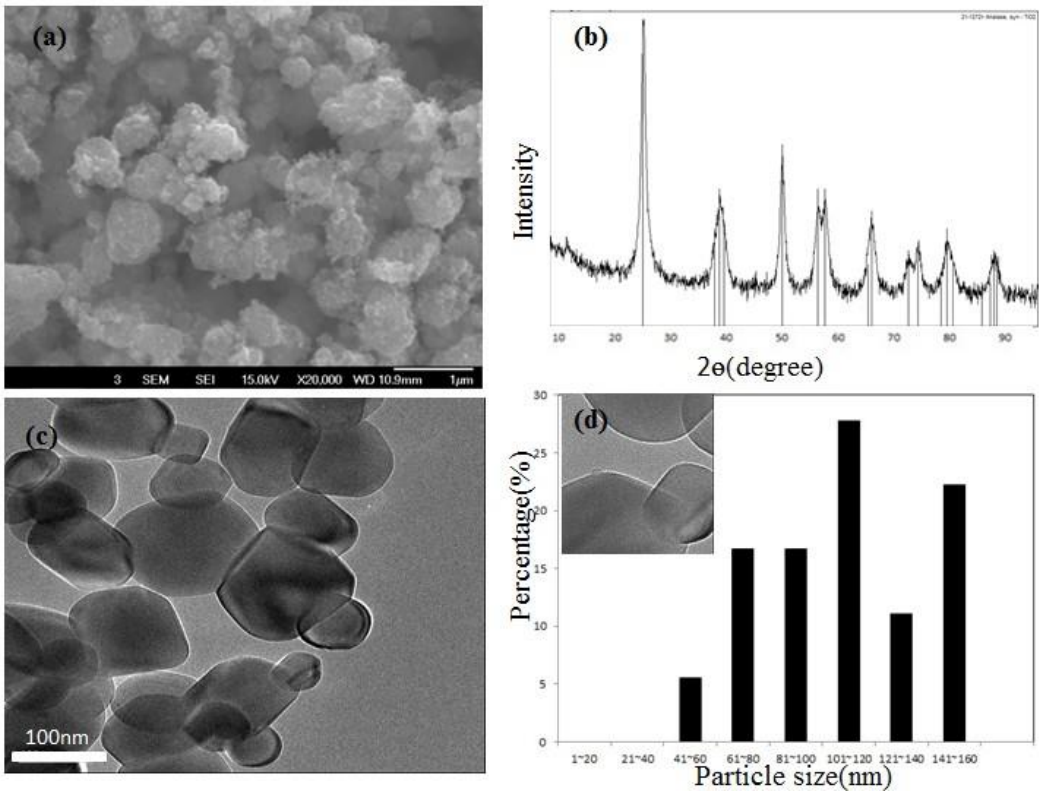


**Figure 23**: (a) and (b): SEM images of TiO2 NPs (c)TEM image of bare $TiO_2$ NPs (d) XRD pattern of graphene-encapsulated TiO2 NPs.

Figure 2(a) is the SEM image and Figure 2(c) is the TEM image of as-made $TiO_2$ NPs, confirming that the $TiO_2$ NPs have been successfully synthesized. The inset of Figure 2(d) is the zoom in image of $TiO_2$ NPs, showing the clear boundary of individual particles.

It is well known that anatase $TiO_2$ is the most electroactive phase of $TiO_2$ for Li storage[56]. Previous thermodynamics[57] and experimental studies[58] have suggested that during a specific sol-gel method, the calcination temperature dominates the phase composition of the $TiO_2$ NPs. Based on the precursor employed in our method and previous knowledge on phase dependence on calcination temperature, 500℃ was

chosen for calcination. The XRD spectrum (Figure 2(b)) confirmed that the desirable anatase $TiO_2$ (JCPDS 21-1272, S.G.: $I4_1/amd$, a=2.7852Å, c=9.5139Å) phase was reliably obtained.

Image J[59] was employed to analyze the size distribution of $TiO_2$ NPs(Figure 2(d)). It is quite clear that the $TiO_2$ particle size ranged from 40nm to 200nm. Previous studies[15, 17, 60] suggested that small particle size (≤200nm) was highly desirable for facilitating insertion & extraction of Li ions and deliver high and stable reversible capacity. It was believed that for nano-structured $TiO_2$ NPs, interfacial $Li^+$ storage will contribute to the overall capacity beyond the conventional bulk $TiO_2$, i.e., extra $Li^+$ can be stored at the interfaces of nano-structured $TiO_2$ materials[17, 28, 60-63]. Thus, with the reduced particle size, it is possible to both insert more $Li^+$ ions and shorten the $Li^+$ diffusion length[55]. The size of sol-gel synthesized $TiO_2$ NPs is known to be determined by many factors, among them pH of the sol-gel reaction environment, calcination temperature and duration play important roles[64]. In order to obtain nanoparticles smaller than 200nms, at a calcination temperature of 500℃, a duration of 2 hours was determined to be sufficient to provide needed phase as well as size control[65].

Figure 3(a) is the SEM and Figure 3(b) is the TEM image of graphene. AFM study (Figure 3(c)) revealed that the thickness of GNS synthesized by wet chemical method ranged from 4~8nm, with an average thickness of 6nm.

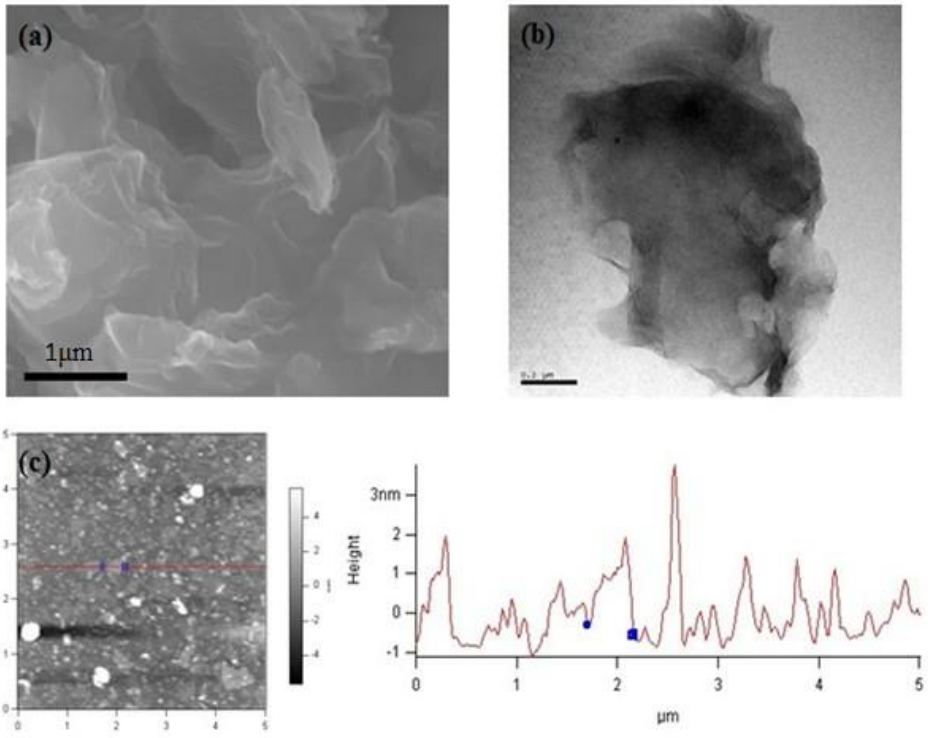

**Figure 3:** (a) SEM image, (b) TEM image and (c) AFM image of GNS.

The functional groups on the decorated $TiO_2$ NPs and GO were confirmed by FTIR, (Figure 4(a) and (b)) and the charge information of those two colloids were collected by zeta-potential measurements (Figure 4(c) and (d)). For GO, dominating oxygen containing groups were identified in FTIR spectra, such as O-H groups (3420 $cm^{-1}$), C=O groups (1720-1740$cm^{-1}$) and C-O vibrations (1250$cm^{-1}$). The existence of these functional groups is believed to contribute to the negative charges on the surface of GO[66]. This is supported by the mean Zeta potential of GO in aqueous environment, -23.8mV, indicating negative charge on GO. For decorated $TiO_2$ NPs (Figure 4(b)), the main characteristic FTIR peaks at 692$cm^{-1}$ and 1509$cm^{-1}$ are assigned to the N-H bending vibration and –NH- deformation vibration[67]. This indicates that the surface of $TiO_2$ NPs was successfully decorated by APTES components during the modification. The Zeta potential tests showed a mean value of 20.64mV confirming the positive charge on decorated $TiO_2$ NPs. So we can conclude that GO and decorated $TiO_2$ NPs have opposite charges, and may be assembled by static electric attractive force.

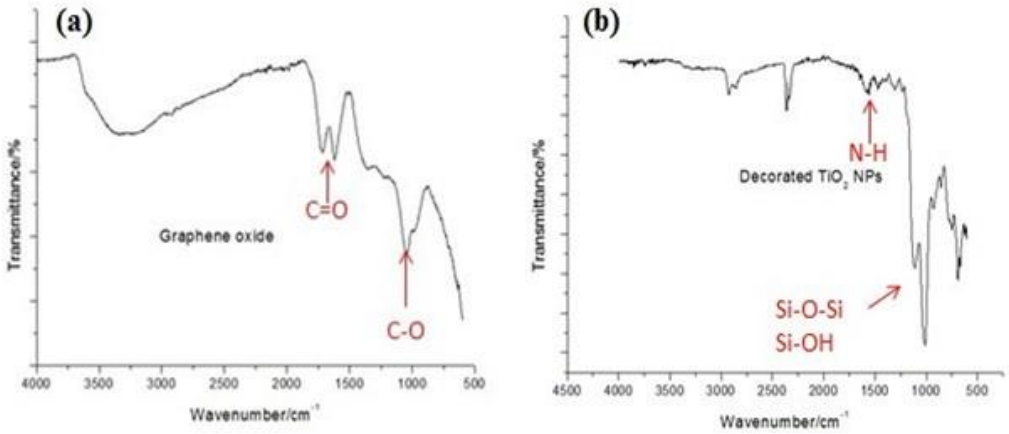


**Figure 4:** (a) and (b): FTIR spectra of GO and decorated $TiO_2$ NPs, respectively.

SEM study strongly suggested that $TiO_2$ NPs were successfully encapsulated by GNS (Figure 5(a)). TEM study confirmed the successful and uniform encapsulation. Figure 5(b) is the TEM image of graphene-encapsulated $TiO_2$ NPs. Those NPs were clearly encapsulated by uniform and ultrathin graphene sheets. The thickness of graphene layer was 4~5nm, which agrees well with the measured graphene thickness by AFM. A simple calculation was also carried out to determine if this thickness of graphene coating is reasonable assuming: (1) $TiO_2$ NPs have the same diameter; two boundary conditions were considered to determine the graphene

thickness range: 40nm, when $TiO_2$ NPs were all 40 nm in size, the thinnest graphene coating would be determined, and 200nm, when $TiO_2$ were all 200nm in size, the thickness graphene coating would be determined; (2) The shape of $TiO_2$ NPs is sphere; (3) continuous, conformal and uniform GNS coating were formed the same on each $TiO_2$ NPs; (4) 100% of GNS were coated on $TiO_2$ NPs; (4) 100% of GNS were coated on $TiO_2$ NPs. Using the TGA results (Figure 5(d)), density of anatase $TiO_2$($3.84g/cm^3$), and planar density of single layer graphene($0.77mg/m^2$), it was determined that if assuming a 40nm diameter of all $TiO_2$ NPs, the GNS coating thickness would be 2.34nm, while assuming a 200nm diameter of all $TiO_2$ NPs resulted in the GNS coating thickness of 9.34nm. Given the $TiO_2$ NPs size distribution (Figure 2(d)) and the factor that it is unlikely that 100% GNS are coated on the $TiO_2$ NPs, we can expect the GNS coating thickness to be in the lower part of the 2.34nm~9.34nm range. The experimental results of 4~5nm coating thickness agrees very well with our expectation.

Compared with typical carbon coating, this uniform and conformal GNS encapsulation structure can (1) effectively buffer the strain caused by frequent charging and discharging process; (2) enhance the overall conductivity of the electrode due to the fast electron transport enabled by GNS; (3) provide a high $TiO_2$ content in the composite; (4) alleviate the aggregation problem of the bare $TiO_2$ NPs since individual and conformal GNS wrapping may significantly benefit the desirable formation of an effectively interconnected network of GNS with uniformly distributed $TiO_2$ NPs embedded, hence providing easy access to each nanoparticle and alleviate the capacity issue caused by agglomeration of individual $TiO_2$ NPs and (5) GNS may also contribute to improve the electrode capacity[68].

From Figure 5(c), all diffraction peaks of $TiO_2$/graphene were indexed to the anatase $TiO_2$ and no peak of graphene at $2\theta=26.6°$ was found, which suggested that graphene nanosheets were homogeneously dispersed on the surface of $TiO_2$ NPs. TGA (Figure 5(d)) result showed that the weight fraction of $TiO_2$ in the composite was as high as 93.6%. This high $TiO_2$ content associated with flexible and ultrathin graphene matrix is considered to be very beneficial towards resulting in high capacity and excellent cycle performance. Previous studies[69] have shown that in order to form an effective conducting network, two requirements need to be satisfied: 1. Uniform distribution of GNS that forms firm and conformal contact with the $TiO_2$ NPs; and 2.Balanced ratio of GNS to $TiO_2$ NPs. The ultrathin and flexible feature of GNS

facilitates the homogeneous dispersion within the particles, which not only can serve as a 'bridge' to build up a conducting network within the composite, but also can provide firm contact with the active materials even under fast charging and discharging process. It was also pointed out in a previous study that increased GNS amount beyond certain point would lead to aggregation among GNS, which would block diffusion of the $Li^+$ ions and increase the charge-transfer resistance[70]. Some previous studies have reported improved electrochemical performance when carbon nanotubes or GNS were incorporated into active materials between 2%~50%[69, 71]. Thus, a 6.4% content of GNS in the final composite is within our desired range. However, a systematic study to determine the optimal GNS to $TiO_2$ NPs ration is beyond the scope of this report and planned for following reports.

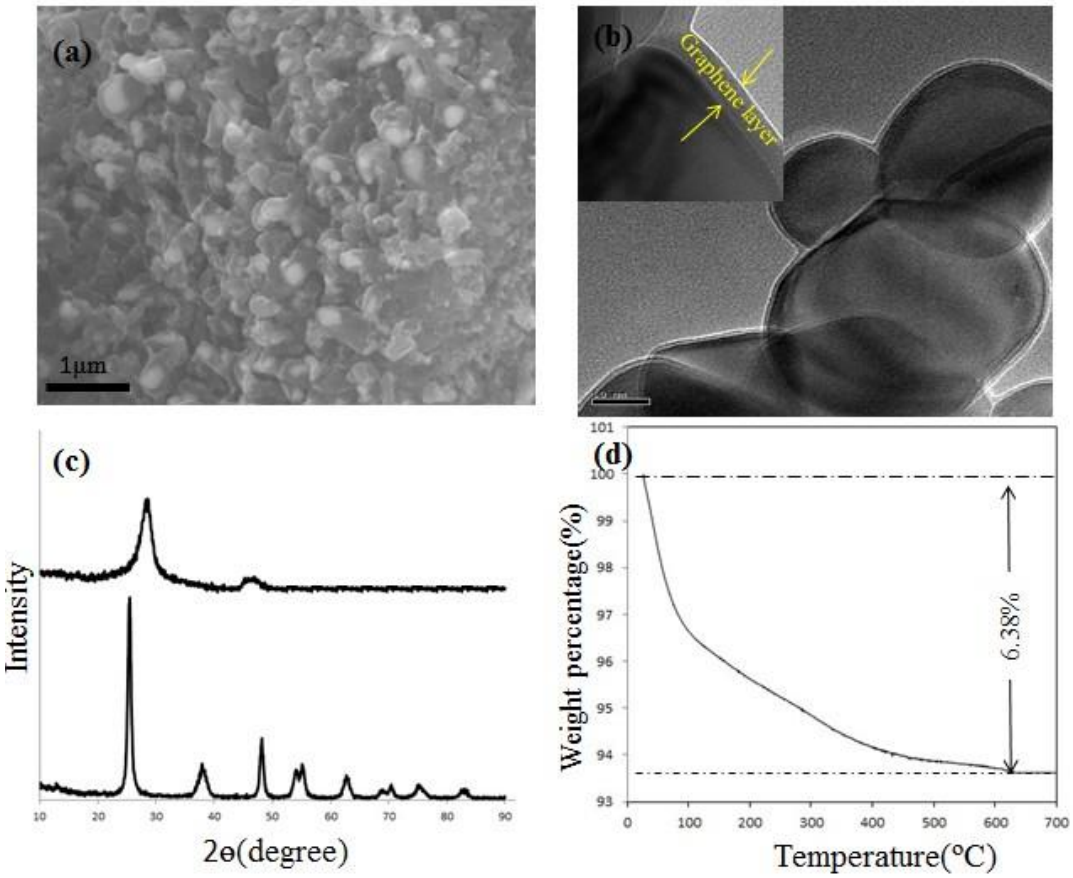


**Figure 5**: (a) SEM image of graphene encapsulated $TiO_2$ NPs; (b) TEM image of graphene encapsulated $TiO_2$ NPs (c) XRD pattern of graphene encapsulated $TiO_2$ NPs; (d) TGA result of graphene encapsulated $TiO_2$ NPs

Cyclic voltammetry(CV) experiments were conducted to test the electrochemical performance of bare $TiO_2$ NPs and $TiO_2$/graphene composite at a scan rate of 0.5mV/s within a voltage range of 1~3V (Figure 6). Both Figure 6(a) and (b)

demonstrated the similar profiles, which are consistent with the previous studies[72]. A cathodic peak at ~1.7V and an anodic peak at~2.1V were identified. Obvious change in amplitude and peak positions during subsequent cycles were observed on bare $TiO_2$ NP samples, while there was little significant change for graphene encapsulated $TiO_2$ NPs, which implies that $TiO_2$/graphene composite has higher reversibility than that of $TiO_2$ NPs[73]. Subsequent charging-discharging tests confirmed this improved reversibility.

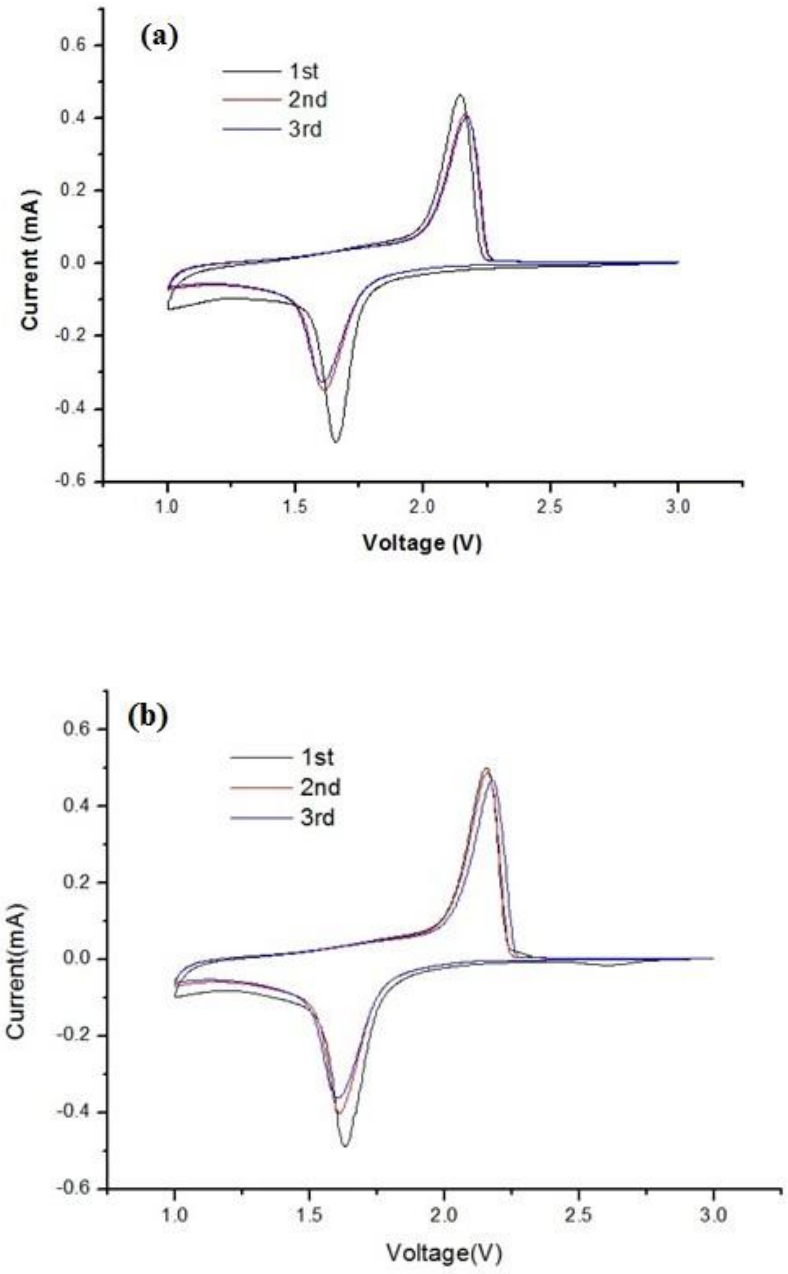


**Figure 6**: Cyclic voltammograms of (a) bare $TiO_2$ and (b) $TiO_2$/graphene electrodes

Figure 7(a) and (b) show the charging and discharging profile of bare $TiO_2$

NPs and $TiO_2$/graphene at 1C current rate, respectively. Both processes had the typical three stages[52]: first the voltage dropped rapidly from 3V, followed by a plateau at ~1.7V, indicating insertion of lithium ions; and a slow voltage decrease in the last stage, which signifies a transporting process of Li-ions to the anode surface[74].

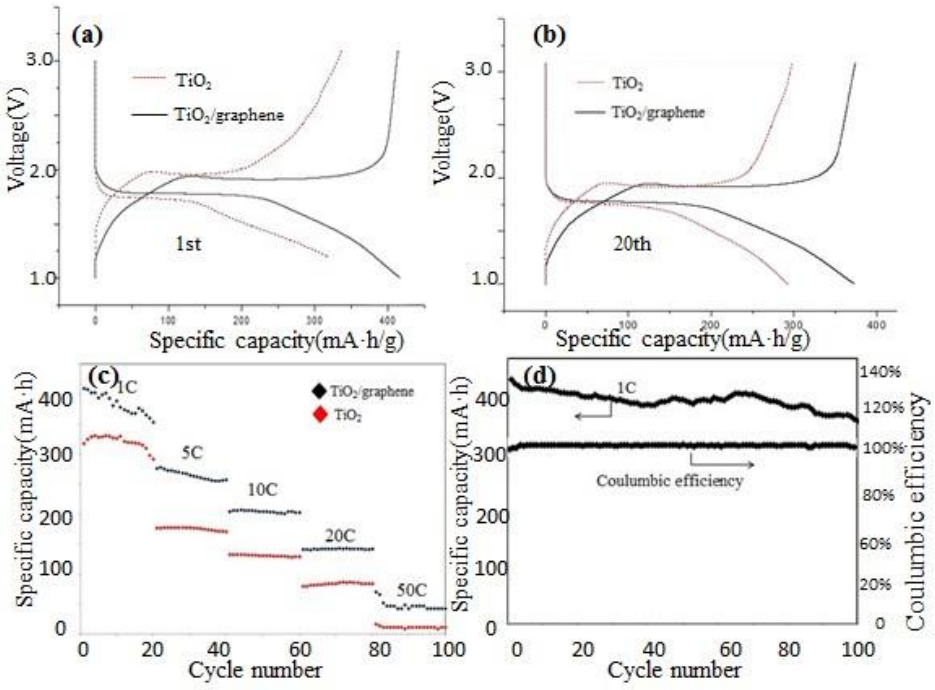


**Figure 7:** Charging and discharging profile at 1C current rate for bare $TiO_2$ NPs and $TiO_2$/graphene composite at (a) 1st cycle and (b) 20th cycle; (c)specific capacity of bare $TiO_2$ and $TiO_2$/graphene composite at different charging and discharging rates.

Batteries with both bare $TiO_2$ and $TiO_2$/graphene composites as anode materials underwent cycling test at 5 different charging and discharging rates-1C, 5C, 10C, 20C and 50C, respectively (Figure 7(c)). For bare anatase $TiO_2$ NPs, the specific capacity at 1C reached around 318mAh/g, which is almost the theoretical capacity of anatase $TiO_2$. This high capacity can be attributed to the nano size of $TiO_2$, which strongly facilitated Lithium insertion and extraction process. However, the capacity of $TiO_2$ NPs faded rapidly and continuously with the increase of cycling numbers and charging and discharging rate. At 20C, the specific capacity was only around 84mAh/g. This is due to the typical poor conductivity and volume change of most metal oxide anodes. At 1C, the $TiO_2$/graphene composite demonstrated an initial capacity of 409mA ħ/g and a reversible capacity of ~373mA ħ/g at 20 cycles, which was higher than that of $TiO_2$ NPs with an initial capacity of 318mA ħ/g and a reversible capacity of 291mA ħ/g at 20 cycles. This large capacity in $TiO_2$/GNS can

be attributed at least partially to the existence of graphene. As we know, graphene can also serve as a source for lithium storage with an experimental capacity of 1000mA ħ/g[75]. If we use the TGA data and the theoretical capacities of $TiO_2$ NPs and GNS (equation (2)), we can estimate the capacity of the composite to be around 376mA ħ/g, which agrees well with our experimental data on reversible capacity.

$TiO_2$/GNS capacity= $TiO_2$ capacity*$TiO_2$%+GNS capacity*GNS% (2)

At 20C, the capacity of $TiO_2$/GNS composite was retained at 141mA ħ/g. which is comparable to reported reversible capacity of $TiO_2$ /GNS composites (150~160mA ħ/g) at 1C current rate[47, 52, 73, 74, 76, 77]. Furthermore, even under very large charging and discharging rate of 50C, the specific capacity of $TiO_2$/GNS was ~51mA ħ/g, almost 5 times of that of bare $TiO_2$ NPs (~11mA ħ/g). The observed improvement is believed to be due to the improved conductivity, less agglomeration of $TiO_2$ NPs because of the encapsulation and improved accommodation of volume change of $TiO_2$ NPs. Figure 7(d) depicted long term cycling performance of $TiO_2$/graphene composite at 1C. The result showed that even after 100 cycles under 1C current rate, the specific capacity still remained at 343mA ħ/g, and the Coulumbic efficiency stayed above 98% up to 100 cycles.

## 4. Conclusion

In summary, we successfully synthesized GNS encapsulated $TiO_2$ composite and studied its use as an anode material for LIBs. Uniform, conformal and ultrathin graphene coating on individual nanoparticles were clearly identified and was believed to contribute to the improved electrochemical performance of the nanocomposite. Compared with the bare counterpart, electrochemical tests showed improved reversible specific capacity of $TiO_2$/graphene composite at 1C rate (373mA ħ/g) over bare $TiO_2$ NPs (291mA ħ/g). Even at fast charging and discharging rate of 20C, a capacity of 141mA ħ/g for $TiO_2$/GNS was retained. The long term tests showed that reversible capacity of $TiO_2$/GNS maintained at 343mA ħ/g (1C rate) after 100 cycles and Coulumbic efficiency stayed beyond 98%.

# References

1. Wu, Q. L.; Li, J.; Deshpande, R. D.; Subramanian, N.; Rankin, S. E.; Yang, F.; Cheng, Y.-T. *The Journal of Physical Chemistry C* **2012,** 116, (35), 18669-18677.
2. Mitra, S.; Poizot, P.; Finke, A.; Tarascon, J. M. *Advanced Functional Materials* **2006,** 16, (17), 2281-2287.
3. Lee, G.-H.; Park, J.-G.; Sung, Y.-M.; Chung, K. Y.; Cho, W. I.; Kim, D.-W. *Nanotechnology* **2009,** 20, (29), 295205.
4. Yuan, S.; Li, J.; Yang, L.; Su, L.; Liu, L.; Zhou, Z. *ACS applied materials & interfaces* **2011,** 3, (3), 705-709.
5. Kavan, L.; Kalbac, M.; Zukalová, M.; Exnar, I.; Lorenzen, V.; Nesper, R.; Graetzel, M. *Chemistry of Materials* **2004,** 16, (3), 477-485.
6. Wagemaker, M.; Kentgens, A.; Mulder, F. *Nature* **2002,** 418, (6896), 397-399.
7. Li, W.-Y.; Xu, L.-N.; Chen, J. *Advanced Functional Materials* **2005,** 15, (5), 851-857.
8. Li, Y.; Tan, B.; Wu, Y. *Nano Letters* **2008,** 8, (1), 265-270.
9. Shaju, K. M.; Jiao, F.; Débart, A.; Bruce, P. G. *Phys. Chem. Chem. Phys.* **2007,** 9, (15), 1837-1842.
10. Brousse, T.; Retoux, R.; Herterich, U.; Schleich, D. *Journal of The Electrochemical Society* **1998,** 145, (1), 1-4.
11. Lou, X. W.; Wang, Y.; Yuan, C.; Lee, J. Y.; Archer, L. A. *Advanced Materials* **2006,** 18, (17), 2325-2329.
12. Park, M. S.; Wang, G. X.; Kang, Y. M.; Wexler, D.; Dou, S. X.; Liu, H. K. *Angewandte Chemie* **2006,** 119, (5), 764-767.
13. Wu, Z.-S.; Zhou, G.; Yin, L.-C.; Ren, W.; Li, F.; Cheng, H.-M. *Nano Energy* **2012,** 1, (1), 107-131.
14. Reddy, M.; Subba Rao, G.; Chowdari, B. *Chemical Reviews* **2013**.
15. Reddy, M.; Rao, G. S.; Chowdari, B. *Chemical Reviews* **2012**.
16. Chen, J. S.; Wang, Z.; Dong, X. C.; Chen, P.; Lou, X. W. *Nanoscale* **2011,** 3, (5), 2158-61.
17. Kubiak, P.; Fröschl, T.; Hüsing, N.; Hörmann, U.; Kaiser, U.; Schiller, R.; Weiss, C. K.; Landfester, K.; Wohlfahrt‐Mehrens, M. *Small* **2011,** 7, (12), 1690-1696.
18. Wei, Z.; Liu, Z.; Jiang, R.; Bian, C.; Huang, T.; Yu, A. *Journal of Solid State Electrochemistry* **2010,** 14, (6), 1045-1050.
19. Kim, H. S.; Kang, S. H.; Chung, Y. H.; Sung, Y.-E. *Electrochemical and solid-state letters* **2010,** 13, (2), A15-A18.
20. He, G.; Eckert, J.; Löser, W.; Schultz, L. *Nature materials* **2002,** 2, (1), 33-37.
21. Lin, Y.; Wu, G.; Yuan, X.; Xie, T.; Zhang, L. *Journal of Physics: Condensed Matter* **2003,** 15, (17), 2917.
22. Testino, A.; Bellobono, I. R.; Buscaglia, V.; Canevali, C.; D'Arienzo, M.; Polizzi, S.; Scotti, R.; Morazzoni, F. *Journal of the American Chemical Society* **2007,** 129, (12), 3564-3575.
23. Yin, H.; Wada, Y.; Kitamura, T.; Kambe, S.; Murasawa, S.; Mori, H.; Sakata, T.; Yanagida, S. *Journal of Materials Chemistry* **2001,** 11, (6), 1694-1703.
24. Stergiopoulos, T.; Arabatzis, I. M.; Katsaros, G.; Falaras, P. *Nano Letters* **2002,** 2, (11), 1259-1261.

25. Qiu, J.; Yu, W.; Gao, X.; Li, X. *Nanotechnology* **2007,** 18, (29), 295604.
26. Zhong, P.; Que, W. *Nano-Micro Letters* **2010,** 2, (1), 1-5.
27. Fröschl, T.; Hörmann, U.; Kubiak, P.; Kučerová, G.; Pfanzelt, M.; Weiss, C.; Behm, R.; Hüsing, N.; Kaiser, U.; Landfester, K. *Chemical Society Reviews* **2012,** 41, (15), 5313-5360.
28. Jung, H.-G.; Oh, S. W.; Ce, J.; Jayaprakash, N.; Sun, Y.-K. *Electrochemistry Communications* **2009,** 11, (4), 756-759.
29. Yang, S.; Feng, X.; Müllen, K. *Advanced Materials* **2011,** 23, (31), 3575-3579.
30. Liu, S.; Yu, J.; Jaroniec, M. *Journal of the American Chemical Society* **2010,** 132, (34), 11914-11916.
31. Zhu, P.; Wu, Y.; Reddy, M.; Nair, A. S.; Chowdari, B.; Ramakrishna, S. *RSC Advances* **2012,** 2, (2), 531-537.
32. Sasidharan, M.; Nakashima, K.; Gunawardhana, N.; Yokoi, T.; Inoue, M.; Yusa, S.-i.; Yoshio, M.; Tatsumi, T. *Chemical Communications* **2011,** 47, (24), 6921-6923.
33. Zhang, J.-J.; Wei, Z.; Huang, T.; Liu, Z.-L.; Yu, A.-S. *Journal of Materials Chemistry A* **2013,** 1, (25), 7360-7369.
34. Lee, J. Y.; Zhang, R.; Liu, Z. *Electrochemical and solid-state letters* **2000,** 3, (4), 167-170.
35. Read, J.; Foster, D.; Wolfenstine, J.; Behl, W. *Journal of power sources* **2001,** 96, (2), 277-281.
36. Wang, L.; Yu, Y.; Chen, P.; Zhang, D.; Chen, C. *Journal of power sources* **2008,** 183, (2), 717-723.
37. Liang, M.; Zhi, L. *Journal of Materials Chemistry* **2009,** 19, (33), 5871-5878.
38. Park, S.; Ruoff, R. S. *Nature nanotechnology* **2009,** 4, (4), 217-224.
39. Lee, C.; Wei, X.; Kysar, J. W.; Hone, J. *Science* **2008,** 321, (5887), 385-388.
40. Wu, Z.-S.; Ren, W.; Gao, L.; Zhao, J.; Chen, Z.; Liu, B.; Tang, D.; Yu, B.; Jiang, C.; Cheng, H.-M. *ACS Nano* **2009,** 3, (2), 411-417.
41. Balandin, A. A.; Ghosh, S.; Bao, W.; Calizo, I.; Teweldebrhan, D.; Miao, F.; Lau, C. N. *Nano Letters* **2008,** 8, (3), 902-907.
42. Rao, C. N. R.; Sood, A. K.; Subrahmanyam, K. S.; Govindaraj, A. *Angewandte Chemie International Edition* **2009,** 48, (42), 7752-7777.
43. Pan, D.; Wang, S.; Zhao, B.; Wu, M.; Zhang, H.; Wang, Y.; Jiao, Z. *Chemistry of Materials* **2009,** 21, (14), 3136-3142.
44. Guo, P.; Song, H.; Chen, X. *Electrochemistry Communications* **2009,** 11, (6), 1320-1324.
45. Kim, H.; Kim, S.-W.; Park, Y.-U.; Gwon, H.; Seo, D.-H.; Kim, Y.; Kang, K. *Nano Research* **2010,** 3, (11), 813-821.
46. Yao, J.; Shen, X.; Wang, B.; Liu, H.; Wang, G. *Electrochemistry Communications* **2009,** 11, (10), 1849-1852.
47. Wang, D.; Choi, D.; Li, J.; Yang, Z.; Nie, Z.; Kou, R.; Hu, D.; Wang, C.; Saraf, L. V.; Zhang, J. *ACS Nano* **2009,** 3, (4), 907-914.
48. Behera, S. K. *Chemical Communications* **2011,** 47, (37), 10371-10373.
49. Li, X.; Huang, X.; Liu, D.; Wang, X.; Song, S.; Zhou, L.; Zhang, H. *The Journal of Physical Chemistry C* **2011,** 115, (44), 21567-21573.

50. Chen, S. Q.; Wang, Y. *Journal of Materials Chemistry* **2010,** 20, (43), 9735-9739.
51. Lian, P.; Zhu, X.; Xiang, H.; Li, Z.; Yang, W.; Wang, H. *Electrochimica acta* **2010,** 56, (2), 834-840.
52. Chen, J. S.; Wang, Z.; Dong, X. C.; Chen, P.; Lou, X. W. D. *Nanoscale* **2011,** 3, (5), 2158-2161.
53. Koelsch, M.; Cassaignon, S.; Guillemoles, J.; Jolivet, J. *Thin Solid Films* **2002,** 403, 312-319.
54. Daniela C. Marcano, D. V. K., Jacob M. Berlin, Alexander Sinitskii, Zhengzong Sun, Alexander Slesarev, Lawrence B. Alemany, Wei Lu, and James M. Tour. *ACS Nano* **2010,** 4, (8), 4806-4814
55. Marcano, D. C.; Kosynkin, D. V.; Berlin, J. M.; Sinitskii, A.; Sun, Z.; Slesarev, A.; Alemany, L. B.; Lu, W.; Tour, J. M. *ACS Nano* **2010,** 4, (8), 4806-4814.
56. Yang, Z.; Choi, D.; Kerisit, S.; Rosso, K. M.; Wang, D.; Zhang, J.; Graff, G.; Liu, J. *Journal of power sources* **2009,** 192, (2), 588-598.
57. Van Overschelde, O.; Snyders, R.; Wautelet, M. *Applied Surface Science* **2007,** 254, (4), 971-974.
58. Gao, Y.; Masuda, Y.; Seo, W.-S.; Ohta, H.; Koumoto, K. *Ceramics International* **2004,** 30, (7), 1365-1368.
59. http://rsbweb.nih.gov/ij/.
60. Shin, J. Y.; Samuelis, D.; Maier, J. *Advanced Functional Materials* **2011,** 21, (18), 3464-3472.
61. Subramanian, V.; Karki, A.; Gnanasekar, K.; Eddy, F. P.; Rambabu, B. *Journal of power sources* **2006,** 159, (1), 186-192.
62. Macwan, D.; Dave, P. N.; Chaturvedi, S. *Journal of materials science* **2011,** 46, (11), 3669-3686.
63. Oh, S. W.; Park, S.-H.; Sun, Y.-K. *Journal of power sources* **2006,** 161, (2), 1314-1318.
64. Fröschl, T.; Hoermann, U.; Kubiak, P.; Kučerová, G.; Pfanzelt, M.; Weiss, C.; Behm, R.; Hüsing, N.; Kaiser, U.; Landfester, K. *Chemical Society Reviews* **2012,** 41, (15), 5313-5360.
65. Rossmanith, R.; Weiss, C. K.; Geserick, J.; Hüsing, N.; Hörmann, U.; Kaiser, U.; Landfester, K. *Chemistry of Materials* **2008,** 20, (18), 5768-5780.
66. Li, D.; Müller, M. B.; Gilje, S.; Kaner, R. B.; Wallace, G. G. *Nature nanotechnology* **2008,** 3, (2), 101-105.
67. Feng, B.; Hong, R.; Wang, L.; Guo, L.; Li, H.; Ding, J.; Zheng, Y.; Wei, D. *Colloids and Surfaces A: Physicochemical and Engineering Aspects* **2008,** 328, (1), 52-59.
68. Han, S.; Wu, D.; Li, S.; Zhang, F.; Feng, X. *Small* **2013**.
69. Su, F.-Y.; You, C.; He, Y.-B.; Lv, W.; Cui, W.; Jin, F.; Li, B.; Yang, Q.-H.; Kang, F. *Journal of Materials Chemistry* **2010,** 20, (43), 9644-9650.
70. Su, F.-Y.; He, Y.-B.; Li, B.; Chen, X.-C.; You, C.-H.; Wei, W.; Lv, W.; Yang, Q.-H.; Kang, F. *Nano Energy* **2012,** 1, (3), 429-439.
71. Chen, M.; Huang, Z.; Wu, G.; Zhu, G.; You, J.; Lin, Z. *Materials research bulletin* **2003,** 38, (5), 831-836.

72. Zhang, F.; Zhang, Y.; Song, S.; Zhang, H. *Journal of power sources* **2011,** 196, (20), 8618-8624.
73. Cai, D.; Lian, P.; Zhu, X.; Liang, S.; Yang, W.; Wang, H. *Electrochimica acta* **2012,** 74, (0), 65-72.
74. Ding, S.; Chen, J. S.; Luan, D.; Boey, F. Y. C.; Madhavi, S.; Lou, X. W. D. *Chemical Communications* **2011,** 47, (20), 5780-5782.
75. Wang, G.; Shen, X.; Yao, J.; Park, J. *Carbon* **2009,** 47, (8), 2049-2053.
76. Li, N.; Liu, G.; Zhen, C.; Li, F.; Zhang, L.; Cheng, H. M. *Advanced Functional Materials* **2011,** 21, (9), 1717-1722.
77. He, L.; Ma, R.; Du, N.; Ren, J.; Wong, T.; Li, Y.; Lee, S. T. *Journal of Materials Chemistry* **2012,** 22, (36), 19061-19066.

# CHAPTER 4: CONCLUSIONS AND FUTURE WORK

This thesis presents a series of experimental investigations on synthesis, optimization, integration and characterization of carbon nanostructured materials. We developed a cost effective post treatment routine to obtain free-standing CNTs grown by template-assisted chemical vapor deposition(CCVD) method, synthesized graphite oxide (GO) and graphene nanosheets(GNS) under mild reaction conditions and finally designed and studied a novel $TiO_2$ NPs/GNS core-shell structure for applications in Lithium-ion batteries. Corresponding to the objectives in Chapter 1, the following conclusions were drawn. Future work was also exploited in the end of this chapter.

1. By a two-step method to anodize aluminum, we successfully fabricated alumina thin film with uniform and straight nano pores. After the electro deposition of cobalt nano particles within the pores, CCVD method was used to synthesize CNTs [Paper 1#]. An effective two-step post treatment method has been successfully developed to remove the amorphous carbon and expose free-standing CNT arrays. This method based on mechanical polishing combined with a wet etching is proven to be a highly efficient post treatment compared with other conventional methods including air oxidation and reactive ion etching. The as-made samples have been used for studying mechanical properties of CNT based composites [Appendix 1# and 2#].
2. By oxidation of natural graphite flakes to synthesize graphite oxide (GO) followed by reduction, we developed an optimized protocol to fabricate GNS for diverse applications [Paper 2#]. This environmental friendly, highly effective and low cost routine provides GNS with high quality in a controllable fashion.
3. The electrostatic interaction was successfully employed as a facile process to synthesize $TiO_2$ NPs/GNS core-shell structure with enhanced performance as anode materials for LIB applications [Paper 3#]. Uniform and conformal wrapping of GNS around $TiO_2$ NPs was observed and identified as the key contributor to the enhanced electrochemical performance. Compared with other reported $TiO_2$ nanostructured materials, the graphene encapsulated $TiO_2$ NPs demonstrated a very high initial capacity of 409mA ħ/g at 1C and exhibited little decay during subsequent cycles. Besides, the composite retained a capacity of 141mA ħ/g at the high charging/discharging rate of 20C, which is comparable to reported reversible capacity of $TiO_2$/GNS composites (150~160mA ħ/g) at 1C current rate. The nanocomposite

anode also showed a Coulombic efficiency above 98% and good long term cycling performance (as high as 343mAh/g after 100 cycles) at a rate of 1C.

Possible future work may continue broadening of the integration of GNS and their derivatives (such as GO) into different nanostructured functional materials to form GNS based composites for various energetic applications. As demonstrated in [paper 3#], the encapsulation structure is proven to be promising for advanced electrodes with greatly improved electrochemical performance. Besides, static electric interaction has shown convincing potential in self-assembling process. Possible projects may include:

1. ***$Fe_3O_4$ NPs/graphene composite for LIB applications***: $Fe_3O_4$ is another interesting anode material for LIB applications. In our preliminary lab work, we already synthesized $Fe_3O_4$-$NH_2$ NPs, which were positively charged. Therefore, next step is to encapsulate the $Fe_3O_4$ NPs with negatively charged GO. Followed by reduction step, $Fe_3O_4$/GNS composite can be made for further characterizations.

2. ***In-situ hydrothermal method to synthesize α-MnO2/graphene composite as catalyst for Lithium air batteries***: Lithium-air battery is another interesting and promising energetic device. In our lab work, we have successfully synthesized single-crystalline α-$MnO_2$ tetragonal nanotubes as the catalyst for Lithium-air batteries by a facile hydrothermal method. Since GO can also be reduced into GNS by hydrothermal method, we are proposing an in-situ method to synthesize α-$MnO_2$/GNS composite to improve the electrochemical performance.

# APPENDICES

## Appendix 1: Measurement of Interfacial Energy and Friction between Carbon Nanotubes and Polymer Matrix by a Micro-pullout Test


## Abstract

The remarkable mechanical and electronic properties and large surface area of carbon nanotube make it an excellent candidate for energy and environment applications such as solar cells, fuel cells, batteries, and composite structures for windmill blades. One of issues that determine the useful life and hence reliability of the energy devices and structures is the interface between the nanotube and matrix/current collector that the nanotube embedded in. Here, we developed a simple method to quantitatively measure the interfacial strength of nanotube/matrix interfaces. Instead of nanoscale measurement which requires nanomanipulation, a micro-pillar was imprinted onto a composite surface on which nanotubes stick out with a given protruding length. The polymer pillar was then pulled out from the surface, and the maximum force was measured, based on which interfacial energy was calculated by finite element methods and analysis formula. The results show that the interfacial friction stress between nanotube and polymer matrix is in the range of 36-51 MPa, which is consistent with the measurement by other methods.



**Key words:** Carbon nanotube, Composites; Interface, Finite element analysis, Pullout.


### 1. Introduction

Carbon nanotubes (CNTs) are molecular-scale tubes of graphitic carbon with outstanding mechanical properties, remarkable electronic properties and many other unique characteristics [1-4]. These materials are excellent candidates for a wide range of energy and environment applications, including nanotube electrodes in solar cells, fuel cells and high-energy batteries, media for $H_2$ storage at room temperature, and composite materials for windmill blades.[5-10] It has been shown that vertically-aligned *nitrogen-doped* CNT arrays can act as a metal-free electrode with a

much better electrocatalytic activity, long-term operation stability, and tolerance to crossover effect than platinum for oxygen reduction in alkaline fuel cells [8]. Using carbon nanotubes for battery's electrodes can produce a significant increase -- up to tenfold -- in the amount of power it could deliver from a given weight of material, compared to a conventional lithium-ion battery [11]. Carbon nanofibers already compete with traditional technologies for electrodes in batteries; currently 50% of all lithium batteries incorporate carbon nanofibers which double their energy capacity. In structured materials application, the carbon nanotube/carbon fabric/epoxy composites showed ~30% enhancement of the interlaminar shear strength as compared to that of carbon fiber/epoxy composites without carbon nanotubes and demonstrate significantly improved out-of-plane electrical conductivity [12].

One of the important issues in the energy applications of carbon nanotubes is the interface between the CNT and matrix. For solar cell, fuel cell and battery applications, repetitive cycling can weaken the CNT electrode structure reducing its adhesion to the current collector causing the cell to swell. This can lead to reduction in charge capacity and ultimately failure of the cell [13]. For composites, the interfacial strength strongly affects the mechanical properties, and therefore useful life of the composite structures [14]. Quantitatively measurement of interfacial strength between CNT and matrix in various applications is thus important to ensure the life and hence reliability of those energy devices and structures.

Because of importance of the interface, efforts have been made to quantitatively measure interfacial strength of the composites. A few experiments on polymer nanocomposites have been performed with nano-manipulation techniques for probing individual carbon nanotube (CNT) pullout from a polymer matrix [15-17]. However, quantitatively measuring the interfacial friction presents severe challenges mainly due to the manipulation, gripping and force and strain measurements at the nanoscale.

In the present work, we developed a simple method to measure the interfacial friction between CNTs and polymer matrix. Instead of measure the nano-newton force using nano-manipulation, we prepared micro-scale polymer pillars and imprinted them onto the surfaces of CNT arrays. The fractural energy due to nanotube pullout from the matrix was determined by measuring the maximum load during peeling process. The friction and bonding strength of CNT/polymer interface was then be calculated based on finite element analysis.

## 2. Experimental procedure

### a) Sample preparation

Vertically-aligned multi-walled carbon nanotubes (MWCNT) grown by chemical vapor deposition (CVD) technique was embedded in alumina templates [18]. Briefly, high-purity aluminum is anodized in a multistep process to generate a nanoporous alumina matrix with a hexagonal array of straight pores extending from the substrate to the matrix surface. CNTs were then grown inside those nanopores using a chemical vapor deposition (CVD) method. The diameter of the resulting MWCNT arrays is 50 nm and the volume fraction of the CNTs on the substrate is 0.3. The nanotubes were then partially exposed by etching the alumina matrix to desire depth (Fig.1d). Here the samples with 0 nm, 30 nm and 50 nm protruding length were investigated. Imprinting materials used in this study is Polymethylmethacrylate (PMMA, 0.75mm thick Goodfellow). A Leica ultra-microtome was used to carefully cut thin PMMA plate into Trapezoid pillars with a dimension from 16*16 μm-150*150 μm at one end having a contact area S.

### b) Pull-out test

Pullout testing was performed with a home-made micro-testing system (Fig.1a), consisting of a lower sample holder with a heater, and an upper sample holder attached on a high-precise XYZ stage (Throlabs model MTS25/M) with a resolution of 0.1 μm/s and a minimum velocity of 0.2 μm/s. A load cell (Futek, model: WC1) with a resolution of 1mN was attached on the upper sample holder. During the operation, the displacement and force on samples were simultaneously recorded by a computer. A long distance microscopy (U-eye model: MD1900) was set to observe and record images of the contact zone between the PMMA pillar and CNT array.

Before testing, a composite sample with highly-ordered CNT array was fixed on the top of the lower holder while the PMMA pillar was firmly glued on the load cell by superglue. The CNT sample was gradually heated up to 165 ℃ while the PMMA pillar was kept at room temperature. After the CNT sample reached the constant temperature, controlled by the XYZ stage, the PMMA pillar was imprinted onto the surface of the CNT sample surface and the imprinting process maintained under a constant compressive loading for three minutes. The operation in this process should be careful as excessive push of the polymer into the composite sample would

cause the local bucking of pillars. After the processing, the system was cooled down while keeping compressive force on the pillar to make sure the polymer pillar is still embedded within the CNT array. After the system was completely down to the room temperature, the XYZ stage pulled the PMMA pillar up at a speed of 0.2μm/s under the control of computer. The force-displacement curve was recorded and the maximum separation force can then be determined precisely. Finally, the contact area on the polymer surface (Fig.1c) was measured under optical microscope (U-eye model: MD1900) and scanning electron microscopy (SEM) (Jeol 7000). The contact surfaces of composite samples and PMMA pillar were also examined after the separation.

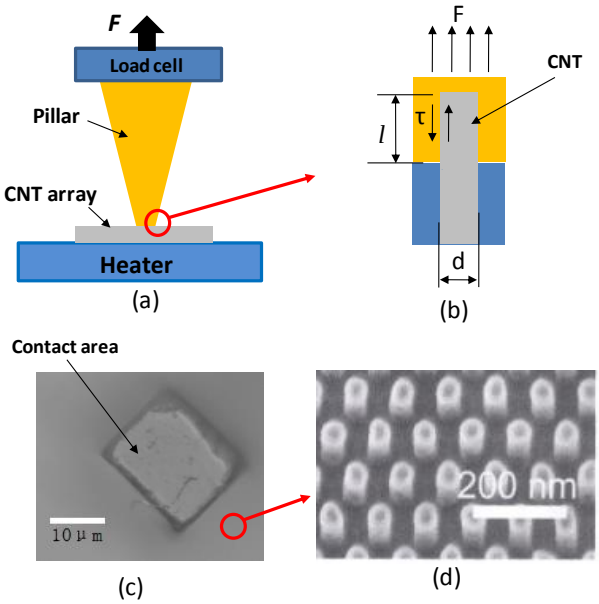


**Fig.1.** (a) Experiment set-up for pullout test using micro-pillar and CNT array, (b) Cross-section (unit cell) of pillar/CNT interface, showing CNT embedded in PMMA matrix, (c) Optical image of top view of PMMA pillar/CNT contact area after the pillar was pulled out from the surface, and (d) SEM image of CNT array after alumina matrix was etched.

## 3. Finite element modeling

Finite element (FE) models were developed to simulate the pulling and separation process of micropillars from composite samples. The models have exactly the same configuration as those samples used in the experiment. Finite element software package (Abaqus 6.8-2) was used to perform the simulation of pillar pullout processing. The FE models consist of three parts: a micropillar, a substrate and a cohesive zone between them, representing PMMA pillar, CNT composite substrate and PMMA/CNT interface, respectively, as schematically shown in Fig. 2a and b. Specifically, adhesion and friction behaviors of CNT array at the PMMA/CNT

interface were treated as the fracture resistance of a cohesive layer. Thus, a cohesive zone model was adopted to simulate the interactions between the vertical distributed CNTs and PMMA. This cohesive zone features distinct traction-separation relations as a crack initiates at one edge and propagates throughout the whole surface. In the simulation, bilinear traction-separation laws were employed.

$$T_n = \frac{T_n^0}{\delta_n^0}\delta_n \text{ when } 0 \le \delta_n \le \delta_n^0 \quad (1)$$

$$T_n = \frac{T_n^0}{\delta_n^f - \delta_n^0}(\delta_n^f - \delta_n) \text{when } \delta_n^0 < \delta_n \le \delta_n^f \quad (2)$$

where $T_n$ is the normal traction separation stress and $\delta_n$ is normal displacement at failure, $T_n^0$ is the normal cohesive strength, $\delta_n^0$ is the normal displacement jump between two cohesive surfaces when damage initiates, and $\delta_n^f$ is the normal displacement jump when separation completes. The traction−separation response in shearing direction takes the same form as Eqs. 1 and 2, except for the subscripts being changed from *n* to *s*. The parameters used in the calculation are listed in Table 1. By adjusting the parameters we could calculate the maximum force and fit the experimental results with an error of ±1%. The interfacial energy $G_{IC}$ was then calculated by

$$G_{Ic} = \frac{T_n * \delta_n^f}{2} \quad (3)$$

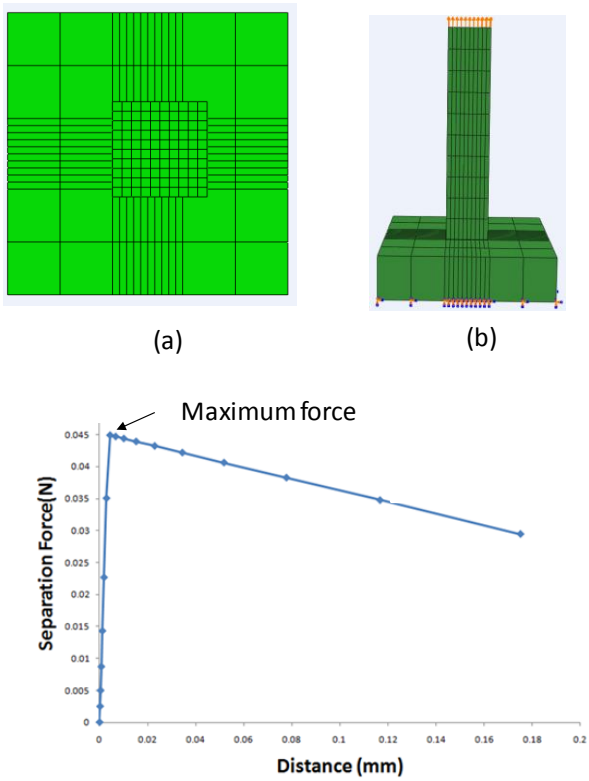


**Fig.2.** (a) Top-view and (b) Side-view of FE models, and (c) A separation force－distance curve simulated by FE analysis.

**Table I** Parameters used for CNT/ PMMA adhesion model

| PMMA Young's Modulous E(MPa) | Al Young's Modulous $E_2$(MPa) | Traction separation stress T(MPa) | Separation length $_f$(mm) |
|---|---|---|---|
| 3200 | 90000 | 0.012-0.017 | 0.06 |

The final FE model contains about 35,000 nodes and 30,000 elements with very fine meshes in the contact region between CNT composite and PMMA pillar. The final mesh density was determined through a series of convergence studies. The cohesive zone areas in the FE simulation were chosen as 64 μm*64 μm, 81 μm*81 μm, 120 μm*120 μm, 135 μm*135 μm, and 180 μm*180 μm, which is the same as those used in the experiment. The height of the PMMA pillar was 1mm. The CNTs composites size was 1mm*1mm with the contact area in the center, the nodes of which at the bottom were constrained in all translational degrees of freedom.

## 4. Results and Discussion

A typical load-displacement curves with CNT and without CNT protruding under the same contact area S are shown in Fig. 3(a). After the initial loading of the specimen, a crack initiates at an edge of the specimen and propagate along the bonded

interface. Since the contact shape is square, when the edge-induced crack propagates, the specimen provides an increasing interfacial area with increasing crack length and load, and initially results in stable crack propagation. At some crack length the propagation becomes unstable and catastrophic failure of the sample occurs at the interface. This coincides with the point of maximum load in Fig. 3(a). It can be seen that with CNTs sticking out, the maximum force is much larger than that for the sample with flat surface (no CNT sticking out).

We have measured the maximum force under various interface contact conditions. By adjusting the contact area, we obtained a series of curves correlating the maximum separation force, $F_{max}$, to contact area S. Fig.3b shows the maximum separation force as a function of contact area. The maximum separation force almost linearly increases with increasing the contact area. This is not surprising because the force should be proportional to the area if the interfacial failure strength is contact.

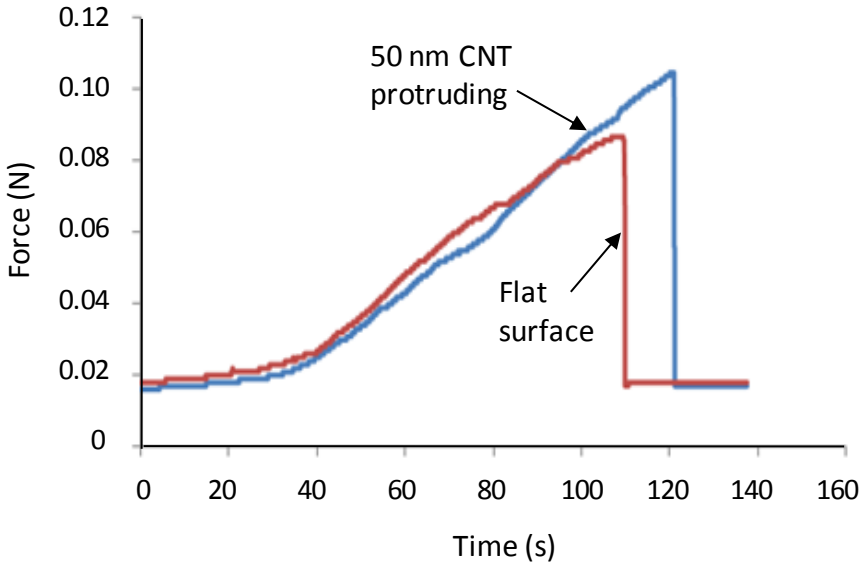


(a)

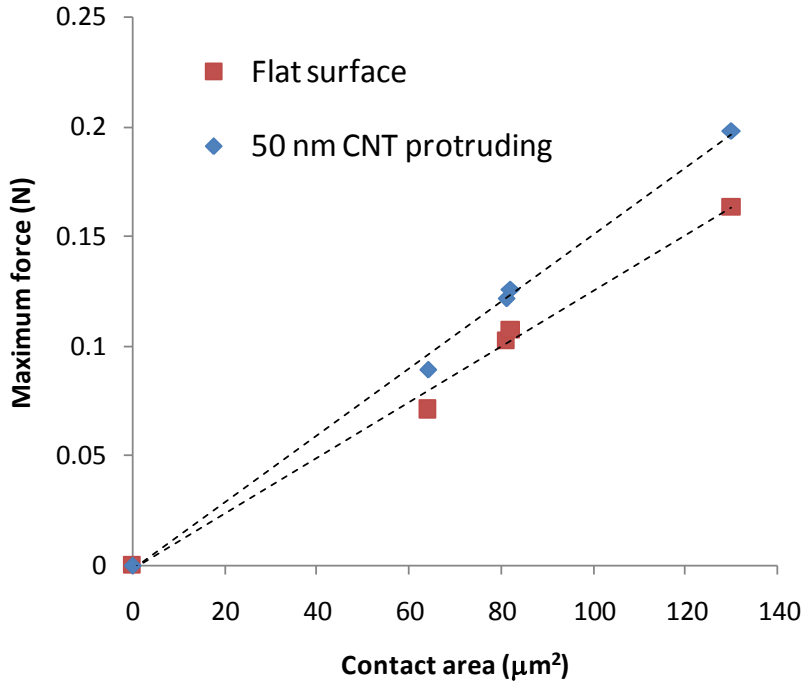


(b)

**Fig.3.** (a) A typical force-displacement curve during the separation process, and (b) Relationship between maximum pull out force and contact area for flat surface and CNT arrays with 50 nm CNT protruding.

The interfacial energy $G_{Ic}$ was calculated based on the FEA models and Eq. (3). Fig. 4 shows the interfacial energy $G_{Ic}$ under different substrate condition. The interfacial energy is nearly independent of the contact area, suggesting that it is determined by the substrate conditions or the protruding length of CNT array but not interfacial contact area. As shown in Fig. 4, the CNT protruding length strongly affects the surface energy of CNT/PMMA interface. The higher the protruding CNTs is, the larger the interfacial energy becomes.

The interfacial shear stress was calculated based on the experimental data and Eq.6a in Appendix. To estimate the interfacial stress, we first calculated the adhesion energy difference between the samples with/without CNT protruding, yielding $\Delta G_{Ic}$=0.054 J/m for 30nm CNT protruding length, and $\Delta G_{Ic}$=0.109 J/m for 50nm CNT protruding length. With $d$=50 nm, $V_f$=0.3 as input parameters in Eq.6a in Appendix, the interface stress $\tau$ is calculated in a range of 36-51MPa.

There have been reports on the interfacial friction stress of polymer/CNT interfaces. In particular, similar procedure but using single nanotube was developed to measure the interfacial strength. Barber *et al*. attached individual CNTs to the end of an atomic force microscopy (AFM) tip and pushed the nanotube into a liquid

copolymer, followed by solidification of the polymer, to produce single carbon nanotube composites [14]. The nanotube was then pulled from the polymer matrix and the critical force required for interfacial failure was recorded by the AFM. Their experiment gives a value of 47 MPa for the average interfacial stress required to remove a single MWCNT from the polyethylenebutene matrix. Interestingly, their measurement is very close to our results. Such value of interfacial strength is relatively larger than that (~10 MPa [19]) in traditional composite materials containing fiber reinforcements that only interact weakly with the surrounding polymer matrix. Thus, covalent bonding may exist between the polymer matrix and CNT, probably through defects in the outer shell of the nanotube itself [14]. This may be true to our material system since the CNTs fabricated by the template-assistant technique in this study have relatively rough surface [18]. Thus, strong mechanical interlock may also play an important role in enhancing the interfacial strength.

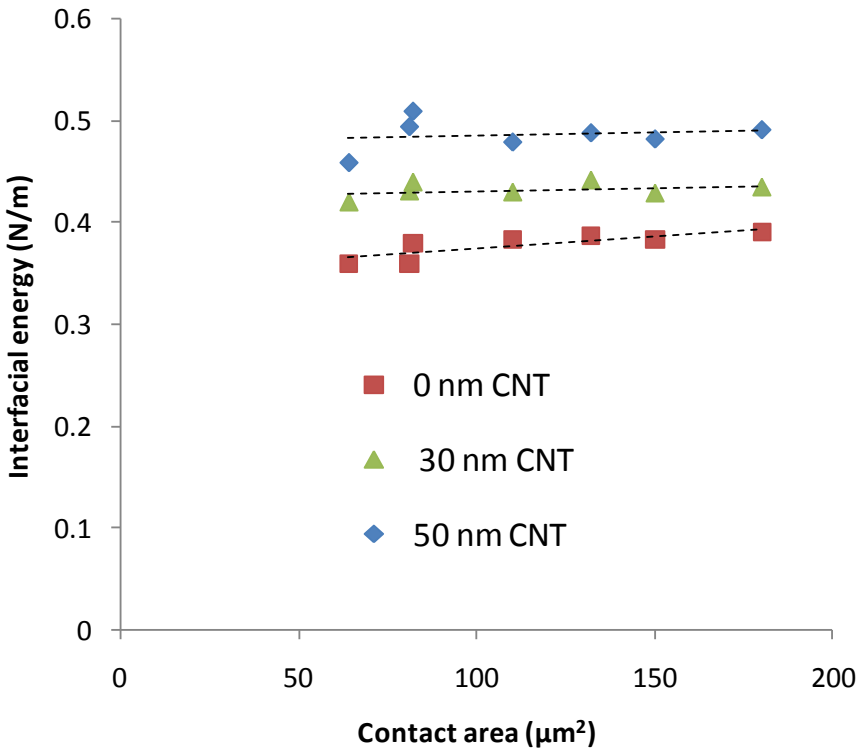


**Fig.4.** Interface energy $G_{Ic}$ with samples having different protrude CNTs.

## 5. Conclusions

A microscale pullout test method has been developed to evaluate the interfacial friction between the carbon nanotube and polymer matrix. The maximum force was measured using the micro-pullout test. To extract interfacial energy, a 3D finite element model for the micro-pullout test was developed and a cohesive zone model was used to predict the crack propagation and maximum force. The model predicts that the interfacial energy is a function of maximum separation force and CNTs height. The interfacial friction stress of CNT/PMMA interface was determined by fitting the experimental results. The measured interfacial shear stress ranges from 36 to 51 MPa, which is consistent with the results from other methods. Compared with nano-manipulation, this technique is simple and easy to perform, providing a new route for measuring the interfacial friction stress at the nanoscale.

**Acknowledgement**

The authors would like to thank the support by NSF under the contract # 0825990.

## Appendix: Determination of Interfacial friction between CNT and matrix

Fig. 1b shows a unit cell model where the interfacial friction is generated at CNT/matrix interfacial during pullout. In the unit cell model, the interface between the PMMA and CNT is assumed to have constant interfacial friction stress $\tau$. The maximum force to pull the CNT from the matrix is:

$$F = \tau(\pi dl) \tag{1a}$$

Assuming that the force changes linearly during pullout, the total work for CNT pullout is:

$$W = \frac{1}{2}Fl \tag{2a}$$

Substituting equation (1a) into equation (2a) we have

$$W = \frac{1}{2}\pi\tau d \tag{3a}$$

This work is only related to the friction between CNT and PMMA. During the pullout process, work must also be done to overcome the interfacial energy, $\gamma_1$ and $\gamma_2$ , so as to separate the PMMA/Alumina ($\gamma_1$)and PMMA/CNT($\gamma_2$) interfaces with contact area $A_1$ and $A_2$, respectively. So the total energy required is

$$W_{tot} = W + 2\gamma_1 A_1 + 2\gamma_2 A_2 = \frac{1}{2}\pi\tau dl^2 + 2\gamma_1 A_1 + 2\gamma_2 A_2 \tag{4a}$$

where $A_1$ is the contact area between PMMA and alumina, and $A_2$ is the contact area

between PMMA and CNT cross section. The interfacial fracture energy can be written as

$$G_{IC} = \frac{W_{tot}}{A} = \frac{2\tau}{d} = V_f l^2 + 2\gamma_1(1 - V_f) + 2\gamma_2 V_f \quad (5a)$$

where $V_f$ is the volume fraction of CNT and $A = A_1 + A_2$ is the total area of the CNT unit cell. If the CNTs are not embedded in the matrix, the interfacial fracture energy is $2\gamma_1(1 - V_f) + 2\gamma_2 V_f$. From (5a) we have

$$\tau = \frac{\Delta G_{Ic} d}{2V_f l^2} \quad (6a)$$

where $\Delta G_{Ic}$ is the interfacial fracture energy difference between samples with and without embedded CNTs in PMMA and can be measured separately by using micro-pullout test described above. Equation (6a) can then be used to estimate the interfacial stress for CNT composites.

**References**


1. M.M.J. Treacy, T.W. Ebbesen, J.M. Gibson. Nature 381, 678 **(1996)**.
2. P. Poncharal, Z.L. Wang, D. Ugrate, W.A. de Heer. Science 283, 1513 **(1999)**.
3. M. Bockrath, D. H. Cobden, J. Lu, A. G. Rinzler, R. Smalley, L. Balents, P. L. McEuen. Nature 397, 598 **(1999)**.
4. P. Kim, T.W. Odom, J.-L. Huang, C.M. Lieber. Phys. Rev. Lett. 82, 1225 **(1999)**.
5. Gao, B., A. Kelinhammes, X.P. Tang, C. bower, Y. Wu, O. Zhou. Chemical Physics Letters 307, 153 **(1999).**
6. C.Liu, Y.Y.Fan, M.Liu, H.T.Cong, H.M.Cheng, M.S.Dresselhaus. Science 286,1127 **(1999).**
7. M. W. Rowell, M. A. Topinka, and M. D. McGehee. Applied Physics Letters 88, 233506 **(2006).**
8. K.P. Gong, Feng Du, Z.H. Xia, M. Durstock and L.M. Dai.Science 323, 760 **(2009)**.
9. D. T. Welna, L. Qu, B. E. Taylor, L. Dai, M. F. Durstock. Journal of Power Sources 196, 1455 **(2011)**.
10. J. Suhr, L. Ci, V. Pushparaj, X. Zhang, P. M. Ajayan. Nano Letters 8, 2762 **(2008)**.
11. S. W. Lee, N. Yabuuchi, B. M. Gallant, S. Chen, B.-S. Kim, P. T. Hammond and Y. Shao-Horn. Nature Nanotechnology 5, 531 **(2010)**.

12. E. Bekyarova, E. T. Thostenson, A. Yu, H. Kim, J. Gao, J. Tang, H. T. Hahn, T.-W. Chou, M. E. Itkis, and R. C. Haddon. Langmuir 23, 3970 **(2007).**
13. J. Smithyman, Z. Liang, J.P. Zheng, B. Wang, C. Zhang. Binder-Free Nanocomposite Material And Method of Manufacture, U.S. Patent 20,110,111,279, May 12 **( 2011)**.
14. W. A. Curtin. Advances in Applied Mechanics 36, 163 **(1999)**.
15. B. McCarthy, J.N. Coleman, R. Czerw, A.B. Dalton, M. in het Panhuis and A. Maiti et al. J. Phys. Chem. B **106**, 2210 **(2002)**.
16. A.H. Barber, S.R. Cohen and H.D. Wagner. Appl. Phys. Lett., **82**, 4140 **(2003)**.
17. Y. Ganesan, C. Peng, Y. Lu, P. E. Loya, P. Moloney, E.Barrera, B. I. Yakobson, J.M. Tour, R. Ballarini, and J. Lou. *ACS Appl. Mater. Interfaces 3*, 29 (**2011)**.
18. Z. H. Xia, L. Riester, W. A. Curtin, H. Li, B. W. Sheldon, J. Liang, B. Chang and J. Xu. Acta Materialia, 52, 931 **(2004).**
19. E. Mader, K. Jacobasch, K. Grundke, and T. Gietzelt. Composites Part A 27, 907 **(1996)**.

# Appendix 2: A Method to Evaluate the Interfacial Friction between Carbon Nanotubes and Matrix

Quan Xu[1], Yuqin Yao[2] , J.Y. Liang[2] and Z.H,Xia[1,3]

## Abstract

A new method has been developed to determine the interfacial friction between carbon nanotubes (CNTs) and polymer matrix. A stripe made of PMMA with a specific contact pattern was imprinted on a CNT substrate with an ordered CNT array. By simultaneously measuring the vertical displacement and load in the decohesion process, the interfacial friction was calculated based on analytical formula from micromechanics. To extract quantitative results, a 3D finite element model for the decohesion test was developed and a cohesive zone model was used to predict the complex equilibrium crack front. The model predicts that the interfacial energy is a function of maximum separation force, sample size and CNTs height, and the model agrees well with full numerical results over a wide range of stripe and substrate property values. The overall method is applied to determine the interfacial friction of CNT/PMMA nanoimprint. The measured interfacial strength is in the range of 29-44 MPa.

## 1. Introduction

In micron fiber-reinforced matrix composites, the dominant toughening mechanism is crack deflection around fibers with weak interfaces, with “bridging” of the crack by the unbroken fibers restraining growth. Macroscopic toughness is then set by the work required to fracture and pullout the restraining fibers [1]. Fiber pullout from a matrix is usually characterized by the critical shear stress to debond the fiber/matrix interface and the subsequent shear resistance to relative sliding of the fiber and matrix. The interface sliding is often termed the “interface friction” although it may be controlled by a variety of inter-related phenomena. Recently, nanofibers have been used as reinforcement in various matrices, resulting in enhanced mechanical properties. In these nanocomposites, the interfaces form a considerable part of the total structure and exert enormous influence in the mechanical and chemical behavior of the system. A fundamental understanding of the interfacial

friction during pullout at the nanoscale is critical to the development of a new class of composites.

Because of importance of the interface in nanocomposites, efforts have been made to quantitatively measure the interfacial strength of the composites. Direct testing of simple carbon nanotube–polymer composites has been used to quantify and isolate the interfacial adhesion between individual CNTs and polymer matrices. In a nanoscale measurement, carbon nanotubes bridging across holes in an epoxy matrix have been drawn out using the tip of a scanning probe microscope while recording the forces involved. A full force-displacement trace could be recorded and correlated with transmission electron micrographs observations prior and subsequent to the tip action. Based on these experiments, an approximate calculation of the nanotube-polymer interfacial shear strength has been performed. Barber *et al*. attached individual CNTs to the end of an AFM tip and pushed the nanotube into a liquid copolymer, followed by solidification of the polymer, to produce single carbon nanotube composites [3]. The nanotube was then pulled from the polymer matrix and the critical force required for interfacial failure was recorded by the AFM. In situ transmition electron microscopy (TEM) straining technique [4,5], the CNT-polymer composite (an electron transparent thin specimen) is strained inside a TEM and simultaneously imaged to get real-time and spatially resolved (1nm) information. Similarly in Raman spectroscopy [6-10] by straining the CNT-polymer composite and catching the shifts in Raman peaks they measured the reinforcement made by CNT to polymer. More recently, Traditional single-fiber pull-out type experiments were conducted on individual multiwalled carbon nanotubes (MWNT) embedded in an epoxy matrix using a novel technique at the nanoscale [16]. The largest recorded interfacial adhesion strengths in these experiments were an order of magnitude greater than the typical engineering composite values, indicating excellent polymer adhesion to the nanotubes, although the large variability in the interfacial strength (35–376MPa). Other researchers are trying to correlate the experimental results with continuum theories like micro-mechanics of composites[11-15].

Most interfacial measurement mentioned above has been performed with nano-manipulation techniques for probing individual carbon nanotube (CNT) pullout from a polymer matrix. The major challenges is the manipulation, gripping and force and strain measurements at the nanoscale. In the present work, we have developed a new method to determine the interfacial frictional stress between CNTs and polymer.

Instead of nano-manipulation techniques, we used macro-scale samples which the CNT array was embedded in the polymer stripe with a chevron contact shape. The stripes were directly imprinted on the nanotube arrays. The peeling energy due to nanotube pullout from the matrix was determined by measuring the maximum load during peeling process. The friction and bonding strength of CNT/polymer interface was then be calculated based on the theoretical models and finite element analysis.

Another related area with similar interface problems is nanoimprinting. In nanoimprint process, there are two key issues: exact deformation of a film according to mold patterns and clear separation of the mold from the film. The separation of the mold from the thin film is analogous to the nanofiber pullout in composites. It has been showed that adhesion and friction, caused by the direct contact between mold and film, can induce significant distortion and even breakdown of transferred patterns, especially for high aspect ratio patterns. Our method can also be applied to nanoimprint separation process to measure the interfacial friction and study the effect of the interfacial friction on the pattern formation.

## 2. Test Method and Sample Preparation

### *2.1 Chevron interfacial decohesion test*

A schematic of the experimental setup is shown in Fig.1. A Poly-methyl methacrylate (PMMA) stripe with width $B$=3 mm, length $L$=10 mm and thickness $h$=0.75 mm was embedded on a vertically-aligned CNT substrate (Fig.1b). The fabrication of the samples will be described in detail later. In the decohesion test, the stripe was lifted quasistatically from hanging edge (Fig. 1a) at a constant rate of 0.005 mm/s using a micromanipulator that allows us to simultaneously measure the vertical displacement of the stripe end ($\Delta z$) and monitor the load (F). During the entire process, the contact zone near the edge of the stripe was viewed by using a Mitutoyo FS70 High-Powered Inspection Microscope microscope equipped with a video camera(U-EYE) to monitor interfacial crack propagation. The slight bending allows for a precise estimation of the interfacial adhesion strength, and further interfacial friction, directly from the force versus displacement measurements. This experiment has the advantage of simple geometry as in the classical peel experiment.

Fig. 1b shows the schematic of the top view of a test stripe on which a special interface contact is formed between the stripe and the substrate. A chevron contact shape between CNT substrate and the PMMA stripe was used to ensure crack

initiation from the chevron tip, especially for a strong interfacial bonding. Once a crack is initialed at the tip, a higher load needs to be applied to overcome the energy increase due to the increase in contact width to let the crack propagate. This allows us to accurately determine the crack length and the maximum force required for spontaneous crack propagation.

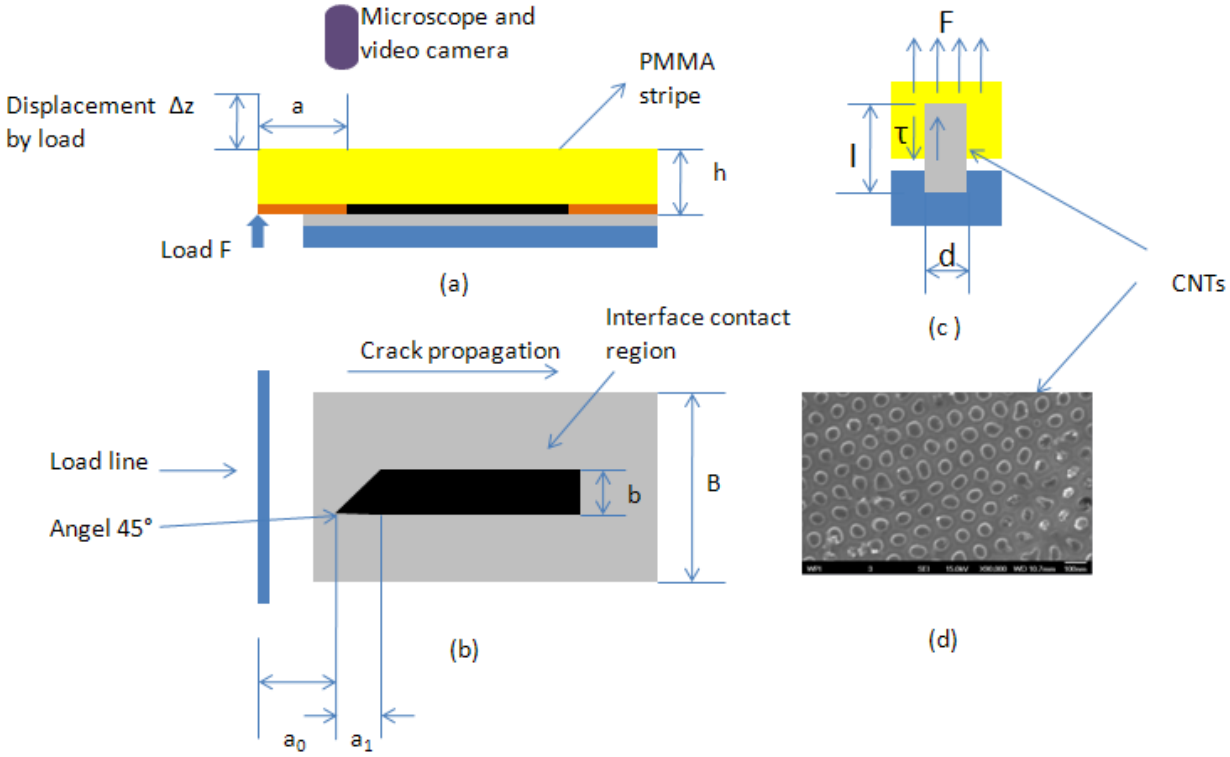


Fig. 1. (a) Schematic of interface decohesion test in which a stripe in contact with a nanotube array on a substrate is peeled off in a displacement-controlled experiment, (b) the interface between the stripe and nanotube array, showing the nanotubes partically embedded in the stripe, (c) top view of the srip and interface contact shapes between the nanotube array and the stripe, and (d) SEM image of the ordered nanotube array.

*2.2. Sample preparation*

Fabrication of the highly-ordered nanotube arrays follows the following route [17]. Briefly, high-purity aluminum is anodized in a multistep process to generate an amorphous nanoporous alumina matrix having a hexagonal array of straight pores extending from the substrate to the matrix surface. In order to fabricate highly aligned and uniform carbon nanotubes, a template assisted approach is applied to this experiment, which can provide free-standing carbon nanotubes with desired dimension, and outstanding mechanical properties, which are suitable for test in this article. A highly ordered aluminum oxide (AAO) template was fabricated via two-step

anodization. An Al sheet (99.999%) with high purity was annealed and electropolished as pretreatment. The first anodization was carried out at 40V, 0.3mol/L oxalic acid at 10℃ for 10-24h and the AAO film was removed in chromic acid for 3h, a second anodization followed up under the same condition for 12h. The template has a hexagonal structure of 50nm in diameter, and 10- 20 μ m in thickness. CNT were grown inside those nanopores using a chemical vapor deposition (CVD) method. Due to the low melting point of Al sheet, cobalt catalyst was electrochemically deposited into the bottom of nanopores, which was reduced using CO at 600℃ in tube furnace. 10% C2H4 and 90% N2 were introduced to replace CO at the same temperature for 2h. Finally CNTs were annealed overnight under a nitrogen atmosphere. The surface was polished mechanically so as to remove the amorphous carbon, finally a chemical wet-etching method was applied to expose CNTs.

After the nanotube arrays were fabricated, the CNTs were partially embedded in a PMMA stripe using imprint lithography, creating a stripe/substrate interface bridged by the nanotubes, as shown in Fig.1b. This was done by directly pressing the substrate with the nanotube arrays into the PMMA surface in a carver hydraulic machine (unit model 3912) under a pressure of 300 MPa at a temperature of 185 ℃, as schematically shown in Fig.2a. After 20 minutes, the sample was cooled down gradually under the same pressure. To form a chevron contact shape between the substrate and the stripe, a 0.005mm-thick thin film made of Polytetrafluoroethylene(PTFE, thickness 0.005mm from Goodfellow) with a pre-cut hole, as shown in Fig. 2b, was layered between the mold and substrate to separate CNTs and polymer surface. As the surface energy of PTFE is much low, CNT or PMMA does not bond with PTFE. PMMA infiltrates into the CNT array with the contact area shaped by PTFE thin film.

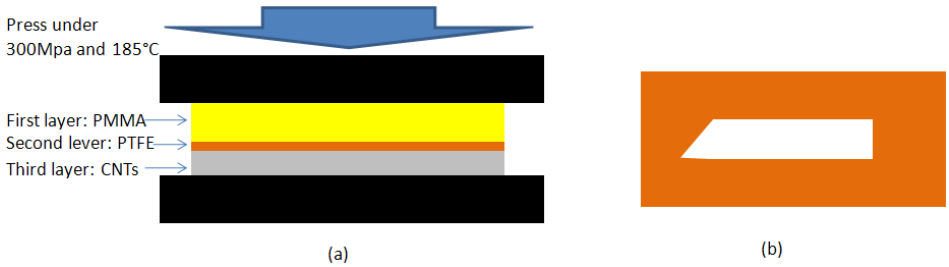


(a) (b)

Fig. 2 (a) Three layers were pressed under a hydraulic press machine with 300Mpa under a temperature of 185 ℃, and (b) top view of the second layer with a hole in the center which control the connection shape between PMMA and CNTs.

## 3. Analysis

*3.1 Interfacial friction stress*

We consider the pullout of a nanotube with diameter *d* and embedded length *l*, embedded in a stripe matrix, as schematically shown in Fig. 1. In the unit cell model, the interface between the PMMA and CNTs is assumed to have constant interfacial frictional stress $\tau$. The maximum force to pull the CNT from the matrix is:

$$F = \tau(\pi dl) \quad (1)$$

Assuming that the force changes linearly during pullout, the total work for CNT pullout is:

$$W = \frac{1}{2}Fl \quad (2)$$

Substituting equation (1) into equation (2) we have

$$W = \frac{1}{2}\pi\tau dl \quad (3)$$

This work is only related to the friction between CNT and PMMA. During the pullout process, work must also be done to overcome the interfacial energy, $\gamma_1$ and $\gamma_2$, so as to separate the PMMA/Alumina ($\gamma_1$) and PMMA/CNT($\gamma_2$) interfaces with connect area $A_1$ and $A_2$, respectively. So the total energy required is

$$W_{tot} = W + 2\gamma_1 A_1 + 2\gamma_2 A_2 = \frac{1}{2}\pi\tau dl^2 + 2\gamma_1 A_1 + 2\gamma_2 A_2 \quad (4)$$

The interfacial fracture energy can be written as

$$G_{Ic}=\frac{W_{tot}}{A} = \frac{2\tau}{d}V_f l^2 + 2\gamma_1(1 - V_f) + 2\gamma_2 V_f \quad (5)$$

Where $V_f$ is the volume fraction of CNT and $A=A_1+A_2$ is the total area of the CNT unit cell. If the CNTs are not embedded in the matrix, the interfacial fracture energy is $2\gamma_1(1 - V_f) + 2\gamma_2 V_f$. From (5) we have

$$\tau = \frac{\Delta G_{Ic} d}{2V_f l^2} \quad (6)$$

where $\Delta G_{Ic}$ is the interfacial fracture energy difference between samples with and without embedded CNTs in PMMA and can be measured separately by using decohesion test described above. Equation (6) can then be used to estimate the interfacial stress for CNT composites or nanoimprint.

*3.2 Fracture energy of the interface with embedded CNTs*

The interfacial fracture energy difference, $\Delta G_{Ic}$, required for the evaluation of the interfacial friction strength can be calculated by energy balance during crack propagation in the decohesion test. The $G_{Ic}$ is the energy required per unit area swept out by a quasistatically advancing mode I steady-state crack tip propagation under plane strain conditions. The energy $\Delta w$ required to advance the steady-state crack (crack front length $b$ ) an infinitesimal distance $\Delta a$ is

$$\frac{\partial w}{\partial a} = G_{Ic} b \tag{7}$$

The deflection $\Delta$z of a cantilever beam subjected to a concentrated load F (Fig. 1), can be written as:

$$\Delta z = \frac{F a^3}{3EI} \tag{8}$$

where F is force, E the elastic modulus of the cantilever beam and I is the moment of inertia of the cross-sectional area with respect to the neutral axis.

The irrecoverable work W, done in advancing the crack an infinitesimal distance $\Delta$a under load $F$, is given by

$$W = \frac{1}{2} F \Delta z \tag{9}$$

Substitution of Equation (8) into Equation (9) yields

$$W = \frac{F^2 a^3}{6EI} \tag{10}$$

The first derivative of $W$ with respect to $a$ is

$$\frac{\partial W}{\partial a} = \frac{F^2 a^2}{2EI} \tag{11}$$

The energy required to create a new surface b$\Delta a$ is obtained from $dW$ only, and therefore,

$$\frac{\partial W}{\partial a} = \frac{F^2 a^2}{2EI} \tag{12}$$

The moment of inertia can be calculated by standard formula of plate $I = \frac{Bh^3}{12}$. Combining Equations (8) and (12), we have

$$G_{Ic} = Y \frac{6F^2 B}{Ebh^3} a^2 \tag{13}$$

In Equation (13), $Y$ is a dimensionless function, independent of the material properties. If force reaches its maximum value at $F=F_{max}$, Equation (13) becomes

$$G_{Ic} = Y \frac{6F_{max}^2 B}{Ebh^3} a^2 \quad (14)$$

The analytical formula (14) is derived to calculate approximately the adhesive bonding strength from a test specimen with a chevron-shaped bonding interface. Here, $Y$ must be experimentally or numerically determined for different specimen geometries. Finite element modeling provides a straightforward method for determining the minimum value of the geometry function, as will be discussed in the following section.

## 4. Finite element analysis

A three-dimensional finite element (FE) model of the chevron interfacial decohesion test was developed and shown in Fig.3. The model consists of PMMA plate, aluminum substrate and alumina/CNT composite layer on the substrate; size of the model is the same as the experimental samples. The discretized FE models contain about 35484 nodes and 30340 elements with very fine meshes in the contact region between composite and PMMA. The final mesh density was determined through a series of convergence studies. Appropriate boundary conditions were used along the symmetry plane and displacements were prescribed at the edge of the specimen to simulate the load applied during testing. The substrate/PMMA interface was modeled using cohesive elements. Traction-separation law was used in the cohesive element to simulate the crack propagation. For fracture problems, where one is concerned with the propagation of a steady-state crack front, only the critical strain energy is required and hence the maximum separation stress $\sigma_{max}$ and cohesive zone length $\delta_c$ can be adjusted. Given the work of fracture $G_{Ic}$, and maximum separation stress $\sigma_{max}$, the cohesive zone length is defined as

$$\delta c = \frac{E G_{Ic}}{\sigma_{max}^2} \quad (15)$$

To properly model crack growth in a finite-element/cohesive-zone model, the numerical mesh must be several times smaller than the characteristic cohesive zone length. In our calculations, the mesh size is five times smaller than the cohesive zone length. The calculations were performed using the commercial finite element package ABAQUS. The parameter and material properties used in the calculation are listed in Table 1.

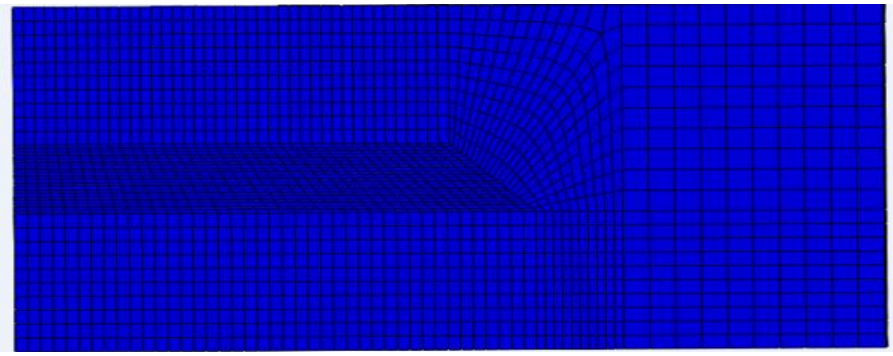

(a)

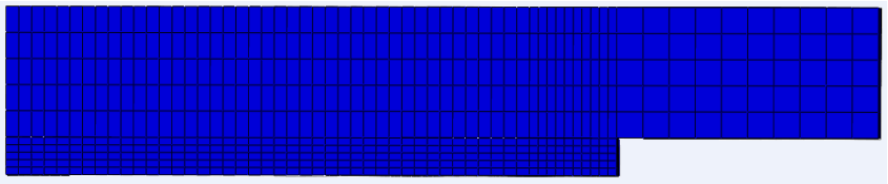

(b)

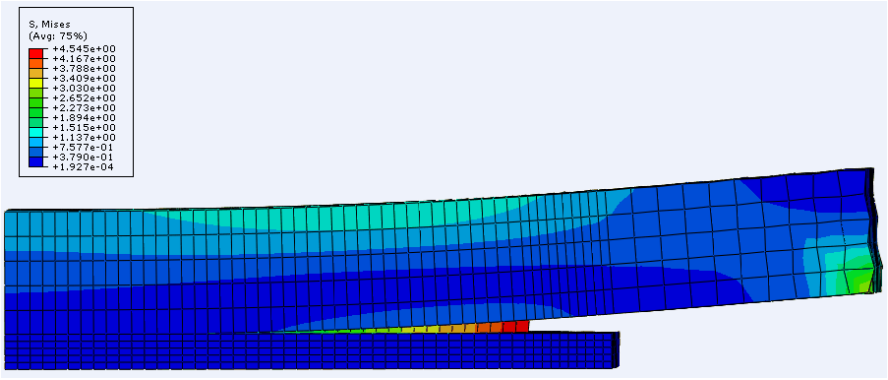
S, Mises
(Avg: 75%)
+4.545e+00
+4.167e+00
+3.788e+00
+3.409e+00
+3.030e+00
+2.652e+00
+2.273e+00
+1.894e+00
+1.515e+00
+1.137e+00
+7.577e-01
+3.790e-01
+1.927e-04

(c)

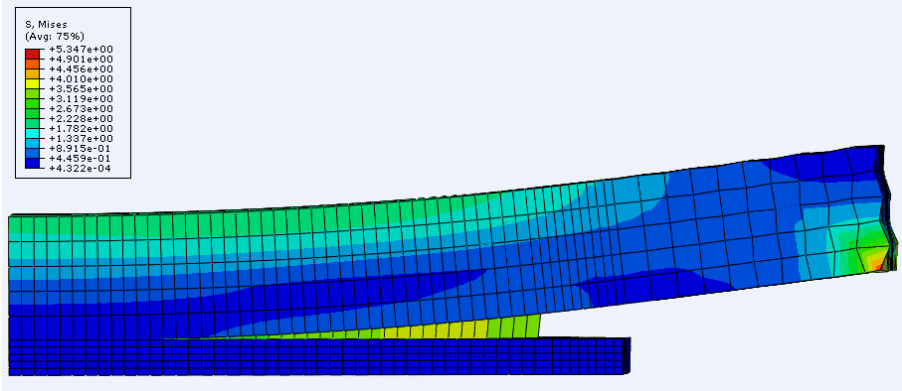
S, Mises
(Avg: 75%)
+5.347e+00
+4.901e+00
+4.456e+00
+4.010e+00
+3.565e+00
+3.119e+00
+2.673e+00
+2.228e+00
+1.782e+00
+1.337e+00
+8.915e-01
+4.459e-01
+4.322e-04

(d)

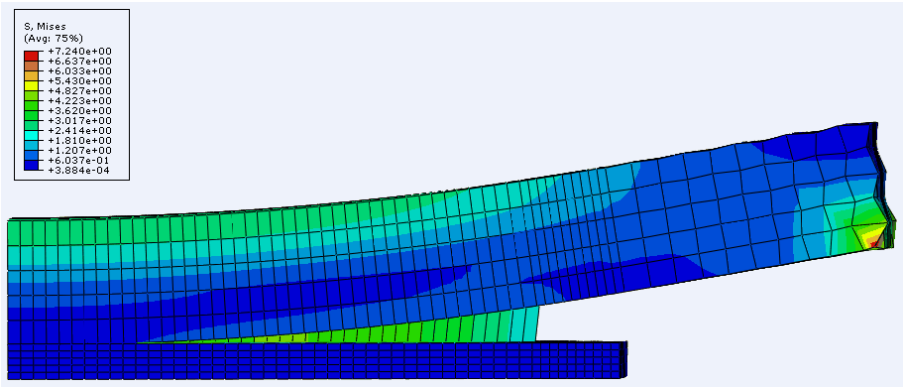


(e)

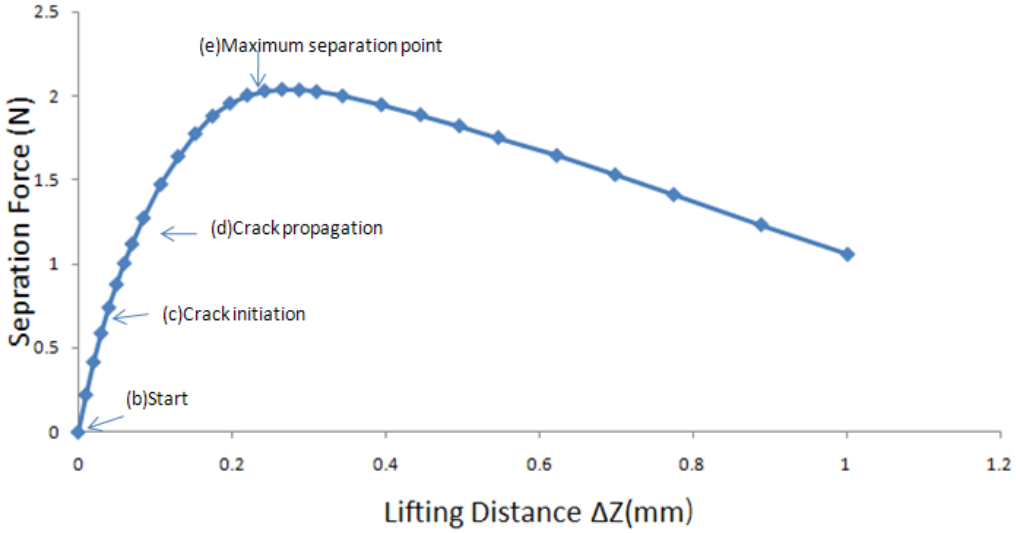


(f)

Fig-3 Snapshots of FEA simulation under peeling: (a) Top-view of FEA model, (b) front-view of FEA model, (c) crack initiation at the front of contact zone, (d) propagation of crack front, (e) critical separation point, and (f) Typical force-lifting distance curve simulated by FEA.

Table 1 Parameters used for CNT/ PMMA adhesion model

| PMMA height h(mm) | Distance $a_0$(mm) | Triangle length $a_1$ (mm) | Stripe width b(mm) | PMMA width B(mm) | PMMA Young's Modulus E(Mpa) | Traction separation stress T(Mpa) | Al Young's Modulus $E_2$(Gpa) | Separation length $\delta_f$(mm) |
|---|---|---|---|---|---|---|---|---|
| | | | | | | | | |

| | | | | | | | | |
|---|---|---|---|---|---|---|---|---|
| 0.75 | 2 | 0.5 | 1 | 3 | 3200 | 0.05-0.4 | 90 | 0.06 |

## 5. Results and discussion

*5.1 Numerical analysis*

The peeling of PMMA stripe from the composite substrate was simulated using the finite element model. For a given interfacial fracture energy, $G_{IC}$, the crack initiates at the tip of chevron contact area. The crack then gradually propagate along the surface and suddenly accelarate at the point of $a=l$, at which the force reaches its maxium value. The crack grows unstably after the point since the surface energy keep the same while the elastical energy stored in the system increses.

To verify Eq. (14), we calculated the maximum force for various configurations with the PMMA height $h$, stripe width $b$ and loading distance $l= a_0+a_1$. Figure 3 shows the maximum force as functions of $h$, $b$, and $l$. $F_{\max} \propto h^{1.5}$ approximately within the range from $h$=0.7mm to $h$=0.85mm, for a given b and $l$ (Figure 4a). For fixed $h$, and $l$, the maximum force $F_{max}$ nearly linearly increases with increasing stripe width $\sqrt{b}$ (Figure 4b). We also study the effect of the stripe width $B$ on the maximum force, and found that $F_{max}$ is independent of $B$. These results are consistant with the analytical solution (Eq. (14)). However, we found that $F_{\max} \propto l^{-0.54}$ ,which is inconsistent with Equation 14. (Figure 4c). This discrepency is due to the crack propagation which changes the value of $l$ during peeling. Finally, we found that the geometric factor $Y$ is a function of interfacial energy $G_{IC}$. This may also be attributed to the fact that $l$ is not a constent. Therefore, Equation (14) must be modified so as to evaluate the interfacial facture energy in the Chevron interfacial decohesion test. A modified formula was derived based on the analytical and FEA results,

$$G_{Ic} = Y[\frac{6F_{max}^2 B}{Ebh^3} l^2]^n \tag{16}$$

$$Y = Y_0 l^{m_1} b^{m_2} h^{m_3} \tag{17}$$

where the geometric factor $Y_0$=0.75, $m_1$=-0.51166, $m_2$=0.2646, $m_3$=1.497, and $n$=0.55766.

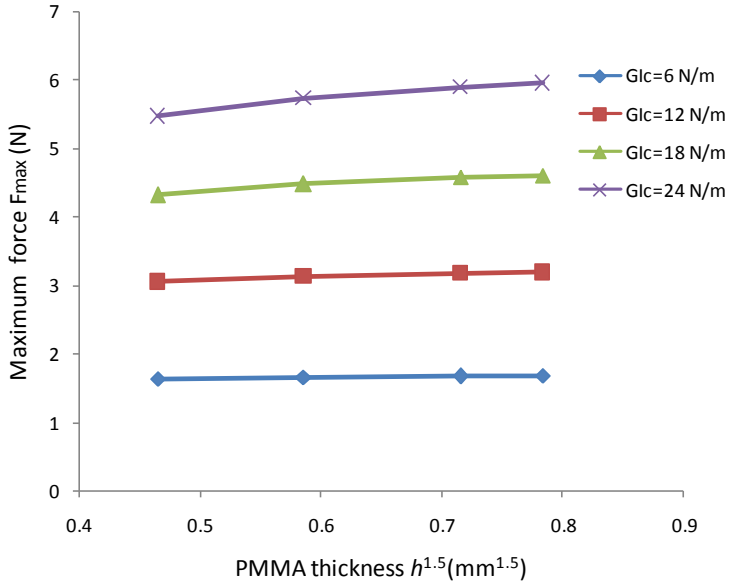
Maximum force Fmax (N)
PMMA thickness $h^{1.5}$(mm$^{1.5}$)
Glc=6 N/m
Glc=12 N/m
Glc=18 N/m
Glc=24 N/m

(a)

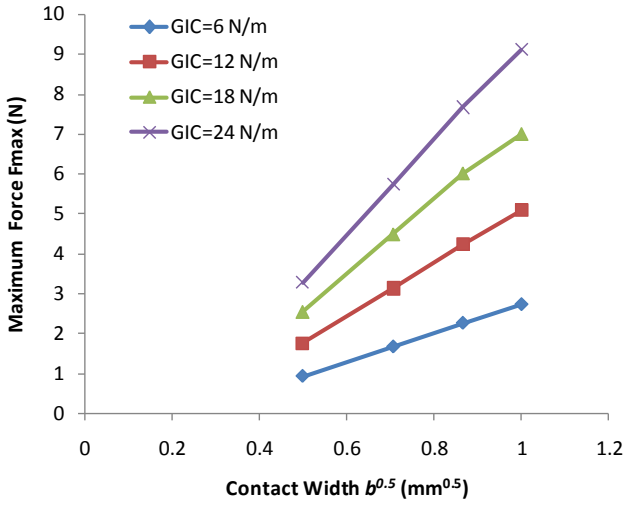
Maximum Force Fmax (N)
Contact Width $b^{0.5}$ (mm$^{0.5}$)
GIC=6 N/m
GIC=12 N/m
GIC=18 N/m
GIC=24 N/m

(b)

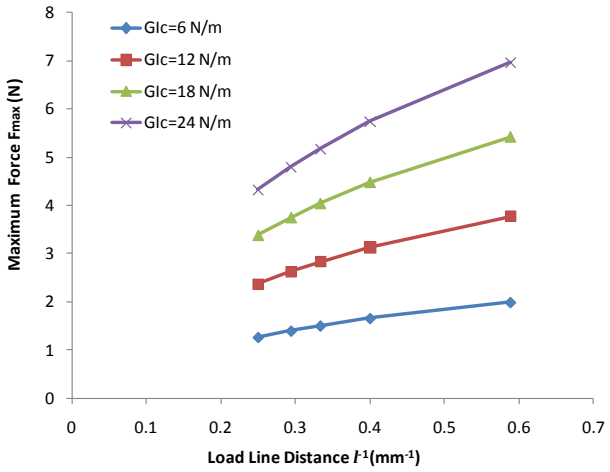


(c)

Fig 4. Maximum separation force as a function of (a) PMMA height for $b$=1mm and $a$=2mm, (c) contact width for $a$=2mm and $h$=0.75mm, and (b) load line distance for $b$=1mm and $h$=0.75mm, for different interfacial energy $G_{IC}$.

*5.2 Experimental results and discussion*

Figure 5 is the process of crack growth during the peeling. As shown in Fig. 5a, the PMMA strip is adhesive firmly to the substrate surface (CNT array) before peeling. With increasing the load, a crack initiates at the chevron notch (Fig. 5b), followed by a relative stable crack growth along the bonded interface within the triangle area. The triangle-shaped bonded area provides an increasing interfacial area with increasing crack length and load, and initially results in stable crack propagation. At some crack length, the propagation becomes unstable and catastrophic failure of the sample occurs. This coincides with the point of maximum load.

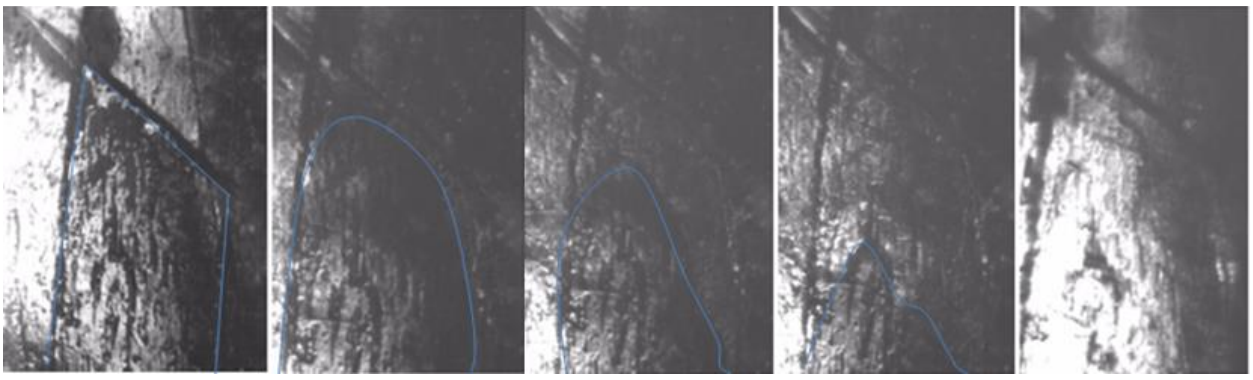

(a) (b) (c)

(d) (e)

Fig. 5.The crack growth in different stages: (a) Original contact state, (b) crack initiate at the tip of the chervon, (c) statabe crack propogation, (d) unstable and sudden failure, and (e) complete seperation of the interface.

In the experiment, specimens with/without CNT protrusion were tested and typical load-displacement curves for a bonded chevron specimen are shown in Fig.6. For both specimens, the force increases nearly linearly with increasing displacement during the initial loading but the slope of the force-displacement for the specimen with CNT protrusion is much larger than that for the flat surface. After the initial increase, the force for both cases reaches a peak and then drops to zero but the peak value for the CNT protrusion is much large compared to the sample with flat surface. The interface was completely separated after the peak. For each test, a maximum force $F_{max}$ was obtained and this value can be used to calculate the interfacial fracture energy $G_{IC}$ using Eq.16.

After the PMMA stripes were peeled off from the composite surface, the surfaces were examined with Scanning Electron Microscopy (SEM). Figure xx shows ...

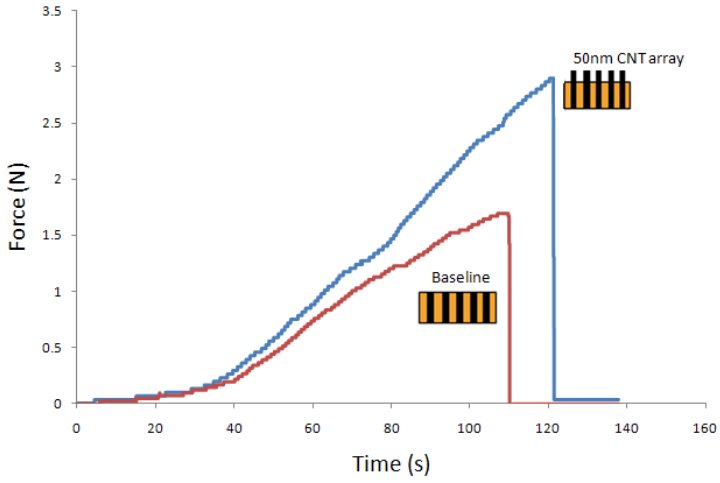


Fig.6 a typical load-displacement curves for a bonded chevron specimen with and without CNT protusion.

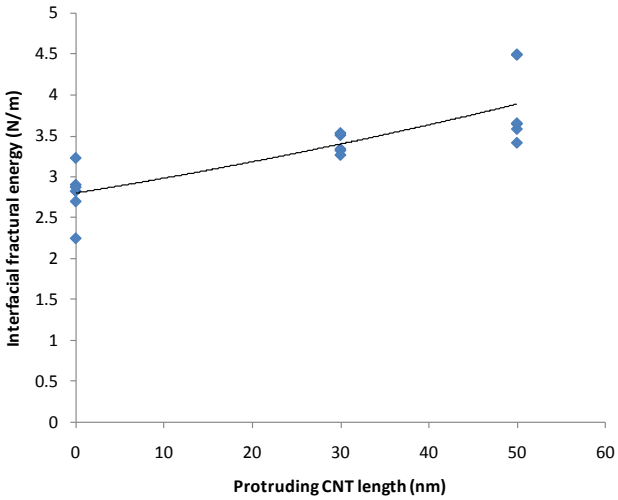


Fig.7 Interfacial fracture energy as a function of protruding CNT length

Fig. 7 shows measured interfacial fracture energy $G_{IC}$ as a function of protruding length of CNT arrays. The CNT protruding length strongly affects the surface energy of CNT/PMMA interface. The interfacial energy nonlinearly increases with increasing the protruding length of CNT array. Since the amount of the energy increase is induced by the CNT protrusion, it can be used to calculate the interfacial frictional stress $\tau$ at the CNT/PMMA interface using Eq. 6. Taking CNT diameter $d$=40 nm, CNT volume fraction $V_f$=0.3, the interface friction stress $\tau$ was estimated to be 29 and 44 MPa . This value is in the range of measured values for CNT/epoxy composites, obtained by other techniques [2-10].

## 6. Conclusions

Chevron interfacial decohesion test method has been developed to evaluate interfacial energy and the interfacial friction between carbon nanotubes (CNTs) and polymer matrix. A stripe made of PMMA was imprinted with a specific contact pattern on a CNT substrate with a highly-ordered nanofiber array. By simultaneously measure the vertical displacement and monitor applied load in the decohesion process, the fracture energy and interfacial friction were calculated based on analytical formula from micromechanics. To extract quantitative results, a 3D finite element model for the decohesion test was developed and a cohesive zone model was used to predict the complex equilibrium crack front. The model predicts the interfacial energy is a function of maximum separation force, sample size and CNTs height, and the model agrees well with full numerical results over a wide range of stripe and substrate property values.

The interfacial friction of CNT/PMMA composites obtained from this method is consistent with the results from other methods.

## Acknowledgement

The authors would like to thank the support by NSF under the contract #.CMMI-0825990.

## References

[1] Piggott M. Load bearing fiber composites. 2nd ed. Dordrecht: Kluwer Academic Publisher;2002.

[2] C.A. Cooper, S.R. Cohen, A.H. Barber and H.D. Wagner, Detachment of nanotubes from a polymer matrix, *Appl Phys Lett* **81** (2002), pp. 3873–3875.

[3] A.H. Barber, S.R. Cohen and H.D. Wagner, Measurement of carbon nanotube-polymer interfacial strength, *Appl Phys Lett* **82** (2003), pp. 4140–4142.

[4] D. Qian, G.J. Wagner, W.K. Liu, M.-F. Yu and R.S. Ruoff, Mechanics of carbon nanotubes, Appl Mech Rev **55** (2002), pp. 495–532

[5] D. Qian, W.K. Liu and R.S. Ruoff, Load transfer mechanism in carbon nanotube ropes, Compos Sci Technol **63** (2003), pp. 1561–1569

[6] P.M. Ajayan, L.S. Schadler, C. Giannaris and A. Rubio, Single-walled carbon nanotube-polymer composites: strength and weakness, Adv Mater 12 (2000), pp. 750–753. [53] C.A. Cooper, R.J. Young and M. Halsall, Investigation into the deformation of carbon nanotubes and their composites through the use of Raman spectroscopy, Compos Part A Appl Sci Manuf 32 (2001), pp. 401–411.

[7] V.G. Hadjiev, M.N. Iliev, S. Arepalli, P. Nikolaev and B.S. Files, Raman scattering test of single-wall carbon nanotube composites, Appl Phys Lett 78 (2001), p. 3193.

[8] A. Paipetis, C. Galiotis, Y.C. Liu and J.A. Nairn, Stress transfer from the matrix to the fibre in a fragmentation test: Raman experiments and analytical modeling, J Compos Mater 33 (1999), pp. 377–399.

[9] L. Valentini, J. Biagiotti, J.M. Kenny and M.A. Lopez Manchado, Physical and mechanical behavior of single-walled carbon nanotube/polypropylene/ethylene-propylene-diene rubber nanocomposites, J Appl Polym Sci 89 (2003), pp. 2657–2663.

[10] D. Qian and E.C. Dickey, In-situ transmission electron microscopy studies of polymer-carbon nanotube composite deformation, *J Microsc* **204** (2001),

[11] Gou J, Minaie B, Wang B, Liang Z, Zhang C. Computational and experimental study of interfacial bonding of single-walled nanotube reinforced composites. Comput Mater Sci 2004;31:225-36

[12] Thostenson ET, Chou T-W. Aligned multi-walled carbon nanotube-reinforced composites: processing and mechanical characterization. J Phys D Appl Phys 2002;35:77-80

[13] Bower C, Rosen R, Jin L, Han J, Zhou O. Deformation of carbon nanotubes in nanotube-polymer composites. Appl Phys Lett 1999;74:3317-9

[14] Schadler LS, Giannaris SC, Ajayan PM. Load transfer in carbon nanotube epoxy composites. Appl Phys Lett 1998;73:3842.

[15]Wagner HD. Nanotube-polymer adhesion: a mechanics approach. Chem Phys Let 2002;361:57-61

[16] Li J, Papadopoulos C, Xu JM, Moskovits M. Appl Phys Lett,1999;75:367–9.

[17] Yogeeswaran Ganesan, Cheng Peng, Yang Lu, Phillip E. Loya, Padraig Moloney, Enrique Barrera, Boris I. Yakobson, James M. Tour, Roberto Ballarini, and Jun Lou, Interface Toughness of Carbon Nanotube Reinforced Epoxy Composites, *ACS Appl. Mater. Interfaces*, **2011**, *3* (2), pp 129–134.

# Appendix 3: Supporting information for Paper 3#

**Determination of number of layers of GNS**

To calculate the number of layers of GNS coating on individual $TiO_2$ NPs, several assumptions were made: (1) $TiO_2$ NPs have the same diameter; two boundary conditions were considered to determine the graphene thickness range: 40nm, when $TiO_2$ NPs were all 40 nm in size, the thinnest graphene coating would be determined, and 200nm, when $TiO_2$ were all 200nm in size, the thickness graphene coating would be determined; (2) The shape of $TiO_2$ NPs is sphere; (3) continuous, conformal and uniform GNS coating were formed the same on each $TiO_2$ NPs; (4) 100% of GNS were coated on $TiO_2$ NPs.

For a single $TiO_2$ sphere, the surface area is $A=4\pi r^2=5024nm^2$

Volume is $V=4\pi r^3/3=33493nm^3$

Weight of $TiO_2$ sphere $W=V*\rho=33493nm^3*3.84g/cm^3=1.3*10^{-13}mg$

For a weight of $TiO_2$/GNS composite at 100mg, weight of $TiO_2$ is 93.62mg.

So the number of $TiO_2$ NPs is $N=\frac{W_{total}}{W_{TiO_2}}=7.2*10^{14}$

The total area of $TiO_2$ $A_{total}=A*N=3.6*10^{18}nm^2=3.6m^2$

For the 2nd layer of GNS, the area can be calculated at an r of 21nm, the area is $4.0m^2$. Same for 3rd layer of GNS, the area is $4.4m^2$.

For a single layer of graphene, one single atom is connected to the adherent 3 carbon atoms, the bonding length of C-C is 0.142nm. A single hexagonal ring of carbon atoms can be considered a basic unit of GNS. Only 1/3 of a single atom belongs to a hexagonal ring, so each hexagonal ring contains 2 carbon atoms. The area of hexagon is $0.052nm^2$, so the area density of graphene can be calculated as $0.77mg/m^2$.

The weight of the first layer of graphene coated on $TiO_2$ NPs is:

$$W_{single\ graphene}=A_{total}*0.77mg/m^2=2.772mg$$

Weight of 2nd and 3rd layer of graphene can be calculated to be 2.695mg and 2.541mg, respectively.

Because $W_{1st\ graphene}+W_{2nd\ graphene}+W_{3rd\ graphene}>W_{graphene}>W_{1st\ graphene}+W_{2nd\ graphene}$, therefore this result indicates that the number of the graphene coated is about 2~3 layers.

Take an experimental AFM thickness of single layered graphene (~1nm) as the

thickness of each layer of GNS, so the total thickness is:

$$T=0.34+2*1 =2.34nm$$

Take the diameter of $TiO_2$ NPs as 200nm, by using the same procedure, weight of each layer of graphene can be calculated as following:

$$W_1=0.56mg;$$

$$W_2=0.57mg;$$

$$W_3=0.58mg;$$

$$W_4=0.6mg;$$

$$W_5=0.61mg;$$

$$W_6=0.62mg;$$

$$W_7=0.63mg;$$

$$W_8=0.64mg;$$

$$W_9=0.65mg;$$

$$W_{10}=0.67mg;$$

Since $W_{graphene} \approx \sum_{i=1}^{10} W_i$, number of layers can be calculated to be 10, the thickness is 9.34nm.

From the calculations above, we can conclude that the number of layers of GNS ranges from 2 to 10, the thickness of the GNS coated on individual $TiO_2$ ranges from 2.34nm to 9.34nm.Since the size distribution of $TiO_2$ mainly stays below 100nm so the thickness of the GNS will be the lower part of the thickness range. This calculation agrees well with the AFM result.

**Phase control of $TiO_2$**

Rutile and anatase are the two of most common phases for $TiO_2$. The only difference between these two phases is the arrangement of the molecules: for anatase $TiO_2$, a body centered tetragonal crystal contains $TiO_6$ octahedras that have edge sharing with others; for rutile $TiO_2$, each $TiO_6$ octahedra shares edges with each other, and forms a single chain. Anatase $TiO_2$ phase is highly desired because it is the most electroactive phase for Lithium storage. Sol-gel method can provide anatase $TiO_2$ NPs with high specific area, low aggregation and excellent controllability over the particle size. During a specific sol-gel method, the calcination step dominates the phase composition of the $TiO_2$ nano particles.

For a typical nucleation process, the energy barrier can be written as[1]:

$$\Delta G_c = \frac{4 f^3 \gamma^3}{27(G_2 - G_1)^2} \tag{1}$$

f—geometry factor,

γ—surface tension，

$G_2$ and $G_1$—single atom energy for amorphous $TiO_2$ and anatase $TiO_2$, respectively. And the number of the nucleus can be described below:

$$N^* = N \exp\left(\frac{-\Delta G_c}{kT}\right) \tag{2}$$

N—the total number of atoms,

k—the Boltzmann's constant，

T—the solidification temperature.

Assume that the particle are the spheres, the anatase $TiO_2$ volume fraction can be written as:

$$I(T,t) = \frac{4}{3}\pi n(T) v^3(T) t^4 \tag{3}$$

t—the time,

n(T) —the nucleation rate，

V—velocity of the interface between amorphous $TiO_2$ and anatase $TiO_2$.

Usually from amorphous $TiO_2$ to anatase $TiO_2$, a certain temperature is needed. According to Figure 1(b), in the temperature-time-transition diagram the bold line stands for the barrier between amorphous $TiO_2$ and anatase $TiO_2$, the annealing temperature can be calculated to be 600℃, which agrees well with the $TiO_2$ phase diagram (Figure 1(a)), anatase stays stable from low temperature to ~600℃.

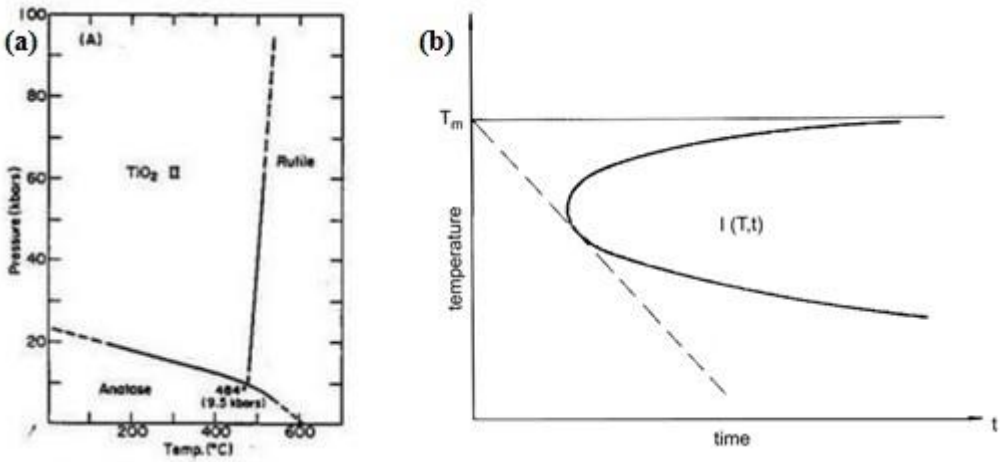

Figure 1: (a) Phase diagram of TiO2; (b) Temperature, time, transition diagram[1]

According to experimental results[2], they also suggest that the temperature is the key factor to the phase composition: after aging step, the $TiO_2$ phase is amorphous; the anatase starts to form at 300℃, and the crystalline structure gets improved with the increase of the temperature; the rutile phase of $TiO_2$ does not occur until 850℃.

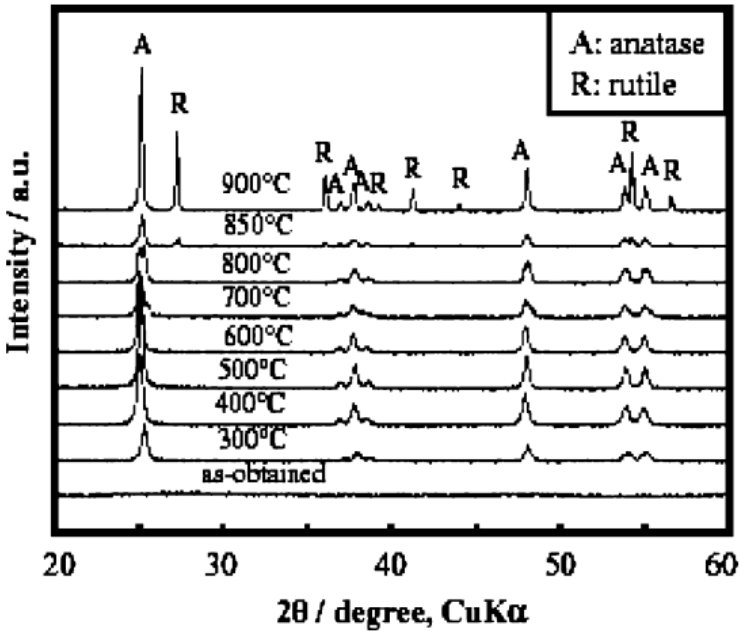


Figure 2: XRD patterns of the as-prepared powder and those after annealing at different temperatures. (A: anatase, R: rutile)[2].

The calcination temperature might also vary due to different precursor applied in the sol-gel synthesis process. According to Table 1[3], the conclusion suggests that 500℃ would be an optimized calcination temperature for various reaction conditions. Therefore, in our synthesizing $TiO_2$ NPs process, we adapted 500℃ as the calcination temperature so as to obtain stable anatase $TiO_2$ phase.

Table 1: Physicochemical Properties of $TiO_2$ Particles Prepared under Various Synthesis Conditions[3]

| synthesis condition | temp (°C) | crystal phase | $V_{pore}$ ($cm^3/g$) |
|---|---|---|---|
| no addition ($S_{control}$) | as-synthesized | amorphous | 0.68 |
| | 500 | anatase | 0.30 |
| [bmim][$PF_6$] ($S_{PF6}$) | as-synthesized | anatase | 0.30 |
| | 500 | anatase | 0.27 |
| [bmim][$BF_4$] ($S_{BF4}$) | as-synthesized | amorphous | 0.05 |
| | 500 | anatase | 0.21 |
| [bmim][$PF_6$] and T80 ($S_{PF6,T80}$) | as-synthesized | anatase | 0.06 |
| | 500 | anatase | 0.31 ± 0.06 |
| T80[a] | as-synthesized | amorphous | 0.01 |
| | 500 | anatase | 0.04 |

**Size control**

Among various methods to synthesize $TiO_2$ NPs, sol-gel is considered to be an efficient method for the size control[4]. For a typical sol-gel method with $TiCl_4$ as precursor, the grain growth kinetics was conducted:

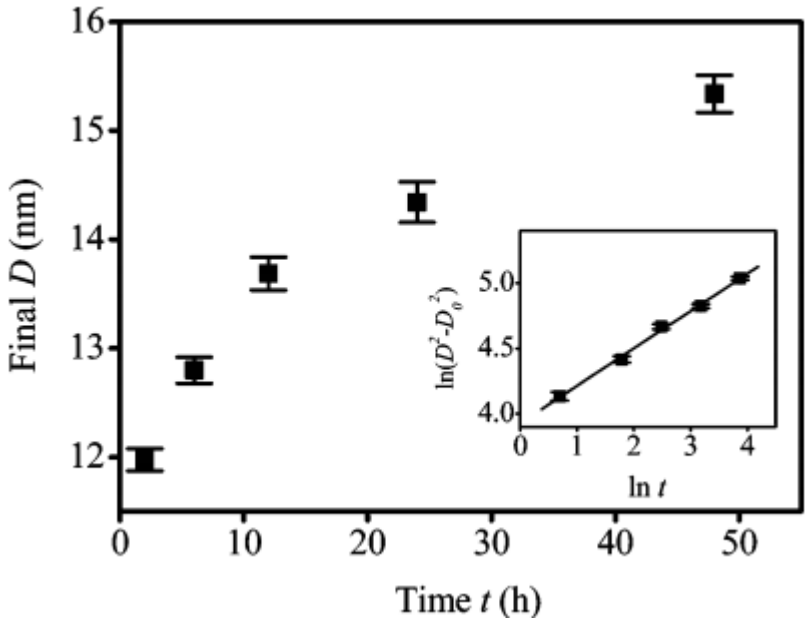


Figure 3: Isothermal grain growth for anatase nanocrystals that were obtained at 300 ℃ for different reaction times. Inset shows the grain growth plotted as $\ln(D^2 D_0^2)$ versus t. $D_0$ denotes the initial particle size[5].

Figure 3 plots the isothermal grain growth of the anatase $TiO_2$ NPs (diameter versus time), which can be described as below[5]:

$$\ln(D^2-D_0^2)= 3.93(2)+0.286(9)\ln t \quad (4)$$

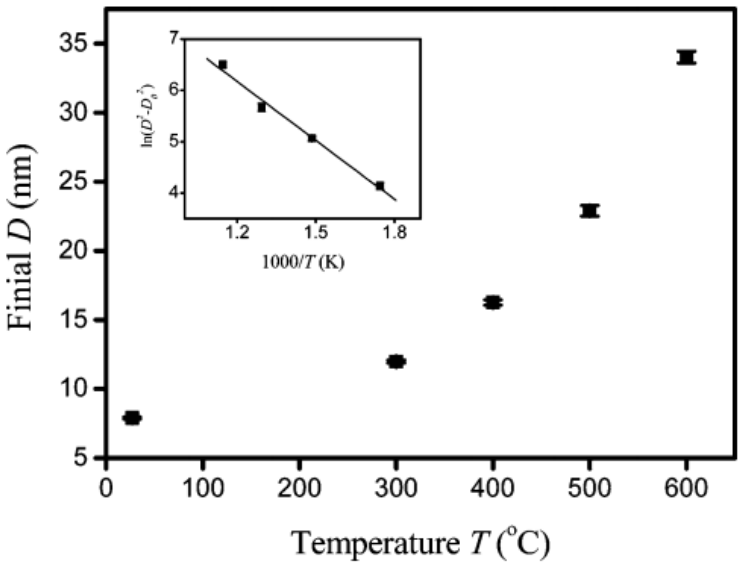


Figure 4: Temperature dependence of the particle size for anatase nanocrystals that were obtained after heating at different temperatures for 2 h. Inset shows the grain growth plotted as $\ln(D^2-D_0^2)$ versus $1/T$[5].

Figure 5 is the temperature dependent diagram of anatase $TiO_2$ NPs, which were calcinated at a fixed duration of 2 hours. The result indicates that the particle size not only increases with the duration, but also increases with the calcination temperature, which can be written as[5]:

$$\ln\left(D^2 - {D_0}^2\right) = 10.8(4) - \frac{3.8(3)\times 10^3}{T} \quad (5)$$

Since growth kinetics of $TiO_2$ NPs have been well developed, an equation of $D^n = k_0 t^m e^{\left(-\frac{E_a}{RT}\right)}$ was generated, where n is the growth exponent. For anatase $TiO_2$, n=5 while for rutile $TiO_2$, n=2. For most sol-gel methods, a high temperature sintering step is required, so here the growth exponent is 2, and the growth kinetic equation will be[5]:

$$D^n = {D_0}^n + k_0 t^m e^{\left(-\left(\frac{E_a}{RT}\right)\right)} \quad (6)$$

D—the diameter,

t—time,

T—the temperature,

m—the time exponent，

$E_a$—the energy required for the grain growth.

For a isothermal grain growth, the equation will be[5]:

$$\ln\left(D^2 - {D_0}^2\right) = mlnt + C_1 (C_1 = lnk_0 - \frac{E_a}{RT}) \quad (7)$$

For a temperature depending process, take the duration as 2 hours, the equation will be[5]:

$$\ln\left(D^2 - {D_0}^2\right) = C_2 - -\frac{E_a}{RT} (C_2 = ln(k_0 t^m) \quad (8)$$

By using the m as $0.286\pm0.009$, growth energy as $32\pm2$kJ·mol$^{-1}$, eq.(8) can be rewritten as[5]:

$$D^2 = {D_0}^2 + 3.86 \times 10^4 \times t^{0.286(9)} e^{\left(-\frac{32(2)}{RT}\right)} \quad (9)$$

One thing is worth noting that due to the different methodologies, the $E_a$ for the growth models will vary, which ranges from $32\pm2$kJ·mol$^{-1}$~$39\pm6$kJ·mol$^{-1}$. For a specific sol-gel process, the particle size increased with the temperature, which went beyond 30nm.

Furthermore, experimental results suggest that some other factors, such as surfactants, precursors and PH value also contribute to the determination of the particle size, as shown in Figure 5, at different PH values, the size distribution exhibited huge difference. Referring to Figure 5(C), after the calcination process, the particle size is less than 200nm, which agrees well with our experimental data.

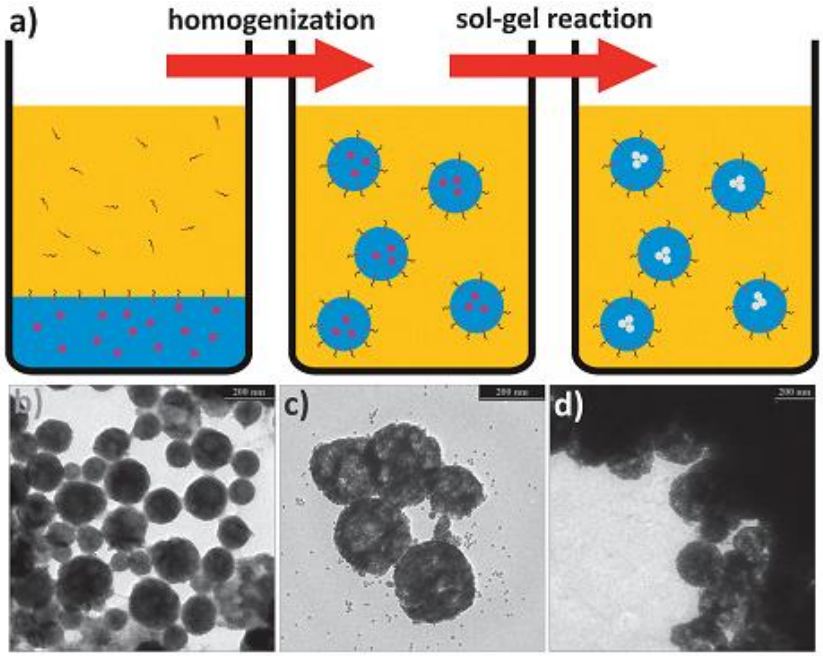


Figure 5 (a) A typical inverse miniemulsion process is schematically shown. A two phase mixture from an aqueous solution of a sol–gel precursor (purple) and an organic surfactant solution is homogenized to form a stable miniemulsion of droplets with uniform size and composition. By increasing the temperature, the sol–gel reaction is induced to generate aggregates of oxide nanoparticles (light grey). (b–d) Nanoscaled aggregates of titania crystallites, synthesized at different ratios HCl :EGMT. (b) EGMT:HCl = 1 : 5.4, as synthesized, (c) EGMT:HCl = 1 : 3.2, after calcination at 400℃, and (d) EGMT:HCl = 1 : 4.3 after calcination at 400℃[6].

**Improved conductivity enabled by GNS(paper review of 'Flexible and planar graphene conductive additives for lithium-ion batteries')**

As a novel two dimensional material, GNS has exhibited superior conductivity beyond conventional graphite materials, therefore it is of huge interest to introduce GNS into the electrode to improve the conductivity. For almost all the electrode materials (both anodes and cathodes), an effective conducting network is desired. To address this issue, there are two considerations need to be put into account: 1. High conductivity, which means the conductive materials with little defect and high crystalline integrity are preferred; 2. Effective contact between the conducting materials and electrode materials, not only suppresses the aggregation of the electrode materials, but also alleviates the agglomeration of the conductive materials. According to the Figure 3, two different conducting modes were demonstrated: for GNS based electrodes, they have the 'plane to point' mode while super-P based electrodes have

the ‘point to point’ mode[7].

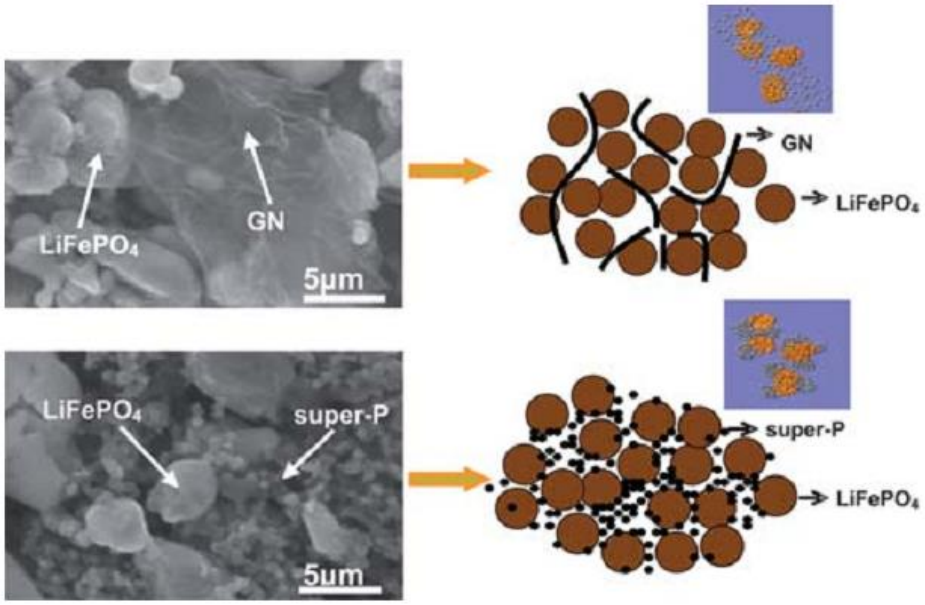


Figure 6: Schematic representations of conducting mechanisms of GN and SP as conductive additives in $LiFePO_4$ (top: plane-to-point mode for GN case, below: point-to-point mode for SP case)[7].

Compared with super-P particles, the ultrathin and flexible feature of GNS facilitated the homogeneous dispersion within the particles, which not only can serve as a ‘bridge’ to build up a conducting network within the composite, but also can provide firm contact with the active materials even under fast charging and discharging process.

From the discussion above, the ‘contact efficiency’ plays a critical role in an electrode. Since the 2-D profile of GNS enables an extremely high contact efficiency, GNS-based electrode system can provide a much higher content of active materials.

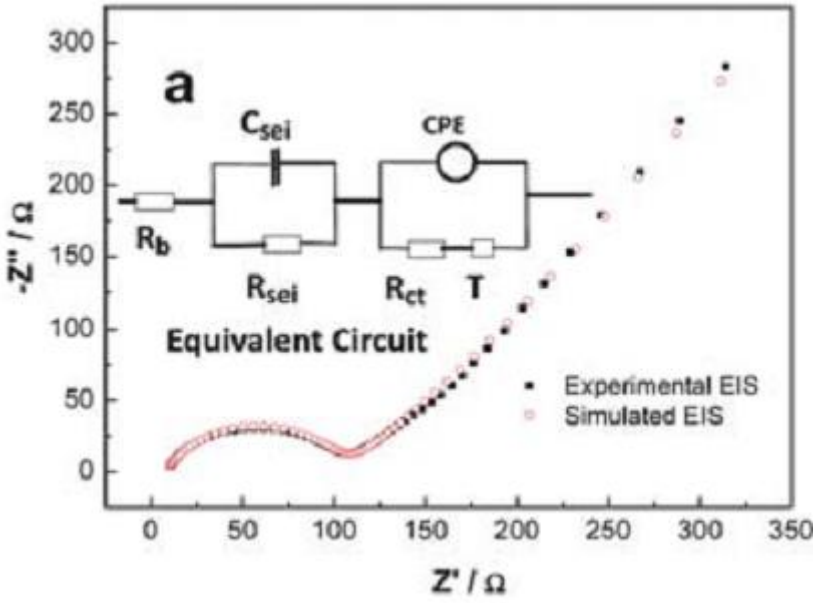
a
$C_{sei}$
CPE
$R_b$
$R_{sei}$
$R_{ct}$
T
Equivalent Circuit
Experimental EIS
Simulated EIS
-Z'' / Ω
Z' / Ω
0
50
100
150
200
250
300
350

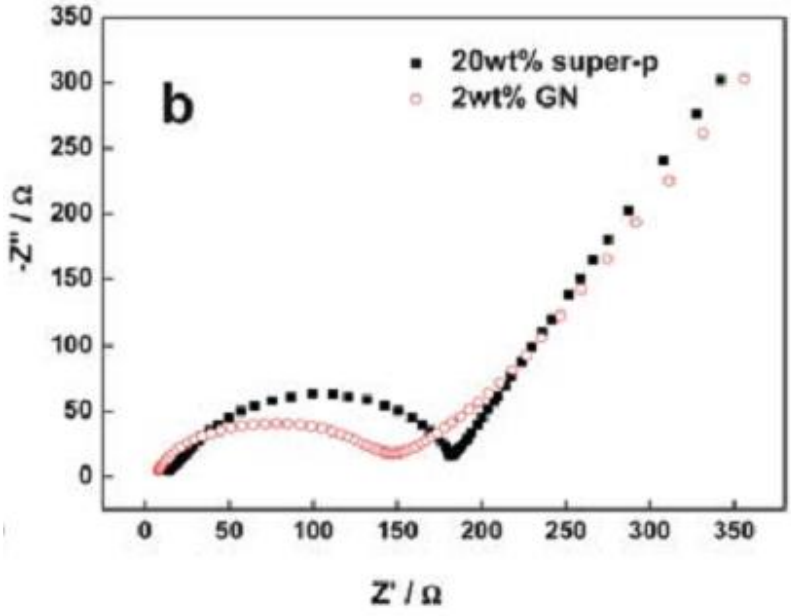
b
20wt% super-p
2wt% GN
-Z'' / Ω
Z' / Ω
0
50
100
150
200
250
300
350

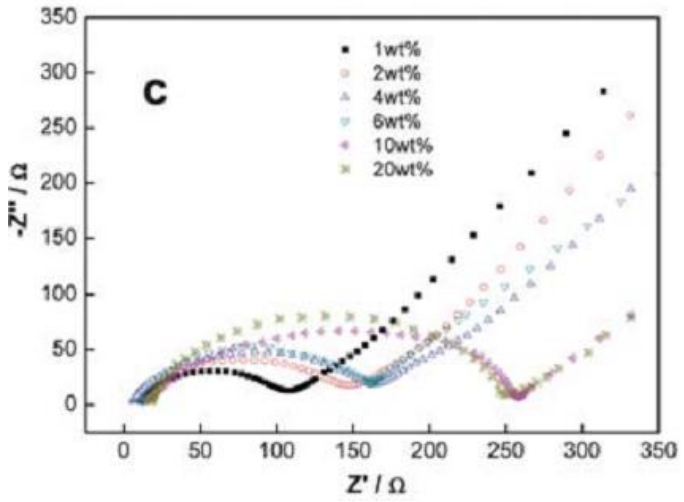


Figure 7: EIS spectra of GN-introduced LiFePO4 and SP-introduced LiFePO4 as a reference. a) Experimental and simulated EIS spectra with the equivalent circuit as an inset, b) experimental EIS spectra of Fe/GN and Fe/SP, c) experimental EIS spectra of Fe/GN with different GN fraction[7].

EIS measurements were conducted to investigate the coin cells. Figure 2(a) indicates that the EIS of $LiFePO_4$/GNS and $LiFePO_4$/Super-P agrees well with the equivalent circuit. The simulation results of the EIS data of Figure 2(b) shows that the charge-transfer resistance of $LiFePO_4$/GNS(~126Ω) is smaller than that of $LiFePO_4$/Super-P, which means the 'plane to point' mode has a much higher conducting efficiency than 'point to point' mode, enabled by the outstanding interface contact efficiency with the active materials. For super-P, the electrode system usually requires much more in weight percentage so as to facilitate the efficient electron transporting. However, the increased conductive materials will lead to severe secondary reactions between them and electrolytes, which will lead to a large charge-transfer resistance.

Further studies were conducted to investigate the influence of the GNS percentage on the electrochemical performance[7]. As observed in experimental results, increased GNS amount will lead to huge aggregation, which will block diffusion of the $Li^+$ ions. Furthermore, same as the Super-P particles, increased amount of GNS will also lead to significant side reaction between GNS and electrolyte, so the charge-transfer resistance will also increase if the GNS amount increases.

In conclusion, compared with the traditional conductive materials, the outstanding conductivity, flexible planar structural feature enabled a novel 'plane to point' contact mode between addictive and active materials. This mode can provide high contact efficiency which is superior to the 'point to point' mode. This reported

study suggests that as conductive materials for LIB applications, GNS is a promising alternative material since its bulk production has been developed for years.

**References**


1. Van Overschelde, O.; Snyders, R.; Wautelet, M. *Applied Surface Science* **2007,** 254, (4), 971-974.
2. Gao, Y.; Masuda, Y.; Seo, W.-S.; Ohta, H.; Koumoto, K. *Ceramics International* **2004,** 30, (7), 1365-1368.
3. Choi, H.; Kim, Y. J.; Varma, R. S.; Dionysiou, D. D. *Chemistry of Materials* **2006,** 18, (22), 5377-5384.
4. Fröschl, T.; Hoermann, U.; Kubiak, P.; Kučerová, G.; Pfanzelt, M.; Weiss, C.; Behm, R.; Hüsing, N.; Kaiser, U.; Landfester, K. *Chemical Society Reviews* **2012,** 41, (15), 5313-5360.
5. Li, G.; Li, L.; Boerio-Goates, J.; Woodfield, B. F. *Journal of the American Chemical Society* **2005,** 127, (24), 8659-8666.
6. Rossmanith, R.; Weiss, C. K.; Geserick, J.; Hüsing, N.; Hörmann, U.; Kaiser, U.; Landfester, K. *Chemistry of Materials* **2008,** 20, (18), 5768-5780.
7. Su, F.-Y.; You, C.; He, Y.-B.; Lv, W.; Cui, W.; Jin, F.; Li, B.; Yang, Q.-H.; Kang, F. *Journal of Materials Chemistry* **2010,** 20, (43), 9644-9650.